REVIEWS OF GEOPHYSICS AND SPACE PHYSICS, VOL. 18, NO. 1, PAGES 143–181, FEBRUARY 1980

The Role of Volatiles and Lithology in the Impact Cratering Process

SUSAN WERNER KIEFFER

U.S. Geological Survey, Flagstaff, Arizona 86001

CHARLES H. SIMONDS

Lunar Curatorial Laboratory, Northrop Services, Incorporated, Houston, Texas 77034

A survey of published descriptions of 32 of the largest, least eroded terrestrial impact structures reveals that the amount of melt at craters in crystalline rocks is approximately 2 orders of magnitude greater than at craters in sedimentary rocks. In this paper we present a model for the impact process and examine whether this difference in melt abundance is due to differences in the amount of melt generated in various target materials or due to differences in the fate of the melt during late stages of the impact. The model consists of a theoretical part for the early stages of impact, based on a Birch-Murnaghan equation of state, a penetration scheme after Shoemaker (1963), and an attenuation model modified from Gault and Heitowit (1963), and a descriptive part for the later stages of impact, based on field observations at the large terrestrial craters. The impacts of iron, stone, permafrost, and ice meteorites 1 km in diameter into crystalline, carbonate, dry sandstone, ice-saturated sand, and ice targets are modeled for velocities of 6.25, 17, and 24.6 km/s. Tables of calculated crater volume, depth of penetration of the meteorite, equivalent scaled depth of burst, radii to various peak pressure isobars, volume of silicate melt, and volume of water vapor (or, in the case of carbonate, carbon dioxide vapor) are presented. Simple algebraic expressions for pressure attenuation are derived: for the near field, $dX/dR = 3Xn/R(1 - n)$, where X is the pressure normalized to an averaged bulk modulus for the target rocks, R is the radius normalized to the radius of the cavity in which energy is initially deposited, and n is the pressure derivative of the bulk modulus. For the far field the pressure attenuation is given by $dX/dR = \sim -3X/R$. For most materials considered, $n = 4$–6, and therefore the near-field attenuation is proportional to $R^{-3.65}$–R^{-4} and the far-field attenuation is proportional to R^{-3}. The calculations show that the volume of material shocked to pressures sufficient for melting should not be significantly different in sedimentary and crystalline rocks. Hence we conclude that shock melt is formed in the early stages of the cratering process by impacts into rocks rich in volatiles but is destroyed by the cratering process. We propose that the melt is finely dispersed by the great expansion of shocked volatiles upon release from high pressure and that suevite units are the product of this process. The fragmented silicates produced by this process may react penecontemporaneously with the hot volatiles to produce hydrated minerals such as clays. This process may produce hydrothermally altered minerals in planetary regoliths, such as the Martian regolith. The dispersion of shock melt by volatile expansion may also account for the apparent lack of lunarlike melt sheets on the surface of Mars. Because large amounts of volatiles vaporize during impact and are transferred from depth either into space, into the atmosphere, or onto near-surface ejecta by condensation, repeated impact degasses a planet, depleting some layers in volatiles and, unless the volatiles escape the planet, enriching others.

CONTENTS

Paper number 9R1347.
0034-6853/80/009R-1347$06.00

INTRODUCTION

Although sediments, sedimentary rocks (including carbonates), water, and ice are major constituents of the outer crust of the earth, most theoretical cratering studies have been directed toward volatile-free rocks [*Gault and Heitowit,* 1963; *Shoemaker,* 1963; *O'Keefe and Ahrens,* 1975, 1976] and have not focused on the role of different rock types in the cratering process or their influence on the properties of the ejecta produced. In fact, major differences in the cratering process are produced by lithologic differences in either projectile or target, and particularly, the volume fraction of sedimentary components in the target has a major effect on the amount and distribution of impact melt in terrestrial craters. We present a model which accounts semiquantitatively for the effects of porosity and water and volatile content on the cratering process. Although the model was formulated for the purpose of synthesizing a wide variety of field observations at terrestrial craters and not for analytical rigor, it incorporates in a general way (1) the effects of the difference in compression and release adiabat properties between wet and dry and porous and non-

TABLE 1. Description of

	Diameter, km	Radiometric Date, m.y.	Oldest Cover	Youngest Cratered Material	Structural Type	Erosion
Puchezh-Katunki, USSR 57°06′N, 43°35′E	80	183 ± 3	Middle Silurian	Early Triassic	ring	ejecta gone
Popigai, USSR 71°30′N, 111°30′N	72	30	Quarternary	Triassic	ring	minor distal ejecta preserved
Manicouagan, Canada 51°30′N, 68°30′W	65	214 ± 5	Pleistocene	Ordovician	ring	into basal melt
Kara, USSR 69°10′N, 65°00′E	50	57	Quarternary	Late Cretaceous	central peak	
West Clearwater, Canada 56°13′N, 74°30′W	38	266 ± 15	Pleistocene	Middle-Upper Ordovician	central peak or ring	deep into fill
Charlevoix, Canada 47°32′N, 70°18′W	34	360 ± 25	Pleistocene	Middle Ordovician	central peak	only a trace of fill left
Mistastin, Canada 55°53′N, 63°10′E	25	38 ± 4	none	1345 m.y.	central peak	only a small amount of fill left
Boltysh, USSR 48°45′N, 32°10′E	25	70	Cretaceous	Precambrian	central peak	below rim
Kamenska, USSR 48°20′N, 40°15′E	25	Upper Cretaceous	Danian	Upper Cretaceous	central peak	?
Ries, West Germany 48°53′N, 10°37′E	24	14.8 ± 0.7	mid-Miocene	Tertiary	central peak	minor ejecta preserved
Strangways, Australia 15°12′S, 133°35′E	24		Cretaceous, Cambrian?	Proterozoic	central peak?	little crater fill preserved
East Clearwater, Canada 56°05′N, 74°07′W	23	266 ± 15	Pleistocene	Ordovician	central peak	into crater fill below top of uplift
Rochechouart, France 45°49′N, 87°40′W	23	150–170		Hercynian (275–300 m.y.)	central peak	only trace of fill left
Gosses Bluff, Australia 23°48′S, 132°18′E	22	130 ± 6	Quarternary	Carboniferous	central peak	almost all fill gone
Lake St. Martin, Canada 51°48′N, 98°30′W	22	200–250	Jurassic	Devonian	central peak	central peak
Steen River, Canada, 57°31′N, 117°38′W	22	95 ± 7	Lower Cretaceous	Precambrian	central peak	?
Jänis'järvi, USSR 61°58′N, 20°55′E	15	700	Pleistocene	Proterozoic	bowl on central peak	almost to crater floor
Kaluga, USSR 54°30′N, 36°10′E	15	415 ± 15	Upper Devonian	Middle Devonian	?	some of rim left

Craters Used in This Study

Cover	Drilling	Target Rocks	Deposits	Reference
400 m sediment in crater	5 holes	2 km of sediment, sandstone, carbonate, sulphate, and shale over granite gneiss	no melt sheet, no impactites, authigenic breccia of gneisses; some glass clasts are found, rocks resemble suevites	*Masaitis* [1975], *Firsov* [1965]
discontinuous Quarternary alluvium		1 km of sediment, 300 m of sandstone, 50 m of shale, and 600 m of limestone over gneisses	melt sheets interbedded with suevites in center suevites with interbedded >20 m thick tagamite sheets rings of uplifted gneisses overlain directly by tagamite sheets beyond rim; breccias with substantial sediment component have little glass	*Masaitis et al.*[1975], *Masaitis* [1975]
thin, Pleistocene	none	thin limestone over 4.5% anorthosite, 40.0% granitic, and 55.5% mafic gneisses amphibolite facies	melt sheet composition matches gneissic basement, melt sheet <200 m thick, discontinuous glass clast-bearing breccias, melt volume = 200–600 km^3 (2–4% of volume excavated)	*Currie* [1972], *Floran et al.* [1978], *Simonds et al.* [1978*a*]
100 m, Quarternary		folded terrigenous and carbonates of Paleozoic age	suevites, transitional to allogenic breccia with small bodies of massive impactite (bombs?); compositionally massive impactites match clay shales	*Masaitis* [1975]
thin, Pleistocene	4	gneiss of quartz diorite, quartz monzonite and diorite composition covered by thin Ordovician limestone	>130-m-thick melt sheet on ring of islands overlying ~10 m of glass-bearing fragmental breccia; estimated melt volume ~24 km^3, 4–5% of volume excavated	*Bostock* [1969], *Simonds et al.* [1978*b*]
nil	none	gneisses of granite, charnockitic and quartzdiorite composition covered by limestone	~2 of clast-laden melt left possibly in form of dikes	*Rondot* [1971]
nil	none	anorthosite, quartz diorite and mangerite crystalline rocks	80-m-thick melt sheet over discontinuous breccias; estimated volume of melt, 8 km^3. 3–5% of volume excavated	*Grieve* [1975]
70–100 m at edge	many	potassic granites	multiple melt sheets up to 200 m thick, variety of allogenic and authogenic breccias; melt composition matches granites	*Yurk et al.* [1975], *Masaitis* [1975]
200–300 m of sediments	yes	folded sediments, sandstones, limestones, shales and marls, largely limestone	500–650 m of breccia with arenaceous-argillaceous cement, central peak of brecciated Carboniferous strata	*Masaitis* [1975]
lake sediments + Pleistocene	13 for research	600 m of sediments, approximately equal portions of carbonate, shale, and sandstone	melt only in suevites as glass clasts, bombs, and possibly matrix; glass clast composition matches crystalline basement, melt volume = 0.1–0.5 km^3 0.05–0.25% of volume excavated; very little erosion of suevite-chilled top suevite preserved in places	*Pohl et al.* [1977]
50% by Cretaceous	none	Precambrian crystalline covered by sandstone, siltstone, minor shale, and limestone of unknown thickness	~15 m of clast-laden melt	*Guppy et al.* [1971]
limestone	2	thin limestone over quartz monzonite, granodiorite, diorite, and gabbro, ranging from massive to gneissic	fragmental rocks with igneous matrix, clast content decreases down from top of hole; bottom of sheet not penetrated by drilling	*Dence* [1964]
thin	no	granites, gneisses, and schists	impact melt (up to 3 m), red melt-rich breccia (0–10 m) non-glass-bearing polymict breccia (>30 m), glass bearing polymict breccia (>20 m)	*Kraut and French* [1971], *Lambert* [1977]
alluvium	2	>3000 m of sandstone, siltstone, and conglomerate; total depth to basement >8 km	single outcrop grading from breccia with planar elements in quartz clasts to a flowed zone, only uppermost target units involved	*Milton et al.* [1972]
~100 m	10	220 m of sediments, mostly carbonates, over massive granites and minor amphibolites	melt sheet 65 m thick in one locality; abundant carbonate, breccia and glass-bearing polymict breccia	*McCabe and Bannatyne* [1970] *Simonds and McGee* [1979]
1400 m, Cretaceous and younger	6	Precambrian crystallines	25 m melt, about 220 m of suevite and intensely fractured basement	*Winzer* [1972]
Pleistocene, thin	no	Proterozoic crystalline schists	sheet of melt over breccia	*Masaitis* [1975], *Eskola* [1921]
800 m	yes	sandstones, clay, siltstone, and marl over crystalline rocks	suevite and allogenic breccia, glass in allogenic breccia	*Masaitis* [1975]

TABLE 1.

	Diameter, km	Radiometric Date, m.y.	Oldest Cover	Youngest Cratered Material	Structural Type	Erosion
Wells Creek, United States 36°23′N, 87°40′W	14		mid-Cretaceous	Upper Mississippian	central peak	at base of excavation
Lappajarvi, Finland 63°09′N, 23°42′E	13		Pleistocene	Precambrian	?	deep into fill
Sierra Madera, United States 30°36′N, 102°55′W	13		Pleistocene	Lower Cretaceous	central peak	rim gone, erosion into central peak
Decaturville, United States 37°54′N, 92°42′W	5.5		nil	Ordovician	central peak	<47 m
Il'inets, USSR 48°45′N, 28°00′E	5	495 ± 5	Devonian	early Paleozoic	bowl?	deeply
Lake Mien, Sweden 56°25′N, 14°22′E	5	118 ± 2	Pleistocene	Precambrian	bowl?	into fill, some melt preserved
Mishingorsk, USSR 58°40′N, 28°15′E	4.5			Middle Devonian	bowl?	
Brent, Canada 46°05′N, 78°29′W	3.8	414 ± 20	Ordovician	Cambrian dikes	bowl	below rim, fill left
Flynn Creek, United States 36°16′N, 85°37′W	3.6		Upper Devonian	Upper Ordovician	central peak	ejecta gone
Steinheim, West Germany 48°02′N, 10°4′E	3.5		Upper Mid-Jurassic	Upper Jurassic	central peak	
Gusev, USSR 48°20′N, 40°00′E	3		Danian	Upper Cretaceous	bowl	?
West Hawk Lake, Canada 49°46′N, 95°11′W	2.7		Pleistocene	Keewatin	bowl	below rim
Lonar, India 19°58′N, 76°31′E	1.83		Pleistocene	Cretaceous-Eocene	bowl	a few tens of meters
Meteor, United States 35°02′N, 111°01′W	1.2		mid-Wisconsin	Triassic	bowl	a few tens of meters

porous sediments (including carbonates), (2) the effects of composition and lithology on the impact melting properties of the rocks, and (3) the effects of the varying heat capacities of the rocks on late-stage digestion and melting of included clasts.

Some of the interesting, and potentially predictable, properties of an impact crater are its size and shape, the distribution of shock effects, and the amount and distribution of melt; the relation of these properties to the mass, velocity, and composition of the meteorite and the composition and thermodynamic and mechanical properties of the target. In order to evaluate these various dependences we have developed the model which follows. Although we cannot assign numerical uncertainties to our conclusions, we have tried to indicate the strengths and weaknesses of the model and to distinguish those conclusions that are relatively independent of the assumptions and those that are strongly dependent on them.

Our considerations are focused primarily on the volume of impact melt generated as a function of target lithology because this is a quantity which can be documented by field study. Prediction of the amount of impact melt generated is not only important in the study of terrestrial craters but is necessary to compare the amount of melt generated under other planetary environments: in the anhydrous lunar crust [*Lunar Sample Preliminary Examination Team,* 1969]; in the presumably anhydrous crust of Mercury [*Adams and McCord,* 1977]; in the crust of Mars, possibly rich in carbonate or clay [*Toulmin et al.,* 1977] or permafrost [*Carr and Schaber,* 1977; *Lambert and Chamberlain,* 1978; *Soderblom and Wenner,* 1978]; and, perhaps, in the volatile-rich crusts of the satellites of the outer planets [*Ostro and Pettengill,* 1978; *Consolmagno and Lewis,* 1978]. As a specific example of large-scale effects which may be lithology-dependent we note that *Carr et al.* [1976, 1977], *Head and Roth* [1976], and *Gault and Greeley* [1978] have suggested that the distinctive lobate features on the continuous ejecta blankets of Martian rampart craters arise from fluidization of permafrost during the impact and transport processes.

FIELD OBSERVATIONS OF THE OCCURRENCE OF IMPACT MELT

In the attempt to determine the extent to which target rock types determine the nature of the impact-produced deposits it

(Continued)

Cover	Drilling	Target Rocks	Deposits	Reference
	?	432 m of sediments, ~75% carbonate and ~25% shale	brecciated county rocks, without wollastonite or high-pressure silicate polymorphs	*Stearns et al.* [1968]
glacial	no	Precambrian	melt sheet	
nil	16	>10 km of sediments (~3.6 km of carbonates), >2.0 km of shales >0.5 km sandstone	polymict and monomict breccias; polymict breccias lack melt or glass and occur in dikes or shear zones	*Wilshire et al.* [1972]
nil	yes	540 m of sediments (mostly carbonate) over crystalline basement	polymict breccias lacking indiction of shock pressures >100 kbar	*Offield and Pohn* [1977]
thin	no	granites, gneisses covered by some lower Paleozoic sands	200–250 m of suevite with glasses and impactites	*Masaitis* [1975]
3–5 m of fill	2	granitic gneiss	20–25 m of clast-laden melt over ~2 m of glass clast–laden polymict breccia, suevite in glacial fill but not in place	*Stanfors* [1969]
		>500 m of sediments, extensive carbonates over crystalline rocks (gneisses and schists)	breccia (>700 m) of sediments diaplectic minerals of crystalline rocks, some glass	*Masaitis* [1975]
Ordovician sediments	12	quartz feldspar gneisses of granodiorite composition	35-m melt zone, coarsest at center before finer and more clast-rich to top and bottom >600 m of melt-bearing breccias (suevite)	*Hartung et al.* [1971], *Grieve* [1978]
>100 m of Devonian-Mississippian	yes	>450 m of sediments dominantly carbonate	40 m of polymict carbonate breccia, nothing melted	*Roddy* [1968]
sediments in depression Pleistocene	25	540 m of Jurassic carbonates over Triassic sandstones	brecciated limestones, shock pressure ≤100 kbar	*Reiff* [1977]
200–300 m of sediments	yes	sediments largely limestone	breccia with sedimentary (sand-clay) matrix	*Masaitis* [1975]
thin Pleistocene	4	micaschists, to granitic gneisses of andesitic and sandstone composition	329 m of breccia, >200 m of ruptured rock, zones with abundant glass fragments in center of structure, with isotopic material in the matrix	*Short* [1970]
100 m of lake fill	>3	Deccan basalt flows, each 10–30 m thick, top of flows, vesicular and weathered flow tops	upper unit with variably shocked well-mixed ejecta with a few percent of melt; lower unit of unshocked, unmixed debris	*Fredriksson et al.* [1973]
~3 m of lake sediments	>5	9–15 m of red sandstone, 80 m of carbonate, 210–240 of quartzite sandstone	165 m of polymict breccia including some glass	*Shoemaker* [1963]; *Shoemaker and Kieffer* [1974]

is, in principle, necessary to separate the effects of target properties (particularly the porosity and the volatile content) from those of the impacting body. The wide range of impact velocities, shapes, and trajectories and the narrower, but still significant, range of compositions and densities (1–8 g/cm^3) of meteorites could have a significant effect on the cratering process. Because, in practice, these variables cannot be specified for most structures, we have considered a large number of structures, believing that thereby the effects of variation in the properties of the meteorites will be averaged out.

General properties of 32 terrestrial impact structures are summarized in Table 1. These 32 structures were selected from a total of 65 that have diameters greater than 1 km and for which diagnostic shock features have been observed (list provided by M. R. Dence (personal communication, 1978)). The 32 structures are the least eroded ones for which descriptions of the structure of the crater, the target rocks, and ejecta are available. The following properties are listed in the table:

1. Diameters of the outer edge of the topographic depression for simple bowl-shaped structures and of the outer edge of the primary structural depression for ring and central peak structures. These dimensions are larger than the initial or transient cavity before slumping or other modification. The diameter of the initial excavation is poorly defined for the craters in crystalline rocks because structural relations are generally not clear enough for the transient cavity to be defined. Published estimates of the diameter of the initial or transient cavity are available for only a few craters: Manicouagan, 22 km [*Floran and Dence*, 1976], West Clearwater Lake, 17 km [*Grieve et al.*, 1977], Ries, 12 km [*Pohl et al.*, 1977], Mistastin, 12 km [*Grieve et al.*, 1977], and Brent, 3.8 km [*Grieve et al.*, 1977].

2. Radiometric ages, typically derived from an impact melt unit, quoted only with the analytical error limits. Many of the published ages are whole-rock K-Ar ages which are suspect because of incomplete degassing, as was discussed by *Jessberger et al.* [1974].

3. Stratigraphic ages of the youngest material cratered and of the oldest covering material.

4. Crater type: simple bowl shaped, central peak, or ring structure.

5. Degree of erosion.

6. Degree of cover.

7. Number of drill holes. (Note that properties 5, 6, and 7

indicate in a general way the quality of information available on the crater.)

8. Target rocks: thickness of sedimentary rocks, lithology of sediments, and lithology of crystalline rocks.

9. Description of ejecta deposits, particularly the occurrence and nature of melt deposits. Small outcrops of igneous rocks within the craters are considered to be indicative of melt sheets that have not been totally removed by erosion.

A detailed reading of Table 1 shows that all of the craters that formed primarily in crystalline rocks have melt sheets as-

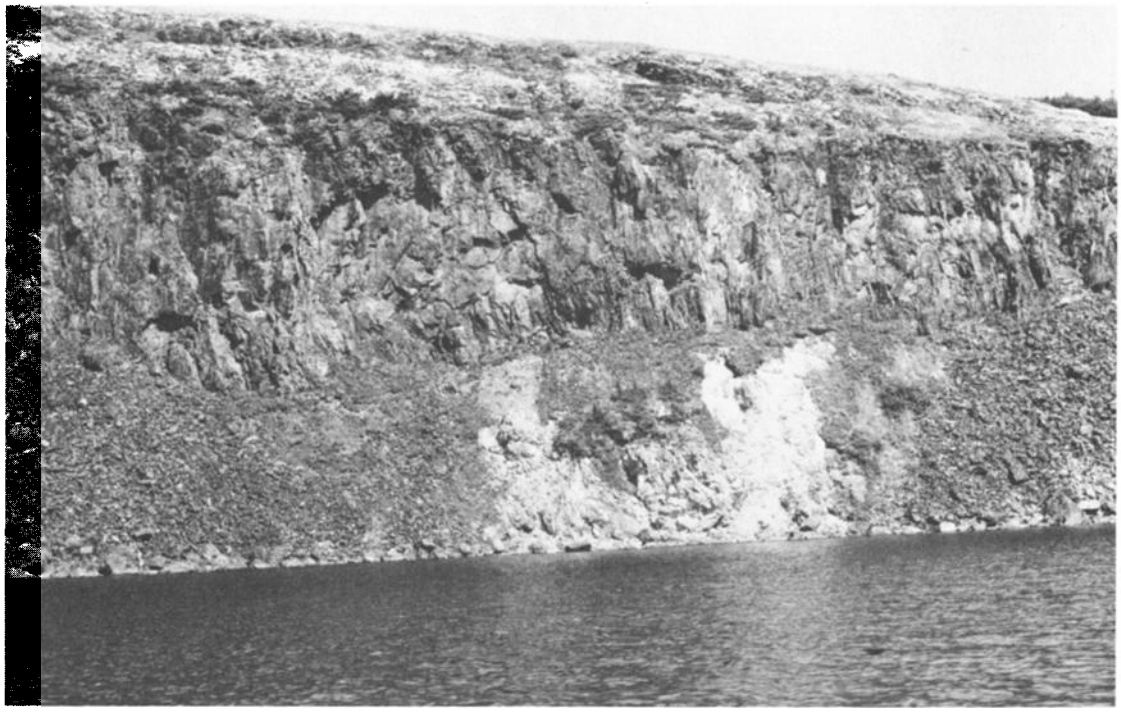

Fig. 1*a*

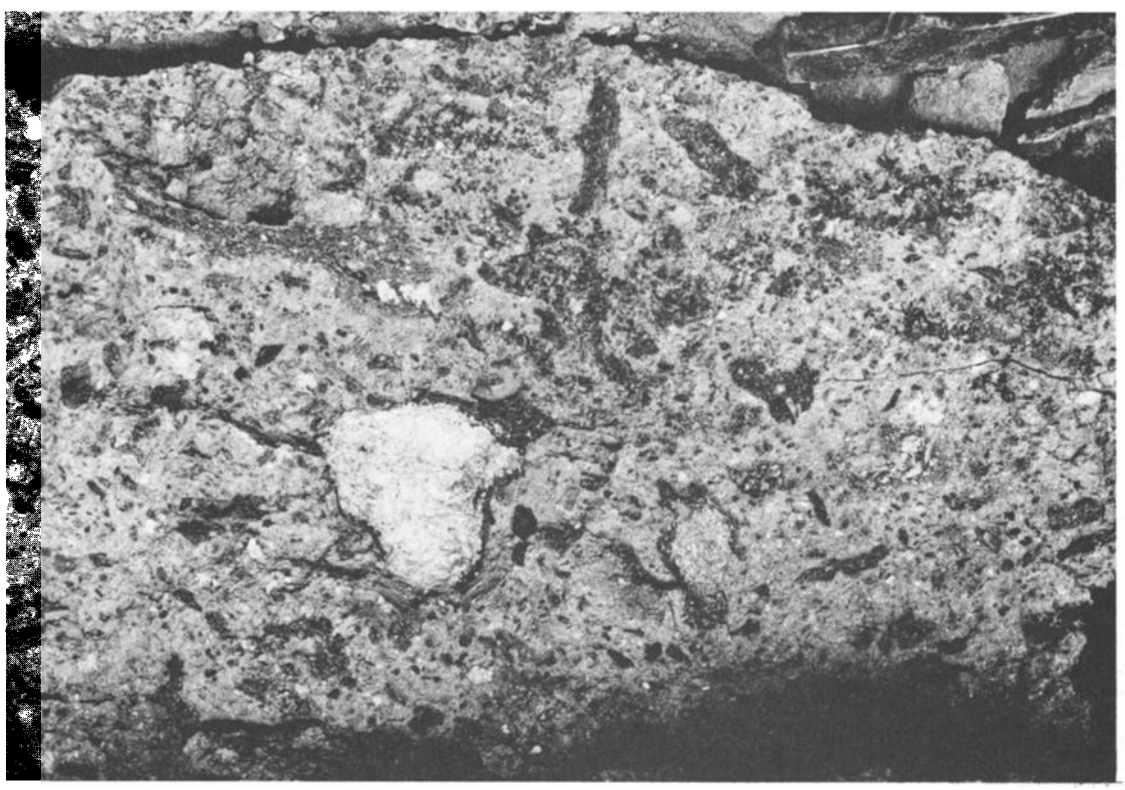

Fig. 1*b*

Fig. 1. (*a*) Exposure of impact melt sheet (cliff unit) at West Clearwater, Quebec, impact structure overlying melt-bearing polymict breccia and brecciated basement. Cliff of melt unit is 15 m high. (*b*) Exposure of suevite in Otting quarry, the Ries crater, Germany (hammer head in upper right corner for scale).

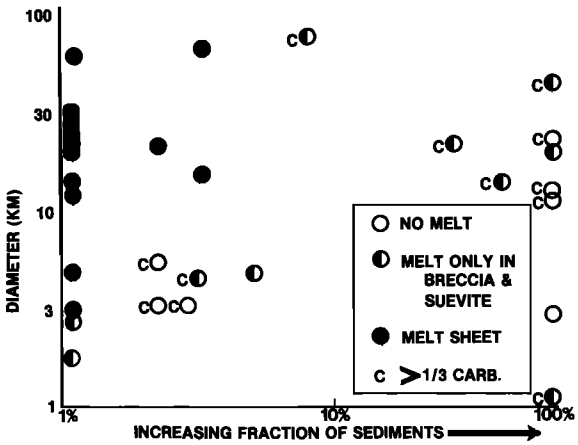

Fig. 2. Summary of the occurrence of impact melt in terrestrial craters. Note that melt sheets occur only at craters with little or no sedimentary cover and that they occur in craters of differing diameters.

sociated with them, except the two smallest, West Hawk Lake and Lonar. A typical melt sheet exposure is shown in Figure 1*a*. In contrast, no craters formed primarily within sedimentary rocks have melt sheets associated with them. Furthermore, the melt found at craters in sedimentary rocks (e.g., Ries and Popigai) has been shown generally to have the composition of the crystalline basement rocks, not of the sedimentary cover [*Pohl et al.*, 1977; *Stähle*, 1972; *von Engelhardt*, 1972; *Masaitis et al.*, 1975]. These observations are summarized in Figure 2. The field evidence is compelling that melt sheets are generally not present at craters in carbonate rocks, shale, or sandstone, but only at craters in crystalline rocks. In view of the large amount of compression and shock heating of porous rocks [*Anderson et al.*, 1966; *Kieffer*, 1971; *Ahrens and Cole*, 1974] and the relatively low pressures required for melting of wet porous rocks (e.g., 300 kbar for nearly total melting of wet Coconino sandstone [*Kieffer et al.*, 1976*a*]) in comparison with dry crystalline rocks (e.g., 800–1000 kbar for nearly total melting of basalt [*Kieffer et al.*, 1976*b*]) the absence of melt sheets around craters in sedimentary rocks is unexpected in terms of current models of cratering. The problem addressed in this paper is whether the variation in abundance and form of impact melt reflects the melting behavior of the various target rock types or differing fates of the melt.

Observations at a few of the better studied structures allow an estimate to be made of the degree to which melt appears to be lacking at the craters in sedimentary rocks. *Grieve et al.* [1977] estimated the following volume percentages of melt at craters in crystalline rocks: 1–2% of the volume excavated at the 4-km-diameter Brent structure, 3–5% at the 28-km Mistastin, 4–5% at the 38-km West Clearwater, and 2–4% at the 65-km Manicouagan. These estimates are based on the volume of the transient cavity, not the diameter of the larger modified structure. *Grieve et al.* [1977] noted and discussed the possibility that errors in the estimates of initial cavity volumes cause significant error in estimated melt fraction. Although errors of perhaps a factor of 2 are possible in estimates of the transient cavity volume, errors of this magnitude do not significantly affect our conclusions below. Grieve et al. used maximum volumes for their transient cavities, and therefore the above percentages represent minimum melt fractions (if the volume of melt in the field has been estimated correctly).

In contrast to the presence of a few percent melt in the crystalline rock craters, *Pohl et al.* [1977] report 0.05–0.4% melt at the 24-km Ries Crater (which had a sedimentary cover about 0.65 km thick overlying crystalline rocks). This melt is not in the form of a melt sheet but in the form of bombs and drops (closely similar to the basement rock in composition) included in the suevite; one possible exception in melt composition at the Ries is discussed below.

Thus we conclude that the proportion of melt present at the craters in sedimentary rocks is at least 2 orders of magnitude less than that in similar-sized craters in crystalline rocks. *Grieve et al.* [1977, p. 809] suggested that some differences in melt abundance are associated with crater size and arise from differing attenuation rates. However, plausible ranges of attenuation models ($P \propto r^{-3}$ to $P \propto r^{-4.5}$, where P is pressure and r is radius) give variations of only a factor of 2 in melt abundance when they are applied to their crystalline crater models; similar results would be expected for craters in sedimentary rocks.

Limited data on siderophile and volatile trace elements in larger craters reveal that impacts of both stony and iron meteorites formed melt. *Janssens et al.* [1977] inferred an iron meteorite for Rochechouart, a 23-km crater with a melt sheet. *Palme et al.* [1978] suggested a chondritic meteorite for the 23-km East Clearwater crater but were unable to identify any projectile-induced contamination at West Clearwater, Mistastin, or Manicouagan. *Morgan et al.* [1979] reported modest enrichments at the Ries which could be ascribed to an achondrite. Therefore the limited evidence available suggests that meteorite lithology alone does not account for the variation in melt abundance.

Although a number of factors other than lithology could affect the amount of melt formed at impact sites (e.g., meteorite shape, angle of incidence, and, of course, impact velocity), we can think of none that would produce the consistent difference that we observe in the terrestrial craters, and we have therefore assumed that these other possible effects have been averaged out in our overview of many different craters. We examine here simply the roles of meteorite and target lithology and volatile content.

A critical point discussed later in the paper is the mode of transport of melt during the cratering of different rock types. A significant difference between craters in sedimentary rocks and craters in crystalline rocks is the occurrence of suevite units at craters in sediments or with thick sections of sediment overlying crystalline basement (e.g., Puchezh-Katunki, Popigai, Kara, Ries, Steen River, Jänis'järvi, and Il'inets). A notable exception is the bowl-shaped, 1.3-km Meteor (Barringer) Crater. We utilize as the definition of suevite, 'a grayish or

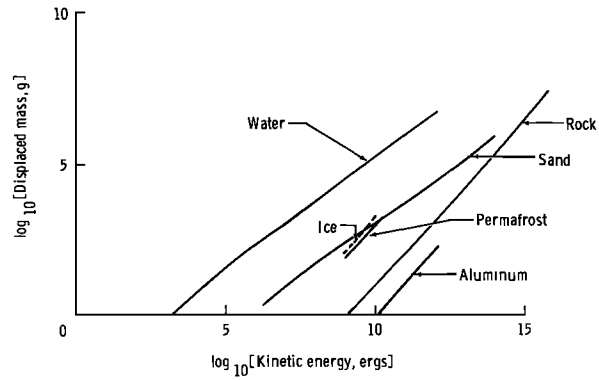

Fig. 3. Energy-mass relations for craters formed in targets of differing strengths and materials. Data are modified from *Gault and Moore* [1965] and, for ice and permafrost, from *Croft et al.* [1979].

TABLE 2*a*. Impact Parameters: $v_i = 6.25$ km/s

	Meteorite					
	Iron	Aluminum	Diabase	Basalt	Permafrost	Ice
			Iron			
P	2150	1230	1170	1130	780	440
u_t	3.1	2.2	2.1	2.0	1.6	1.0
f	0.50	0.46	0.45	0.44	0.38	0.27
p/r_{0m}	1.42	0.82	0.90	0.84	0.76	0.42
r_{0t}/r_{0m}	1.00	0.87 (1.10)	0.91 (1.15)	0.92 (1.16)	0.90 (1.13)	0.85 (1.08)
r_0/r_{0m}	1.26	1.12 (1.41)	1.19 (1.50)	1.21 (1.52)	1.24 (1.56)	1.31 (1.65)
			Aluminum			
P	1230	820	795	750	580	350
u_t	4.1	3.1	3.0	2.9	2.4	1.7
f	0.45	0.50	0.50	0.50	0.47	0.40
p/r_{0m}	2.28	1.30	1.44	1.44	1.28	0.82
r_{0t}/r_{0m}	1.14	1.00	1.06	1.06	1.04 (1.31)	0.96 (1.21)
r_0/r_{0m}	1.49	1.26	1.33	1.34	1.34 (1.69)	1.31 (1.65)
			Diabase			
P	1170	800	770	730	550	340
u_t	4.1	3.2	3.1	3.0	2.5	1.7
f	0.45	0.50	0.50	0.50	0.48	0.40
p/r_{0m}	2.28	1.36	1.52	1.52	1.36	0.82
r_{0t}/r_{0m}	1.11	0.95	1.00	1.00	1.00 (1.25)	0.94 (1.18)
r_0/r_{0m}	1.45	1.20	1.26	1.26	1.26 (1.60)	1.26 (1.60)
			Basalt			
P	1130	750	730	680	510	310
u_t	4.2	3.3	3.2	3.1	2.6	1.9
f	0.44	0.50	0.50	0.50	0.49	0.42
p/r_{0m}	2.38	1.42	1.58	1.64	1.44	0.94
r_{0t}/r_{0m}	1.10	0.95	1.00	1.00	1.00 (1.25)	0.90 (1.13)
r_0/r_{0m}	1.45	1.20	1.26	1.26	1.26 (1.58)	1.20 (1.20)
			Carbonate			
P	1120	750	730	680	520	320
u_t	4.2	3.3	3.2	3.1	2.6	1.9
f	0.44	0.50	0.50	0.50	0.49	0.42
p/r_{0m}	2.38	1.42	1.62	1.60	1.44	0.94
r_{0t}/r_{0m}	1.13	0.98	1.02	1.03	1.02	0.92 (1.16)
r_0/r_{0m}	1.48	1.23	1.28	1.29	1.28	1.22 (1.54)
			Granite			
P	1040	720	690	650	500	310
u_t	4.3	3.4	3.3	3.2	2.7	2.0
f	0.43	0.50	0.50	0.50	0.49	0.43
p/r_{0m}	2.50	1.48	1.66	1.70	1.52	1.00
r_{0t}/r_{0m}	1.10	0.96	1.01	1.02	0.99	0.90 (1.13)
r_0/r_{0m}	1.47	1.21	1.27	1.28	1.26	1.19 (1.50
			Permafrost			
P	770	580	550	510	400	260
u_t	4.7	3.9	3.8	3.6	3.1	2.4
f	0.37	0.47	0.48	0.49	0.50	0.47
p/r_{0m}	3.00	1.84	2.06	2.08	1.92	1.32
r_{0t}/r_{0m}	1.10	0.94	1.00	1.02	1.00	0.90
r_0/r_{0m}	1.52	1.21	1.28	1.30	1.26	1.17
			Dry Coconino Sandstone			
P	770	550	530	500	390	250
u_t	4.7	3.9	3.8	3.7	3.2	2.5
f	0.37	0.47	0.48	0.48	0.50	0.48
p/r_{0m}	3.00	1.84	2.06	2.20	1.98	1.40
r_{0t}/r_{0m}	1.09	0.94	0.99	0.99	0.98	0.88
r_0/r_{0m}	1.52	1.21	1.26	1.27	1.23	1.13
			Dry Sand			
P	630	480	550	430	340	220
u_t	4.9	4.1	4.1	3.9	3.4	2.7
f	0.34	0.45	0.45	0.47	0.50	0.49
p/r_{0m}	2.30	1.98	2.32	2.44	2.20	1.58
r_{0t}/r_{0m}	1.11	0.97	0.99	1.02	1.01	0.90
r_0/r_{0m}	1.59	1.26	1.29	1.32	1.28	1.15

TABLE 2*a*. (continued)

	Meteorite					
	Iron	Aluminum	Diabase	Basalt	Permafrost	Ice
			Ice			
P	440	350	340	310	260	180
u_t	5.2	4.6	4.5	4.3	3.9	3.1
f	0.28	0.39	0.40	0.43	0.47	0.50
p/r_{0m}	3.80	2.44	2.74	2.98	2.80	2.02
r_{0f}/r_{0m}	1.21	1.03	1.09	1.13	1.09	1.00
r_0/r_{0m}	1.84	1.40	1.47	1.49	1.40	1.26

P is the initial pressure (one-dimensional approximation) in kilobars, given to two or three significant figures. Parameter u_t is the initial particle velocity in the ground, relative to a stationary coordinate system, in kilometers per second. The projectile particle velocity, relative to the ground, is $u_p = v_i - m$, where v_i is the impact velocity. Velocities are given only to the nearest 0.1 km/s. Parameter f is the fraction of the initial meteorite energy transferred to the ground during the time taken by the shock to traverse from the front to the back of the meteorite; p/r_{0m} is the penetration of the interface during stage 2, relative to the initial meteorite radius; r_{0f}/r_{0m} is the radius of a target sphere into which f of the initial energy is deposited, relative to the initial meteorite radius, at initial pressure P; and r_0/r_{0m} is the radius of a target sphere into which 100% of the initial energy is deposited, relative to the initial radius, at initial pressure P.

yellowish fragmental rock (depositional breccia) that is associated with meteoritic craters and that contains both shock metamorphosed rock fragments and glassy inclusions that occur typically as aerodynamically shaped bombs' [*Gary et al.*, 1974, p. 710]. Figure 1*b* shows an example from the Ries. In the subsequent discussion we differentiate between suevites and glass-bearing polymict breccias by using three features: (1) their clay matrix, which gives them their distinctive color; (2) the presence of aerodynamically shaped bombs; and (3) their occurrence in positions stratigraphically equivalent to the melt sheet, that is, overlying a mixed breccia unit. For example, at the Ries, the suevite outside of the crystalline ring (e.g., at Otting) lies on top of the Bunte breccia (a melt-free, polymict breccia); the suevite inside the crater (e.g., in the Nördlingen drill core) is on top of a polymict crystalline breccia that contains melt. The exterior and interior suevites of the Ries differ somewhat in their characteristics. Two important differences noted by *Stöffler* [1977] are that melt particles included in the interior suevite are very small in comparison to those in the exterior suevite and they are extremely vesiculated and hydrothermally altered. Whereas, as was noted above, it is generally accepted that the glassy bombs found in the suevite (generally in the exterior suevite) have the same composition as the crystalline basement rocks and are derived from them [*von Engelhardt*, 1972], *Stöffler* [1977] suggested that the melt particles in the interior suevite might be derived from the lowermost sedimentary strata and that the assumed high water content of these strata would account for the small size of the melt inclusions and their extreme vesicularity.

Suevite is present at craters formed largely in sedimentary strata and at craters in mixed targets (at the 72-km Popigai with its overburden (1 km) of sediments [*Masaitis et al.*, 1975] and perhaps at the 22-km Lake St. Martin, which had 220 m of carbonate overlying the basement [*McCabe and Bannatyne*, 1970]; in this case the unit that may be suevite is a nearly clay-free breccia resembling the interior suevite of the Ries as observed in the 1973 Nördlingen core). It is not possible to demonstrate the presence or absence of suevite at craters wholly in crystalline rocks because these craters are all too deeply eroded for such deposits to have been preserved outside the structural rim. We do not consider the polymict breccias underlying melt sheets or occurring as dikes penetrating the basement to be suevites: they have less clay than, for example, the Ries suevite and lack aerodynamically shaped glass bombs [*Floran et al.*, 1978; *Grieve*, 1975; *Simonds, et al.*, 1978*b*].

Because of the depth of excavation at the craters, we assume that to a large extent any sediments present were saturated with groundwater. (Although crystalline rocks may also have been saturated, they hold only a few percent water, whereas porous sediments may contain 20% water in their pores.) This assumption is supported by evidence (even at the relatively small Meteor Crater) that many craters were filled with lakes shortly after the impact event. Thus in considering the role of target lithology we are confronted with the problem of comparing crystalline rocks not only with their porous equivalents but also with porous sediments rich in volatile phases, either water or carbon dioxide produced at high pressure by decarbonation of carbonates.

In addition to the field observations at naturally formed impact craters, data from explosion craters [*Cooper*, 1977], missile impact craters [*Moore*, 1976], and laboratory cratering events [*Gault and Moore*, 1965] demonstrate that target lithology is important in determining crater properties (Figure 3). These data suggest that even in relatively small craters the role of lithology is important. As a rule, craters in soils are larger than energy-equivalent craters in crystalline rocks, and craters in water-saturated sediments are typically 20–50% larger in diameter (1.5–6 times larger in volume) than their energy equivalents in dry soils (see, for example, *Moore* [1976, Figure 53]). However, even if we assume that the volume of melt produced is comparable in craters in sedimentary and crystalline rocks, the percentage of melt produced in craters in sedimentary rocks would be reduced only by a factor of 1.5–6 because of the larger crater volume. Therefore the effect of lithology on crater size alone cannot explain the 2 orders of magnitude difference in melt fraction observed.

A Model for the Cratering Process

We present below a model for the vertical impact of a roughly spherical meteorite 1 km in diameter. A meteorite of this size, of density 3.0 g/cm^3, and of velocity 24.6 km/s has a kinetic energy of 4.75×10^{27} ergs and will produce a transient (premodified) crater about 15–20 km in diameter, depending on the target lithology and scaling laws used (the above values

TABLE 2*b*. Impact Parameters: $v_i = 17$ km/s

	Meteorite					
	Iron	Aluminum	Diabase	Basalt	Permafrost	Ice
			Iron			
P	11,500	6200	5980	6340	4370	2690
u_t	8.5	6.0	5.9	6.0	4.9	3.6
f	0.50	0.45	0.45	0.46	0.41	0.33
p/r_{0m}	1.98	1.16	1.34	1.18	1.08	0.64
r_{0t}/r_{0m}	1.00	0.87	0.90	0.87	0.85 (1.07)	0.75 (0.95)
r_0/r_{0m}	1.26	1.13	1.17	1.13	1.14 (1.44)	1.09 (1.37)
			Aluminum			
P	6200	3960	3840	3970	2950	1970
u_t	11.0	8.5	8.4	8.5	7.2	5.5
f	0.46	0.50	0.50	0.50	0.49	0.44
p/r_{0m}	3.32	2.00	2.24	2.02	1.86	1.14
r_{0t}/r_{0m}	1.17	1.00	1.04	1.02	1.00	0.88
r_0/r_{0m}	1.51	1.26	1.31	1.29	1.26	1.17
			Diabase			
P	5980	3840	3780	3840	2870	1940
u_t	11.1	8.6	8.5	8.6	7.3	5.8
f	0.45	0.50	0.50	0.50	0.49	0.44
p/r_{0m}	3.38	2.04	2.32	2.12	1.90	1.22
r_{0t}/r_{0m}	1.11	0.96	1.00	0.97	0.95	0.83
r_0/r_{0m}	1.45	1.21	1.26	1.22	1.22	1.10
			Basalt			
P	6340	3970	3840	3980	2920	1940
u_t	11.0	8.5	8.4	8.5	7.2	5.8
f	0.46	0.50	0.50	0.50	0.49	0.44
p/r_{0m}	3.38	2.00	2.24	2.08	1.86	1.20
r_{0t}/r_{0m}	1.15	0.98	1.04	1.00	0.99	0.86
r_0/r_{0m}	1.48	1.25	1.31	1.26	1.26	1.12
			Carbonate			
P	5940	3770	3660	3770	2810	1880
u_t	11.1	8.7	8.5	8.7	7.3	5.8
f	0.45	0.50	0.50	0.50	0.49	0.45
p/r_{0m}	3.38	2.08	2.32	2.16	1.94	1.24
r_{0t}/r_{0m}	1.16	1.00	1.04	1.00	0.99	0.87
r_0/r_{0m}	1.52	1.25	1.31	1.26	1.26	1.14
			Granite			
P	5450	3540	3430	3540	2650	1790
u_t	11.4	9.0	8.8	9.0	7.6	6.0
f	0.49	0.50	0.50	0.50	0.49	0.46
p/r_{0m}	3.60	2.20	2.48	2.32	2.08	1.30
r_{0t}/r_{0m}	1.17	0.98	1.02	0.99	0.97	0.87
r_0/r_{0m}	1.49	1.23	1.28	1.25	1.22	1.12
			Permafrost			
P	4370	2950	2870	2920	2180	1550
u_t	12.1	9.8	9.7	9.8	8.5	7.0
f	0.41	0.49	0.49	0.49	0.50	0.48
p/r_{0m}	4.20	2.58	2.88	2.74	2.52	1.62
r_{0t}/r_{0m}	1.18	1.02	1.06	1.03	1.00	0.87
r_0/r_{0m}	1.59	1.29	1.34	1.31	1.26	1.11
			Dry Coconino Sandstone			
P	4546	3030	2920	2990	2280	1550
u_t	12.0	9.7	9.5	9.7	8.4	6.8
f	0.41	0.49	0.49	0.49	0.50	0.48
p/r_{0m}	4.10	2.54	2.84	2.68	2.46	1.58
r_{0t}/r_{0m}	1.18	1.02	1.06	1.03	1.00	0.87
r_0/r_{0m}	1.59	1.29	1.34	1.31	1.26	1.11
			Dry Sand			
P	3690	2570	2510	2530	1970	1390
u_t	12.6	10.4	10.2	10.3	9.0	7.5
f	0.38	0.48	0.48	0.48	0.50	0.49
p/r_{0m}	4.68	2.90	3.24	3.06	2.80	1.86
r_{0t}/r_{0m}	1.19	1.05	1.09	1.06	1.02	0.90
r_0/r_{0m}	1.66	1.33	1.39	1.35	1.29	1.13
			Ice			
P	2690	1970	1940	1940	1550	1125
u_t	13.4	11.5	11.2	11.2	10.0	8.5
f	0.33	0.44	0.45	0.45	0.48	0.50
p/r_{0m}	5.64	3.58	3.96	3.74	3.46	2.34
r_{0t}/r_{0m}	1.32	1.13	1.21	1.18	1.14	1.00
r_0/r_{0m}	1.90	1.49	1.57	1.54	1.46	1.26

TABLE 2c. Impact Parameters: $v_i = 24.6$ km/s

	Meteorite					
	Iron	Aluminum	Diabase	Basalt	Permafrost	Ice
			Iron			
P	22,500	12,000	11,500	12,800	8600	5500
u_t	12.3	8.7	8.5	8.8	7.1	5.4
f	0.50	0.45	0.5	0.46	0.41	0.34
p/r_{0m}	2.12	1.26	1.44	1.24	1.14	0.70
r_{0t}/r_{0m}	1.00	0.87	0.93	0.87	0.85	0.74 (0.93)
r_0/r_{0m}	1.26	1.13	1.17	1.12	1.14	1.06 (1.33)
			Aluminum			
P	12,000	7500	7300	7800	5800	4000
u_t	15.9	12.3	12.1	12.4	10.4	8.3
f	0.46	0.50	0.50	0.50	0.49	0.45
p/r_{0m}	3.62	2.22	2.50	2.22	2.00	1.24
r_{0t}/r_{0m}	1.17	1.00	1.04	1.00	0.99	0.86
r_0/r_{0m}	1.51	1.26	1.31	1.27	1.26	1.13
			Diabase			
P	11,500	7300	7100	7500	5600	3900
u_t	16.1	12.5	12.3	12.7	10.6	8.5
f	0.45	0.50	0.5	0.50	0.49	0.45
p/r_{0m}	3.76	2.28	2.58	2.28	2.06	1.28
r_{0t}/r_{0m}	1.11	0.96	1.00	0.97	0.95	0.83
r_0/r_{0m}	1.45	1.21	1.26	1.22	1.21	1.09
			Basalt			
P	12,800	7800	7500	7900	5900	4000
u_t	15.8	12.2	11.9	12.3	10.4	8.4
f	0.46	0.50	0.50	0.50	0.49	0.45
p/r_{0m}	3.52	2.16	2.42	2.18	1.96	1.24
r_{0t}/r_{0m}	1.16	1.00	1.04	1.00	0.99	0.86
r_0/r_{0m}	1.50	1.26	1.31	1.26	1.26	1.12
			Carbonate			
P	11,500	7300	7100	7600	5600	3800
u_t	16.1	12.5	12.3	12.6	10.7	8.6
f	0.45	0.5	0.50	0.50	0.49	0.45
p/r_{0m}	3.74	2.28	2.58	2.28	2.10	1.32
r_{0t}/r_{0m}	1.16	1.00	1.04	1.00	0.99	0.86
r_0/r_{0m}	1.52	1.26	1.31	1.26	1.26	1.12
			Granite			
P	10,600	6800	6600	7100	5300	3600
u_t	16.5	13.0	12.8	13.0	11.1	9.0
f	0.44	0.50	0.50	0.50	0.50	0.46
p/r_{0m}	3.98	2.46	2.76	2.44	2.22	1.40
r_{0t}/r_{0m}	1.13	0.98	1.02	0.99	0.97	0.84
r_0/r_{0m}	1.49	1.23	1.28	1.25	1.22	1.09
			Permafrost			
P	8600	5800	5600	5900	4400	3200
u_t	17.5	14.2	14.0	14.2	12.3	10.2
f	0.41	0.49	0.49	0.49	0.50	0.48
p/r_{0m}	4.58	2.86	3.24	2.88	2.68	1.70
r_{0t}/r_{0m}	1.18	1.02	1.06	1.03	1.00	0.87
r_0/r_{0m}	1.59	1.29	1.34	1.31	1.26	1.11
			Dry Coconino Sandstone			
P	9000	6000	5800	6100	4600	3200
u_t	17.2	13.8	13.6	13.9	12.0	9.9
f	0.42	0.49	0.49	0.49	0.50	0.48
p/r_{0m}	4.44	2.74	3.10	2.78	2.66	1.62
r_{0t}/r_{0m}	1.19	1.02	1.06	1.03	1.00	0.87
r_0/r_{0m}	1.59	1.30	1.35	1.31	1.27	1.11
			Dry Sand			
P	7400	5000	4900	5200	4000	2900
u_t	18.0	14.8	14.6	14.8	12.9	10.8
f	0.39	0.48	0.48	0.48	0.50	0.49
p/r_{0m}	5.06	3.16	3.56	3.20	2.92	1.90
r_{0t}/r_{0m}	1.21	1.05	1.09	1.06	1.02	0.90
r_0/r_{0m}	1.66	1.34	1.39	1.35	1.29	1.13
			Ice			
P	5500	4000	3900	4000	3200	2300
u_t	19.2	16.3	16.1	16.2	14.4	12.3
f	0.35	0.45	0.45	0.45	0.49	0.50
p/r_{0m}	6.12	3.86	4.34	3.94	3.62	2.40
r_{0t}/r_{0m}	1.36	1.16	1.21	1.18	1.16	1.00
r_0/r_{0m}	1.93	1.52	1.57	1.59	1.47	1.26

TABLE 3. Excavated Volume for 1-km-Diameter Diabase Meteorite and Various Targets

Velocity, km/s	P, kbar	V_{melt} km³	Scaled Depth of Burst*	Excavated Volume, km³											
				1/ 250†	1/ 200	1/ 100	2/ 250	2/ 200	2/ 100	10/ 250	10/ 200	10/ 100	20/ 250	20/ 200	20/ 100
				Diabase											
6.25	1000		0.311	63	66	73	40	41	46	14‡	14	16	9	9	10
17.	total melting	2.7	0.244	204	211	235	128	133	148	44‡	46	51	28	29	32
24.6		4.1	0.211	308	317	356	193	199	223	60‡	62	69	43	44	49
				Dry Coconino Sandstone											
6.25	600		0.422	36‡	36	39	23	23	25	9	9	9	6	6	6
17.	total melting	3.7	0.307	128‡	130	140	81	83	89	31	31	30	21	21	23
24.6		6.0	0.254	199‡	203	222	127	130	141	52	54	58	32	33	36
				Permafrost											
6.25	400	1.4	0.422	45	47	51	29‡	30	32	10	10	12	7	7	8
17.	total melting	4.9	0.302	158	162	176	108‡	111	121	36	36	40	23	24	26
24.6		7.6	0.265	241	248	271	152‡	157	171	54	56	61	36	37	40
				Carbonate											
6.25	750		0.332	59	61	67	37	38	42	13‡	13	15	8	8	9
17.	total	3.6	0.244	193	200	222	107	110	123	20‡	21	23	27	28	31
24.6	vaporization	5.7	0.211	300	310	344	189	195	217	66‡	68	76	42	44	48
				Ice											
6.25	100	3.8	0.561	39‡	40	42	25	26	28	10	11	11	7	7	8
17.	onset of	15.3	0.415	146‡	149	159	96	97	104	39	40	43	27	28	30
24.6	vaporization	24.0	0.356	221‡	226	242	145	148	159	59	60	65	42	43	46
				Granite											
6.25	750		0.429	57	59	65	36	37	41	12‡	13	14	8	8	9
17.	total melting	3.2	0.314	183	188	208	116	119	132	40‡	41	46	26	26	29
24.6		5.0	0.273	281	289	315	177	182	198	61‡	63	69	39	40	44

*Depth (m)/[yield (kg TNT)]$^{1/3}$ (1 kg TNT = 4.2×10^{16} ergs).
†Pressure at rim/pressure at bottom.
‡Preferred estimates.

are for scaling exponents between 3.4 and 3.6; see *Pohl et al.* [1977, p. 396] for a discussion of scaling laws). The model that we present here is a process description derived from both theoretical considerations and field observations and, as such, is not comparable to more elegant computer models in current use. In combining field observations relevant to late-stage flow and modification processes with the theoretical calculations of early-stage flow we have used observations from the larger terrestrial craters, including Popigai, Manicouagan, Mistastin, West Clearwater, Lake St. Martin, and the Ries. The theoretical parts of the model are given in a series of tables which list initial pressure, shock velocity in the target, fraction of energy transmitted to the target by the shock, penetration depth, and radius of initial energy deposition (Tables 2*a*–2*c*); volume of melt, scaled depth of burst, and excavated volume (Table 3); and radius to selected isobars (Table 4). The field inferences and late-stage flow fields are shown in a series of figures.

The tables list the above parameters for impact velocities of 6.25, 17 and 24.6 km/s; the illustrations are for 24.6 km/s. The velocity 24.6 km/s is the root-mean-square impact velocity of known earth-crossing asteroids [*Shoemaker,* 1977] and is thus of major planetary interest; however, it is so far beyond velocities currently attainable in the laboratory that considerable extrapolation of measured thermodynamic properties is required. We have therefore also carried out calculations for two lower velocities: 6.25 km/s, the velocity used by *Gault and Heitowit* [1963] in laboratory experiments and potentially relevant to low-speed impacts associated with accretional processes, and 17 km/s, a higher velocity derived from meteorite velocity data [*Zook,* 1975] which has been used for other planetary problems and for which only modest extrapolation of equation-of-state data is required.

We have arbitrarily divided the impact process into a series of stages [after *Shoemaker,* 1963]: (1) initial contact, (2) compression, (3) rarefaction and attenuation, (4) excavation and interior flow, (5) fall back and external flow, (6) mechanical modification, and (7) hydrothermal and/or chemical alteration (penecontemporaneous). Stages 1–3 are treated theoretically, and stages 4–7 are largely inferred from field data. Much of this work is based on earlier work as follows: stage 1, *Kieffer* [1977]; stage 2, *Shoemaker* [1963]; stage 3, *Charters and Summers* [1959] and *Gault and Heitowit* [1963]; stage 4, field observations and numerical codes, particularly those of *O'Keefe and Ahrens* [1975]; stage 5, field observations; stage 6, field observations and theoretical studies of *Melosh* [1976, 1977]; and stage 7, field observations. We recognize that there are internal inconsistencies in some of the above models (e.g., the original Charters-Summers model does not conserve momentum) and that consistency of assumptions among the above models for the various stages is rare (e.g., jetting of stage 1 depends on geometry, whereas the compression for stage 2 is calculated from a one-dimensional model, yet all of the flow fields depend on geometric assumptions, etc.), but we have tried to extract the most relevant conclusions from the various workers and to apply them to formulate a scenario for the process. Detailed models which are internally consistent geometrically and thermodynamically for the whole cratering process are still beyond the state of the art [see *Roddy et al.,* 1977].

TABLE 4. Radius to Various Isobars for Impact of 1-km-Diameter Diabase Meteorite and Various Targets

Impact Velocity, km/s	Depth to Isobar, km		Radius to Isobar, km												
	250	200	1000	750	600	400	250	200	100	50	20	10	5	2	1
							Diabase								
6.25	1.60	1.66		0.64	0.67	0.74	0.84	0.90	1.09	1.36	1.80	2.27	2.85	3.87	4.87
17.	2.40	2.48	0.86	0.93	0.99	1.09	1.24	1.32	1.61	1.99	2.65	3.32	4.17	5.66	7.13
24.6	2.72	2.80	0.99	1.07	1.13	1.26	1.43	1.51	1.85	2.29	3.06	3.63	3.84	6.53	8.24
							Dry Coconino Sandstone								
6.25	1.78	1.82				0.67	0.75	0.79	0.93	1.10	1.40	1.70	2.08	2.77	3.46
17.	2.61	2.67	0.85	0.91	0.96	1.05	1.17	1.23	1.45	1.72	2.18	2.65	3.25	4.32	5.41
24.6	2.93	3.00	1.00	1.07	1.13	1.24	1.38	1.45	1.72	2.02	2.57	3.19	3.82	5.09	6.37
							Permafrost								
6.25	1.77	1.82				0.69	0.77	0.81	0.97	1.17	1.51	1.86	2.32	3.12	3.92
17.	2.62	2.69	0.85	0.91	0.96	1.05	1.18	1.24	1.48	1.78	2.31	2.85	3.55	4.98	6.01
24.6	2.97	3.06	0.99	1.05	1.11	1.22	1.37	1.44	1.72	2.06	2.68	3.31	4.12	5.54	6.97
							Carbonate								
6.25	1.65	1.70			0.67	0.74	0.84	0.89	1.08	1.31	1.73	2.17	2.72	3.68	4.64
17.	2.41	2.49	0.88	0.95	1.00	1.11	1.25	1.33	1.61	1.96	2.60	2.25	4.08	5.15	6.93
24.6	2.75	2.84	1.03	1.11	1.16	1.29	1.46	1.55	1.87	2.29	3.03	3.79	4.74	6.42	8.08
							Ice								
6.25	2.16	2.20					0.79	0.83	0.97	1.19	1.43	1.70	2.04	2.66	3.29
17.	3.23	3.29	0.91	0.97	1.02	1.12	1.25	1.31	1.54	1.80	2.25	2.70	3.23	4.21	5.20
24.6	3.62	3.69	0.99	1.06	1.13	1.30	1.45	1.52	1.79	2.10	2.63	3.13	3.77	4.90	6.05
							Granite								
6.25	1.65	1.70			0.65	0.72	0.82	0.87	1.05	1.28	1.71	2.13	2.67	3.62	4.55
17.	2.44	2.51	0.85	0.91	0.97	1.07	1.20	1.27	1.54	1.89	2.51	3.14	3.93	5.33	6.70
24.6	2.78	2.86	0.99	1.06	1.12	1.24	1.40	1.47	1.74	2.19	2.91	3.64	4.57	6.17	7.78

Depth was calculated as penetration depth plus radius to isobar considered from spherical attenuation model. Isobars are given as peak pressure, in kilobars.

The model is presented for the most common meteorite-target lithologic combinations encountered in terrestrial and planetary cratering problems: meteorites of iron, stone (diabase, basalt), frozen stone, and ice and targets of dry crystalline rock (dry in the sense that water is bound and does not cause large-scale vesiculation), carbonate, dry porous (cohesionless or weakly cohesive) rock or regolith, permafrost, and ice. For purposes of discussion we will frequently cite the impact of a diabase meteorite into various targets, and we will refer to this as our 'model meteorite.'

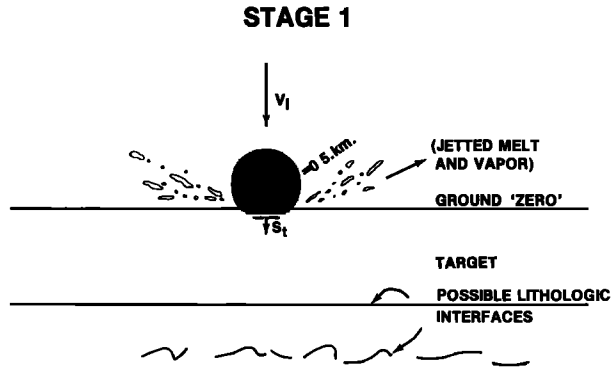

Fig. 4. Schematic diagram of impact conditions during stage 1, initial contact. A mixture of melt and vapor is squirted at very high velocity from the contact interface by jetting. This material could form the tektite-strewn fields. Oblique impact would probably concentrate the jet on the leading side of the projectile and send a stream of melt and vapor down-trajectory. A shock front S_t has started forward into the ground, and shock front S_m has started back into the meteorite. Several lithologic interfaces are shown schematically in the target.

Stage 1: Stage of Initial Contact (Figure 4)

Upon contact of a meteorite with the target, pressures in excess of those obtained by a one-dimensional model are generated if the meteorite is of irregular shape, if the target has an irregular surface, or if the meteorite strikes at an oblique angle, such as the most probable angle of impact of 45° (see, for example, *Kieffer* [1975*b*, Figure 3] or *Kieffer* [1977, Figure 2] for schematics of the geometries). The pressures and temperatures generated are sufficient to vaporize some material and to form a molten 'jet' which is extruded from the meteorite-target interface. This effect was first studied for oblique impacts of metals [*Birkhoff et al.*, 1948; *Walsh et al.*, 1953; *Allen et al.*, 1959; *Al'tshuler et al.*, 1962; *Harlow and Pracht*, 1966] and was observed for hypervelocity impacts into basalt by *Gault et al.* [1963]. A theoretical discussion of the conditions of oblique impact for silicates is given by *Kieffer* [1977], but no experimental data have been published to date. A few percent of the mass of the meteorite and a mass of rock equal to perhaps several meteorite masses are ejected at high velocities from the interface. Although no data are available, we estimate that a few percent of the kinetic energy of the meteorite is transferred into the internal and kinetic energy of the jet.

The material in the jet may be the source of the various tektite-strewn fields suggested to be associated with the impact craters (e.g., the moldavites with the Ries [*Gentner et al.*, 1963] and Javan tektites with Zhamanshin [*Taylor and McLennan*, 1979]). We will return briefly to the question of the origin of the tektites and their relationship to suevite in a discussion of the Ries at the end of the paper.

The duration of the jetting stage is relatively brief. We take

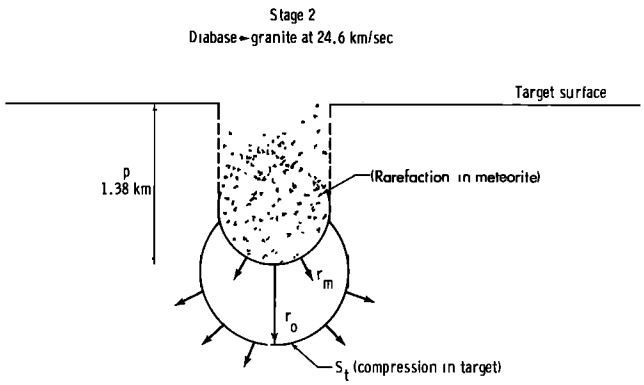

Fig. 5a. Geometry of the shock waves and meteorite at the end of stage 2, substage B, when the rarefaction wave reflected off the top of the meteorite reaches the meteorite-ground interface at the front of the projectile. In the time required for the shock wave to go from the front of the meteorite to the back, be reflected off the back as a rarefaction, and return to the front of the projectile the compressional wave entering the target moves out to radius r_0. In that time the projectile will penetrate depth p.

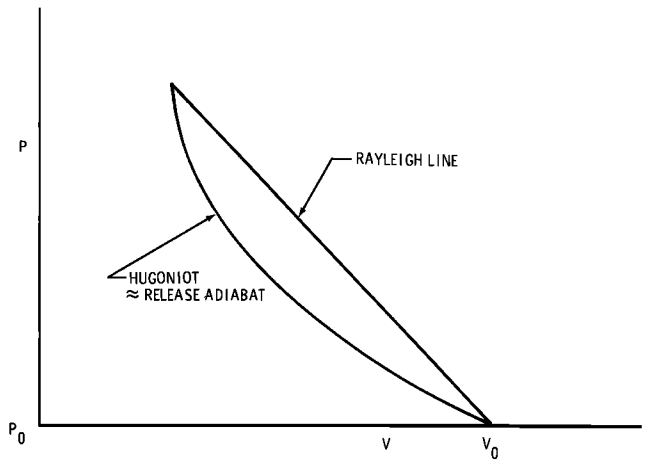

Fig. 5c. Schematic representation of the method used to calculate the pressure-volume work in the attenuation calculations. The waste heat corresponds to the area between the Rayleigh line and the release adiabat. For purposes of calculation the release adiabat is assumed to be equivalent to the Hugoniot.

it as the time during which geometric irregularities in either the meteorite or the target may influence the shock propagation. The duration of this stage is approximately Z/U_s, where Z is the scale of the irregularity and U_s is the shock velocity in the body containing the irregularity. For example, in the model assumed here the meteorite is spherical, and the irregularity might be taken as the sector making initial contact with the target. Z is the characteristic height of this sector, and U_s is the shock velocity of the meteorite. Typically, Z might be 10 m, and U_s about 10 km/s, so that the duration of this stage is about 1 ms. (In the following sections we give only an order of magnitude estimate of stage lengths so that the reader can have an idea of the length of time available for the processes discussed, such as mixing, condensation or chemical alteration; no attempt is made to calculate exact times from the parameters listed in the tables.)

Stage 2: Compression Stage (Figure 5a)

As the target and meteorite are compressed, energy (greater by orders of magnitude than the energy released by large nuclear explosions) is transformed from kinetic energy of the meteorite to kinetic and internal energy of both the target and the meteorite. *Shoemaker* [1963] first described this stage in detail for a one-dimensional impact. *Gault and Heitowit* [1963] generalized Shoemaker's theory to a two-dimensional geometry, extended it to include attenuation in the target, and applied it to laboratory craters formed in basalt by aluminum projectiles impacting at 6.25 km/s. In the description of stages 2 and 3 presented here we apply many of the ideas of these authors; we have used different equations of state in order to make comparisons easily between different rock types.

We take here the compression stage as extending from the moment of contact of the main mass of the meteorite with the target (i.e., when the shock geometry becomes approximately one dimensional) to the moment when the head of the rarefaction wave created by reflection of the shock from the back surface of the meteorite reaches the meteorite-target interface. This stage can be broken into two substages: for the first (substage A) the whole system is under compression, and the duration is approximately

$$t_1 = d/U_{s,m} \tag{1}$$

where d is the length (diameter) of the meteorite and $U_{s,m}$ is the shock velocity in the meteorite; for the second (substage B) the target is still under compression, but the meteorite is decompressing because the rarefaction wave is propagating through the meteorite toward the interface. The duration of this substage is approximately

$$t_2 = d'/c \tag{2}$$

where c is the sound speed in the compressed meteorite and d' represents the length of the compressed meteorite ($d' \sim d(V/V_0)^{1/3}$, where V and V_0 are the specific volumes of the compressed and uncompressed meteorites, respectively). For a Murnaghan equation of state

$$P = \frac{K_0}{n}\left[\left(\frac{V_0}{V}\right)^n - 1\right] \tag{3}$$

where K_0 is the adiabatic bulk modulus at zero pressure and n is the pressure derivative of the bulk modulus, the sound speed at pressure P and volume V or density ρ is

$$c = \left(\frac{K_0}{\rho} + \frac{nP}{\rho}\right)^{1/2} \tag{4}$$

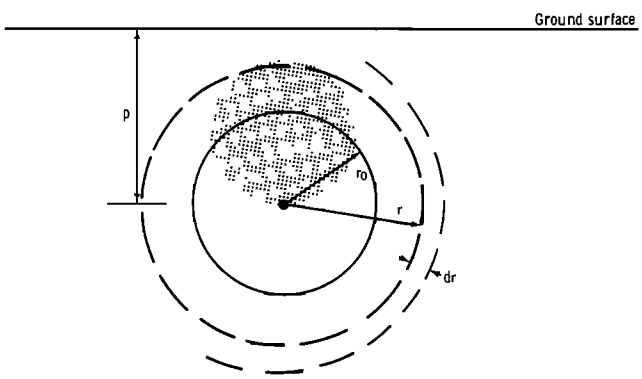

Fig. 5b. Geometry considered in the attenuation calculations of stage 3; r_0 is the radius of the volume assumed uniformly shocked to the peak shock pressure. For most impacts modeled the penetration depth is greater than the meteorite radius, and r_0 defines a sphere centered at depth p.

Therefore the time taken for the rarefaction to travel from the back of the meteorite to the target-meteorite interface is

$$t_2 = d\left(\frac{\rho_0}{\rho}\right)^{1/3}\left(\frac{K_0}{\rho} + \frac{nP}{\rho}\right)^{-1/2} \quad (5a)$$

Because $d' < d$ and $c > U_{s,m}$,

$$t_2 \leq d/U_{s,m} \quad (5b)$$

i.e., $t_2 < t_1$. However, because d' is of the order of d and c is of the order of $U_{s,m}$, we take the duration of stage 2 as $2 \times t_1 = 2d/U_{s,m}$. For our 1-km diabase meteorite traveling at 24.6 km/s an impact into crystalline rock generates a shock wave traveling at ~15 km/s, and so the compression stage lasts 100–200 ms.

Stage 2, Substage A: During t_1, as the Shock Propagates to the Back Surface of the Meteorite

After the irregularities of shock structure associated with stage 1 have decayed, two shock waves propagate away from the meteorite-target interface: one moves forward into the target, and one moves backward into the central section of the meteorite. These two shocks are denoted as S_t and S_m, respectively, in Figure 4. To a first approximation the shock configuration in the center part of the collision region can be taken as being one dimensional [e.g., *Gault and Heitowit,* 1963; *Bjork et al.,* 1967]. The shock states in both the meteorite and the target are specified by the Rankine-Hugoniot jump conditions across the shock fronts:

Conservation of Momentum

$$P - P_0 = \rho U_s u_p \quad (6)$$

Conservation of mass

$$\rho_0 U_s = \rho(U_s - u_p) \quad (7)$$

Conservation of energy

$$E - E_0 = (P - P_0)(V_0 - V)/2 \quad (8)$$

In these equations, P is the pressure, ρ is the density, U_s is the shock velocity, u_p is the particle velocity, E is the internal energy, V is the volume, the subscript zero indicates the parameter in the original, uncompressed state, and the variables without the subscript zero are the parameters in the shocked state. These conservation equations must be supplemented by an equation of state, such as a pressure-volume relation, a shock velocity–particle velocity relation, or a pressure–particle velocity relation. The equations of state used in this paper are discussed in Appendix A and Appendix B.

Consider now a vertical impact such as that shown in Figure 4. The incident velocity of the meteorite is given by v_i; the particle velocities in the meteorite and target will be denoted by u_p when the velocity is meant in a general sense and by u_m and u_t for the meteorite and target, respectively, when one of the bodies is being referred to in particular. The initial conditions generated by the impact are determined by the requirement that the pressure and particle velocity be the same in the shocked regions of the two bodies. The pressure and particle velocity can be obtained graphically from the intersection of the pressure–particle velocity Hugoniot of the target material centered at zero velocity and zero pressure with the reflected ('decelerating') Hugoniot of the meteorite centered at the impact velocity and zero pressure. If a linear shock velocity–particle velocity Hugoniot of the form

$$U_s = c_0 + su_p \quad (9)$$

is assumed for both the meteorite and the target (see Appendix B), these quantities can also be obtained by solving for the particle velocity from the following quadratic equation [*Gault and Heitowit,* 1963]:

$$\rho_{0m}[c_{0m} + s_m(v_i - u_t)](v_i - u_t) = \rho_{0t}\,(c_{0_t} + s_t u_t)u_t \quad (10)$$

In (9), c_0 and s are the coefficients of the Hugoniot, and in (10) the subscripts m and t refer to the meteorite and target, respectively. The equation is derived by requiring $u_m = v_i - u_t$. The value of particle velocity thus obtained can be substituted into (6) to obtain the initial pressure; values obtained for the various meteorite-target combinations and impact velocities are given in Table 2 and Figure 6. The pressures lie in the following ranges: for the 6.25-km/s impact, 1200–175 kbar; for the 17-km/s impact; 6000–1125 kbar; and for the 24.6-km/s impact, 11,500–2300 kbar. The highest pressures are for iron meteorites striking diabase; the lowest pressures are for ice meteorites striking ice targets. The extent into the range of pressures for which material properties are little known is demonstrated by the fact that the pressures attained are as much as 100–350 times the bulk moduli, whereas equation-of-state data generally extend only to 5–10 times the bulk moduli.

We now try to estimate the amount of rock shocked to the initial pressure P during substages A and B by considering the partitioning of energy between the meteorite and the target. A fraction f_j of the initial kinetic energy of the meteorite resides in the jetted material and is lost from the meteorite-target system considered at this stage. At the end of substage A, when the shock front hits the back side of the meteorite, the remaining meteorite and an adjacent plug of target rock are both compressed to the initial pressure P. At this time the initial kinetic energy resides in the jet and in both the meteorite (as kinetic and internal energy) and a plug of target rock adjacent to the interface (also as both kinetic and internal energy). The amount of the initial kinetic energy which has been transmitted to the target by the end of substage A varies with the compositions of the meteorite and target. The total energy per unit mass retained by the meteorite is

$$[(v_i - u_t)^2/2 + u_t^2/2] \quad (11)$$

and, with the original kinetic energy of

$$v_i^2/2 \quad (12)$$

the fraction of the total energy retained by the meteorite is

$$f_m = \frac{(v_i - u_t)^2 + u_t^2}{v_i^2} - f_j \quad (13)$$

Therefore the fraction transferred to the target during substage A is

$$f_t = 1 - f_m = 1 - (1 - u_t/v_i)^2 - u_t/v_i^2 - f_j \quad (14)$$

For simplicity of presentation we assumed that $f_j = 0$, and the values of f_t for such impacts are given in Table 2. The reader can apply a small correction if desired. Note that f_t depends slightly, but not strongly, on v_i. This is because the ratio u_t/v_i in the (14) is relatively independent of v_i (for identical target and meteorite it is 1/2, independent of v_i). For the 24.6-km/s impact the fraction of meteorite kinetic energy transmitted to the target, f_t, ranges from 50% for identical target and projectile to 35% for the most different shock materials, iron into ice.

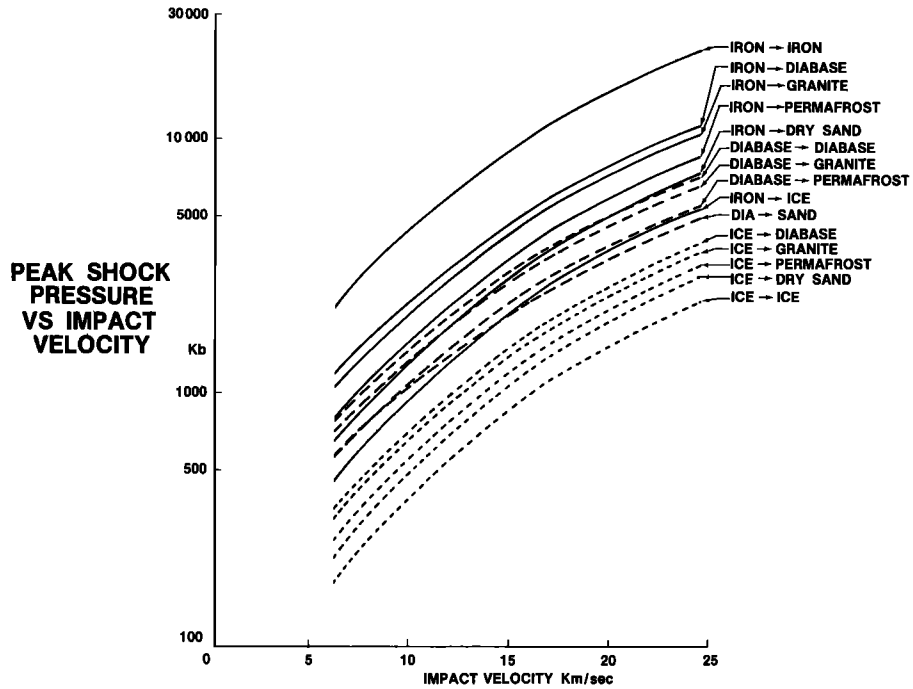

Fig. 6. Peak shock pressure (plotted on logarithmic scale) for impacts of iron, stony (diabase), and ice meteorites into targets of iron, diabase, granite, permafrost, dry sand, and ice.

During the compression stage the shock wave in the target is propagating away from the meteorite-target interface, approximately parallel to it under the center of the impact, but diverging at the edges [e.g., *Bjork*, 1961; *Bjork et al.*, 1967; *Ahrens and O'Keefe*, 1977]. The shock travels with velocity $U_{s,t}$ and covers a distance $U_{s,t} * t_1$ during substage A; energy is transferred from the meteorite into this region traversed by the shock. The energy is deposited equally into kinetic energy E_K and internal energy E [*Shoemaker*, 1963] and is given by

$$E = E_K = P\Delta V/2 = u_t^2/2 \tag{15}$$

Because we are not concerned here with details of the geometry in the vicinity of the shock and because we will assume a spherical attenuation model in stage 3, we calculate here the radius of a sphere of target rock which would contain the energy transferred during the various substages, recognizing that this is a geometry assumed for simplicity rather than accuracy. It aids in both formulation of the attenuation model and comparison with explosion experiments centered at different depths. If the initial density of the target rock into which the energy is deposited is denoted as ρ_{0t} and its initial radius as r_{0t}, its mass would be $4\pi r_{0t}^3\rho_{0t}/3$. With the radius of the meteorite denoted as r_{0m} and its density as ρ_{0m} its mass is given by $4\pi r_{0m}^3\rho_{0m}/3$. Therefore by equating the energy transferred from the meteorite to the sum of the kinetic and internal energies deposited in the target we have

$$f_t(v_t^2/2)4\pi r_{0m}^3\rho_{0m}/3 = u_t^2 4\pi r_{0t}^3\rho_{0t}/3 \tag{16}$$

Solving this for r_{0t} gives a relation between the radius of the meteorite and the radius of the target which contains the transferred energy at an average pressure P:

$$\frac{r_{0t}^3}{r_{0m}^3} = \frac{f_t}{2}\left(\frac{v_t}{u_t}\right)^2\left(\frac{\rho_{0m}}{\rho_{0t}}\right) \tag{17}$$

The dimensions thus obtained are in fact similar to the dimension obtained merely by considering the linear distance that the shock travels during substage A, that is,

$$\frac{r_{0t}}{r_{0m}} \sim \frac{U_{s,t}}{U_{s,m}} \sim \frac{c_{0t} + s_t u_t}{c_{0m} + s_m(v_t - u_t)}$$

For the case of identical projectile and target composition, $\rho_{0m} = \rho_{0t}$, and $v_t = 2u_t$, so that

$$r_{0t}/r_{0m} = 1 \tag{18}$$

The values of r_{0t}/r_{0m} thus obtained are given in Table 2. They are of the order of or less than 1; therefore we repeat that while r_{0t} represents roughly the volume into which energy is placed during substage A, the spherical geometry assumed in the immediate vicinity of the meteorite is not meaningful.

One important result evident from the tables is that r_{0t} is not a very strong function of the impact velocity v_t; this is because it depends on the ratio v_t/u_t, which is relatively independent of the magnitude of v_t.

Stage 2, Substage B: During t_2, as the Rarefaction Propagates Back Through the Meteorite

Transfer of energy from the meteorite into the ground continues approximately until the rarefaction reaches the meteorite-ground interface. Assume that the initial energy density is maintained in the target as the meteorite energy is transferred to the rock, and denote by f_f (for 'final fraction') the amount of the original kinetic energy transferred. Then the radius of rock containing the transferred energy, r_0, is

$$r_0 = r_{0t}(f_t/f_f)^{1/3} \tag{19}$$

We assume that this energy is transmitted into a sphere of ground surrounding the buried meteorite-target interface. Be-

cause r_0, the radius of this sphere, is proportional to the cube root of the fraction of energy transferred, the error in the estimate of r_0 will be proportional to the cube root of the error in the estimate of the fraction transferred. Therefore in the tables we give values of r_0 under the assumption that all of the meteorite energy is transferred, $f_t = 1$, and

$$r_0 = r_{0t}(f_t)^{-1/3} \tag{20}$$

because even if the fraction of energy transmitted to the rock were as low at 0.70, r_0 is within 90% of the value obtained under the assumption that all of the energy is transferred. For example, *Shoemaker* [1963] calculated that for an iron meteorite striking a dry sedimentary target, about 12% of the original energy will be retained by the meteorite at the end of substage B. Allowance for this 12% plus a few percent lost from the jetting process changes the scale of the drawings and conclusions by less than 10%; again, the reader can scale the values in Table 2 by a factor if desired.

The radius r_0 calculated here, then, is taken as the radius of ground initially shocked to pressure P and provides the initial condition for the attenuation model developed in the next section.

During the compression stage 2 the meteorite-ground interface penetrates a distance p into the ground, given approximately by

$$p = \left(\frac{d}{U_{s,m}}\right)u_t + \left(\frac{d'}{c_m}\right)u_t \tag{21}$$

(c_m is the sound speed in the meteorite given by (9)).

The first term on the right-hand side is the distance that the interface travels during substage A; the second term is the distance that the interface travels during substage B. As was discussed previously at (5), to the accuracy of this model it is sufficient to approximate this penetration depth as

$$p \sim 2\left(\frac{d}{U_{s,m}}\right)u_t \sim 2\left(\frac{2r_{0m}}{U_{s,m}}\right)u_t \tag{22}$$

These penetration depths normalized to the initial meteorite radius are given in Table 2, and in Figure 7 for our 1-km meteorite.

The reader should note from the tables that under certain conditions of velocity and for certain combinations of meteorite and ground materials the penetration distance p is less than the radius r_0 of the sphere within which the initial energy is assumed to be deposited. This is true for almost all projectiles striking an iron target at low velocities, but the only geologically interesting situations for which this occurs are the cases of ice or permafrost meteorites striking the harder target rocks. Physically, the interface penetration is so shallow (i.e., particle velocities are very low) that energy is deposited near the ground surface rather than in a deep region below a rapidly penetrating interface. We suggest that for these cases a model of energy deposition into a surface hemisphere (in the manner of *Charters and Summers* [1959] and *Gault and Heitowit* [1963]) is a relatively good approximation. Mathematically, the criterion for such a 'surface hemispherical burst' model is

$$p < r_0 \tag{23}$$

or

$$\frac{1}{5}\left[\frac{c_m}{u_t} + s_m\left(\frac{v_i}{u_t} - 1\right)\right] * \left\{\left(\frac{v_i}{u_t}\right)^{2/3}\left(\frac{\rho_{0m}}{\rho_{0t}}\right)^{1/3}\right\} > 1 \tag{24}$$

This inequality (and the results shown in the tables) brings out the important fact that the criterion for whether a meteorite impact should be considered a 'surface burst' or a 'deep burst' depends not only on the materials involved (through ρ_{0m}/ρ_{0t} and through the ratio v_i/u_t, which we have shown in Table 2

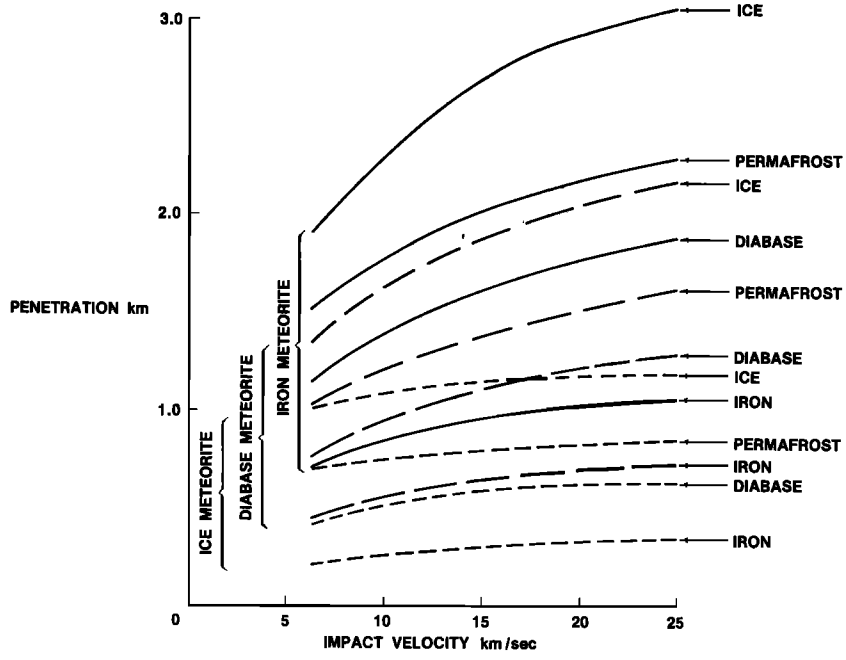

Fig. 7. Penetration of 1-km-diameter meteorites. Shallow penetration (less than the radius of the projectile) occurs only for impacts of ice into iron and for the slower impacts of ice into diabase and the geologically unlikely event of a diabase meteorite hitting an iron target.

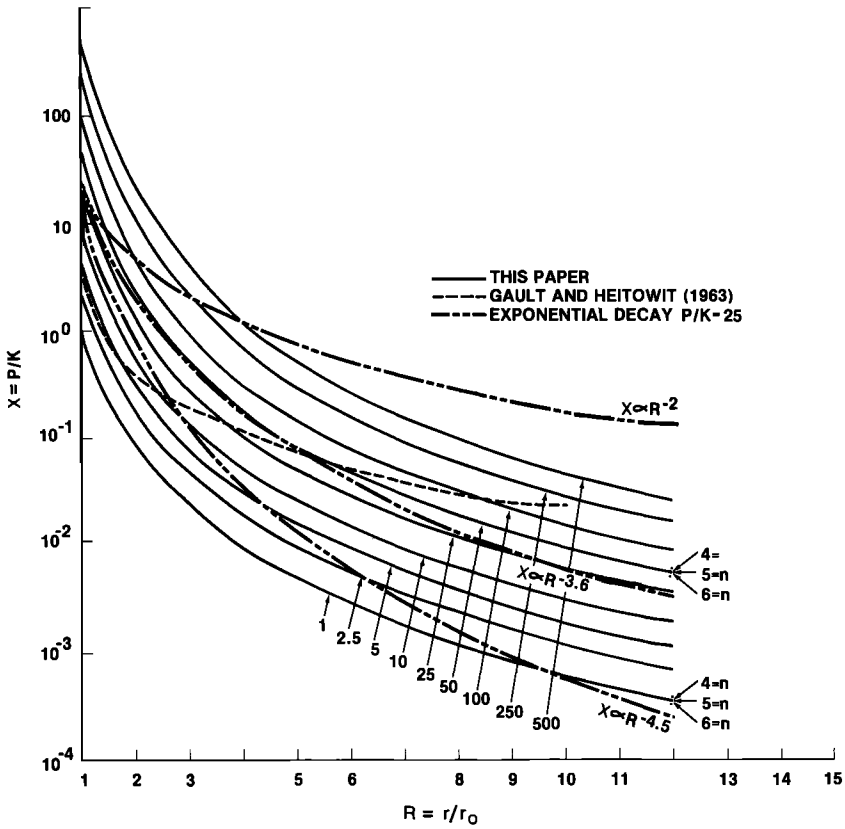

Fig. 8. Normalized pressure ($X = P/K_0$) versus normalized radius ($R = r/r_0$). Attenuation curves are shown for initial pressure ratios ranging from 1 to 500. The curves are for $n = 5$, with ranges for $n = 4$ and $n = 6$ shown at the right. The dashed curve is approximately the result of *Gault and Heitowit* [1963]. The dash-dotted curves are fitted to the form $X \propto R^a$ for three proposed values of a: -2 as suggested by *Cooper* [1973]; -3.6, the intermediate value preferred by *Dence et al.* [1977] and the nearest to fitting our model; and -4.5, a very steep attenuation also compatible with observations of terrestrial craters [*Dence et al.*, 1977].

to be relatively independent of v_i but which does depend strongly on the lithologies) but also on the impact velocity (through the term c_m/u_t in the above equation, but since u_t is proportional to v_i, the dependence is really through v_i in this term). Thus although the common assumption is that icy bodies (comets) will give surface bursts, we see that at the root-mean-square approach velocity of 24.6 km/s the penetration depth for icy bodies, though shallow by comparison with that of iron meteorites, is sufficiently great to allow a subsurface burst model to be used.

Table 3 shows scaled depths of burst p (derived from the expression $p/[E_K]^{1/3}$, where E_K is the meteorite kinetic energy) for our standard impacts of a diabase meteorite. The values range from about 0.21 to 0.56 m (kg TNT)$^{1/3}$ and are somewhat deeper than the value of 0.10 (converted to metric units) used by *Oberbeck* [1977] to yield the best morphologic similarity of impact and explosion craters. The value of p obtained is also deeper by about 60% than depths calculated by *Trulio* [1977] using a considerably different model.

Stage 3: Rarefaction and Attenuation (Figures 5b and 8)

The rarefaction and attenuation stage is taken from the end of stage 2 until the shock has decayed below a few kilobars (the stress at the crater rim). The duration of this stage is approximately r/c_t, where r is the final crater radius and c_t is the velocity of sound in the compressed target. For our 1-km meteorite this phase lasts approximately 1 s.

A modified Charters-Summers, Gault-Heitowit model is proposed for calculation of attenuation of the shock wave with distance from the center of the impact. The model is shown schematically in Figure 5*b*. Spherical divergence of the shock wave is assumed for deep-centered impacts, and hemispherical divergence for shallow-centered impacts. Because of the spherical symmetry assumed in this model the same attenuation model applies to either spherical or hemispherical expansion.

Assume that the energy which has been delivered to the target during stage 2 of the impact is distributed at all times uniformly in a compressed sphere behind the shock wave, S (this is the basic assumption introduced by *Charters and Summers* [1959] and used by *Gault and Heitowit* [1963]). Then the total energy in the system, E_T, is the sum of the (equal) kinetic and internal energies:

$$E_T = \frac{4}{3}\pi\rho_0 r^3 P(V_0 - V) = \frac{4}{3}\pi r^3 P\left(1 - \frac{V}{V_0}\right) \qquad (25)$$

where $V_0 = 1/\rho_0$. Here all properties refer to target properties, so the subscript t, as in ρ_{0t}, is dropped.

For a Murnaghan equation of state

$$P = \frac{K_0}{n}\left[\left(\frac{V_0}{V}\right)^n - 1\right] \qquad (26a)$$

or

$$\frac{V}{V_0} = \left(\frac{Pn}{K_0} + 1\right)^{-1/n} \qquad (26b)$$

the total energy becomes

$$E_T = \frac{4}{3}\pi r^3 P\left[1-\left(\frac{Pn}{K_0}+1\right)^{-1/n}\right] \tag{27}$$

As this energy spreads over a larger volume as the shock diverges, the differential energy dE_T for a small radius change dr is

$$\frac{dE_T}{dr} = 4\pi r^2\left[1-\left(\frac{Pn}{K_0}+1\right)^{-1/n}\right]\left[P+\frac{r}{3}\frac{dP}{dr}\right] + \frac{4}{3}\pi r^3\frac{P}{K_0}*\left[\left(\frac{Pn}{K_0}+1\right)^{-1-(1/n)}\right]\frac{dP}{dr} \tag{28}$$

The internal energy added to a mass of material is given by the area under the Rayleigh line (the straight line connecting the initial state at (P_0, V_0) with the final state at (P, V) (see Figure 5c)). The internal energy regained during isentropic expansion is given by the area under the release adiabat. As is discussed in Appendix B, we now assume that the Hugoniot is an adequate approximation to the release adiabat. The specific waste heat ΔE_w is the area between the Rayleigh line and the release adiabat:

$$\Delta E_w = \frac{1}{2}P(V_0 - V) - \int_{V_0}^{V} P\,dV \tag{29}$$

Now

$$\int_{V_0}^{V} P\,dV = \frac{K_0}{n}\frac{1}{(1-n)}\left[V_0\left\{1-\left(\frac{Pn}{K_0}+1\right)^{1-(1/n)}\right\} + V_0(1-n)\left(\frac{Pn}{K_0}+1\right)^{-1/n} - (1-n)V_0\right] \tag{30}$$

Therefore

$$\Delta E_w = \frac{1}{2}\left[PV_0 - \frac{2K_0V_0}{n}\right]\left[1-\left(\frac{Pn}{K_0}+1\right)^{-1/n}\right] + \frac{K_0V_0}{n(1-n)}\left[1-\left(\frac{Pn}{K_0}+1\right)^{1-(1/n)}\right] \tag{31}$$

Therefore the waste heat deposited in a shell of thickness dr is

$$\frac{dE_w}{dr} = 4\pi\rho_0 r^2\left\{\frac{1}{2}\left[PV_0 - \frac{2K_0}{n}V_0\right]\left[1-\left(\frac{Pn}{K_0}+1\right)^{-1/n}\right] + \frac{K_0V_0}{n(1-n)}\left[1-\left(\frac{Pn}{K_0}+1\right)^{1-(1/n)}\right]\right\} \tag{32}$$

Equating (28) and (32),

$$4\pi r^2\left[1-\left(\frac{Pn}{K_0}+1\right)^{-1/n}\right]\left[P+\frac{r}{3}\frac{dP}{dr}\right] + \frac{4}{3}\pi r^3\frac{P}{K_0}\left[\left(\frac{Pn}{K_0}+1\right)^{-1-(1/n)}\right]*\frac{dP}{dr} = -4\pi r^2\left\{\frac{1}{2}\left[P-\frac{2K_0}{n}\right]\left[1-\left(\frac{Pn}{K_0}+1\right)^{-1/n}\right] + \frac{K_0}{n(1-n)}\left[1-\left(\frac{Pn}{K_0}+1\right)^{1-(1/n)}\right]\right. \tag{33}$$

It is convenient to normalize the pressure to $P/K_0 = X$ and the radius $r/r_0 = R$. Then, from the above equations, dX/dR is

$$\frac{dX}{dR} = \left\{-\frac{3}{2}X + \frac{3}{2}X(Xn+1)^{-1/n} + \frac{1}{n} - \frac{1}{n}(Xn+1)^{-1/n} + \frac{1}{n(1-n)}[(nX+1)^{1-(1/n)} - 1]\right\} \cdot \left\{\frac{R}{3}[1-(nX+1)^{-1/n} + X(nX+1)^{-1-(1/n)}]\right\}^{-1} \tag{34}$$

If an initial value of X, denoted by X_0, is specified at any initial value of R, denoted by R_0, this equation can be numerically integrated to give the shock attenuation (Figure 8). Note that the bulk modulus appears only in the nondimensional pressure X, so that different values of X_0 can correspond either to high initial pressures due to high impact velocities or to low bulk moduli for soft targets. The effects on the attenuation rate of altering the parameters $X = P/K_0$ and n are shown in Figure 8. Variation of n over the range 4–6, which spans the parameter for most materials, has negligible effect. Therefore in terms of the nondimensional pressure and nondimensional radius the attenuation curves for high-velocity impacts producing a given value of X in a soft target and a low-velocity impact producing the same value of X in a hard target are nearly identical; however, the value of r_0 (defining the volume in which the initial energy is placed) is different in the two cases.

A near-field approximation can be obtained for $X \gg 1$, noting that for n = 4–6(5), nX is also greater than 1:

$$\frac{dX}{dR} \sim +\frac{3X}{R}\left(\frac{n}{1-n}\right) \tag{35}$$

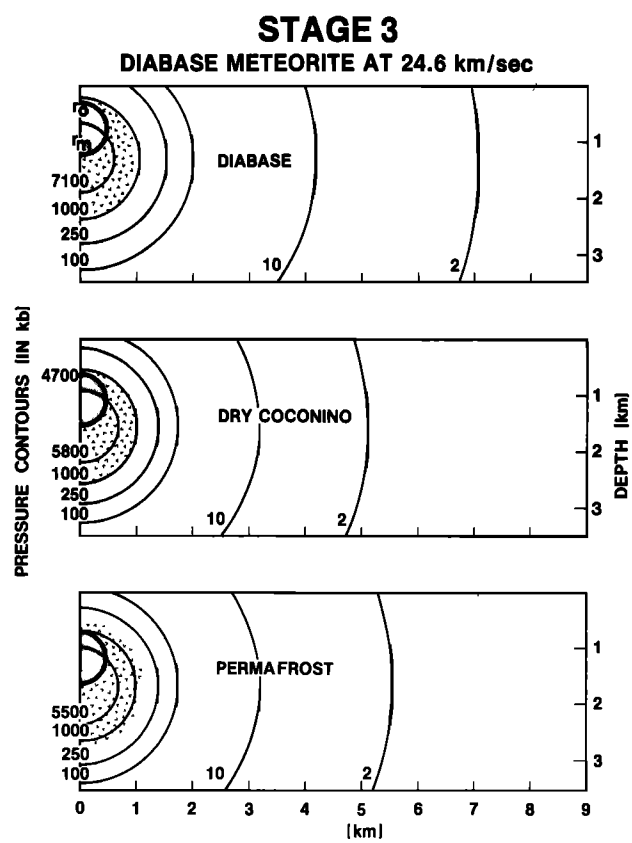

Fig. 9. Geometries of calculated peak shock pressures for impacts into three targets. Note the relative penetration depths, initial peak pressures, relative positions of the 2-kbar isobars, and the nearly equal sizes of the melt zones (indicated by the patterned zones).

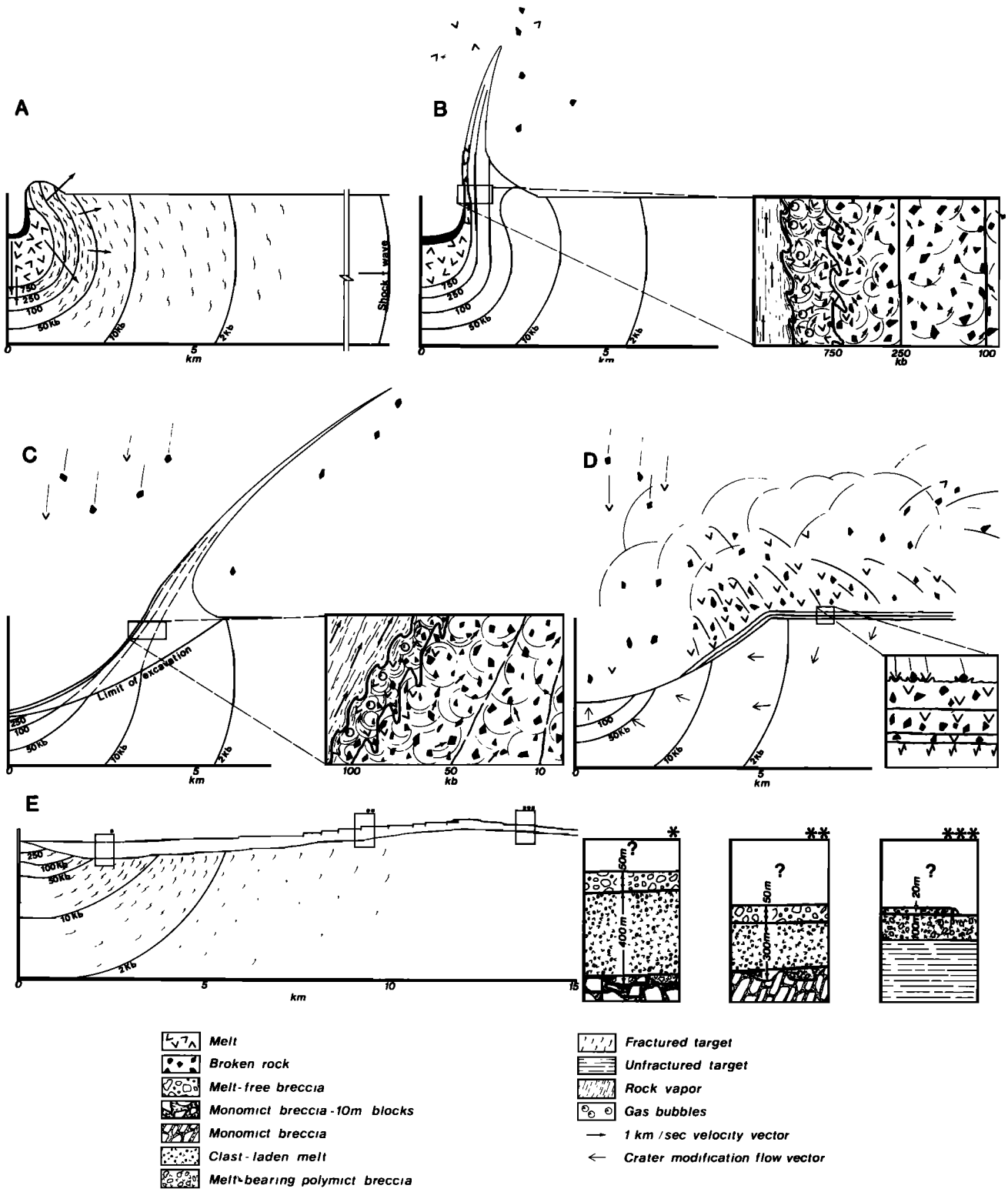

Fig. 10

Figs. 10, 11. Cross sections of model impacts into a hard rock and volatile-rich target. These figures are a composite of inferences from field observations and the calculations discussed in the text. The shape of the contours is estimated from various detailed computer models mentioned in the text, but their radial position is based on the one-dimensional calculations described. Stage 4 (excavation and ejection is shown in Figures 10*a*–10*c* and 11*a*–11*c*; stage 5 (ejection and external flow) is shown in Figures 10*b*–10*d* and 11*b*–11*d*; stage 6 (modification) is shown in Figures 10*d* and 11*d*; and the final configuration of the craters prior to erosion is shown in Figures 10*e* and 11*e*. (*a*) Note the extensive fracturing of the rock which probably occurs as the shock propagates. Note also that permafrost is accelerated to higher velocities than granite. (*b*) As ejection proceeds, the higher velocities and lower viscosities of the more intensely shocked debris result in separate flows of gas, melt, and fractured debris. These units become extensively mixed on a scale of millimeters by intrusion of the gas and melt into less shocked materials and by turbulence in the flows. The large volume of steam greatly enlarges the screen of ejected debris from the permafrost impact. (*c*) As flow proceeds, it becomes bounded by a parabolic cavity which is assumed to be defined by a 2-kbar isobar at the margin and the 250-kbar isobar at the base. Slightly deeper excavation

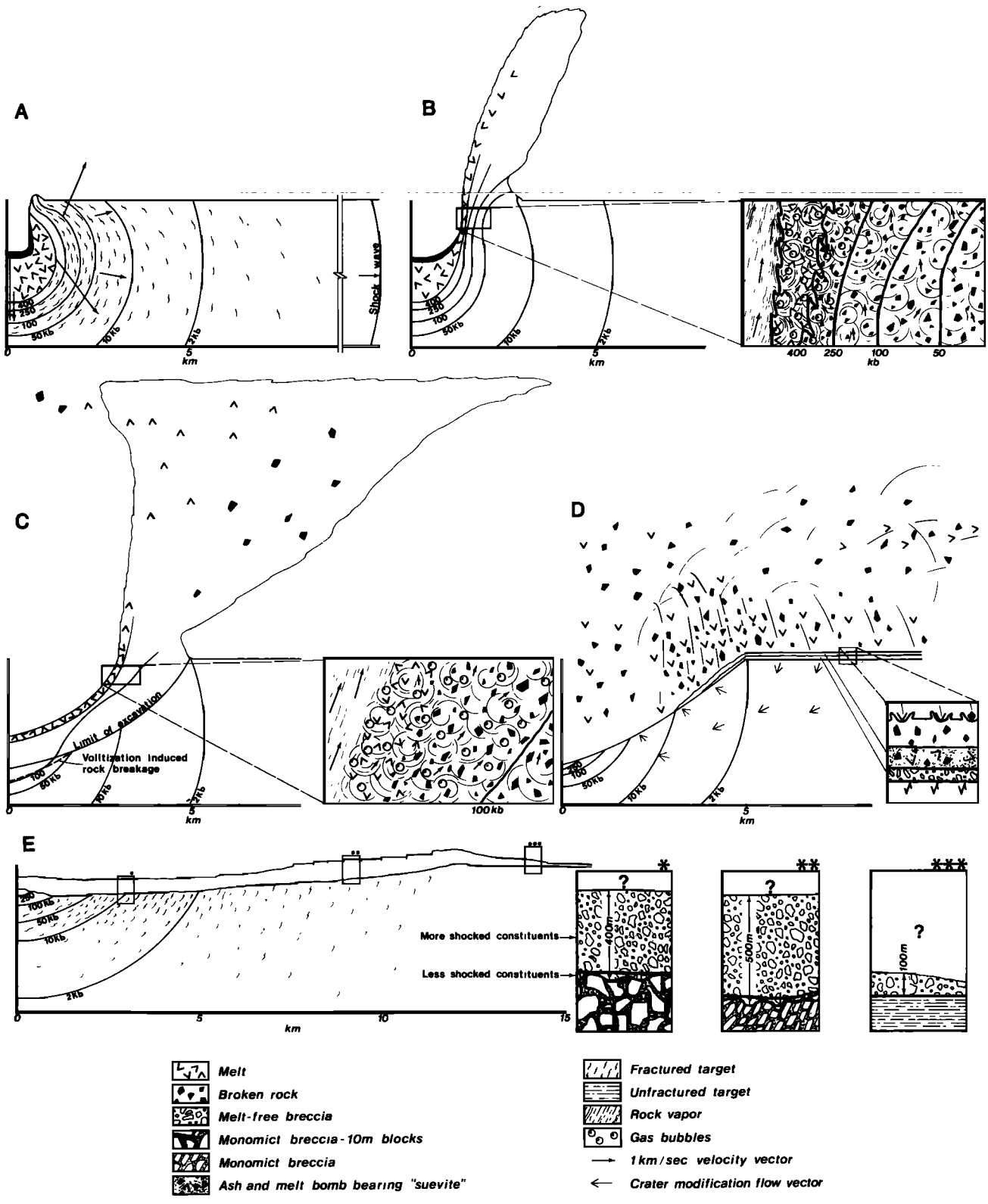

Fig. 11

would probably take place in the volatile-rich target owing to steam formation below the 200-kbar isobar. The granite crater probably would be excavated to a high-pressure surface less deep than the permafrost target owing to the higher strength of the granite and the higher postshock velocities of the permafrost; thus the 2-kbar isobar is arbitrary. Mixing of gas with melt and melt with less shocked debris is probably very effective by this point in the cratering process, much of the melt may begin to cool and resorb fragmented rock, and the silicate vapor will begin to condense on the melt and fragmented rock with which it is mixed. (*d*) Toward the end of the process the moving ejecta consists of the materials on ballistic trajectories. This material will strike and excavate ejecta on a small scale, further mixing constituents derived initially from a range of shock pressures. (*e*) A composite of the final stratigraphy of the craters. Because erosion has removed the uppermost deposits in all terrestrial craters, the top of the ejecta and fallback is not well characterized petrologically. The reader may compare the generalized sketches here with the more detailed model of *Stöffler* [1977, p. 453] to visualize the resulting stratigraphy for the Ries.

For example, at $R = 1$, for $X = 4$ and $n = 5$, $dX/dR = -15$.)

A far-field approximation can be obtained for $X \ll 1$:

$$\frac{dX}{dR} \sim -\frac{3X}{R} \tag{36}$$

(For example, at $R = 5$, for $X = 0.016$, $dX/dR = -0.0096$.)

Integration of (35) shows that in the near-field region the normalized pressure decays as

$$X \propto R^{+3n/(1-n)} \tag{37}$$

For the most common value of $n = 5$ the pressure decays as $R^{-3.75}$ in the near field, and the dependence will be between $R^{-3.65}$ and R^{-4} for materials with normal bulk modulus behavior. The dependence changes to

$$X \propto R^{-3} \tag{38}$$

in the far field and is, to first order, independent of n.

It should be emphasized that at some point the spherical (or hemispherical) symmetry assumed fails to represent realistically the near-surface conditions because the effect of rarefactions from the free surface is not accounted for. Therefore our model cannot predict the differing rates of attenuation along the axis of symmetry and the free surface obtained in two-dimensional models, such as those of *Orphal* [1977]. Our calculated attenuation rates should most closely match those obtained along the axis of symmetry or, generally, away from the free surface, although at high pressures for deeply buried meteorites (say, about 500 kbar in the examples shown in Figure 9) the influence of the free surface on the shapes of the isobars may be small.

In comparing these calculated attenuation rates with field and laboratory work and with other theoretical models we note that there are large variations in published values. Data cited by *Cooper* [1973] and *Ahrens and O'Keefe* [1977] on the rate of attenuation around contained and surface nuclear explosions suggests that $P \propto R^{-2}$. Field observations at impact craters give a wide range of attenuation rates. *Robertson and Grieve* [1977] in discussing the attenuation based on observations of deformation features, particularly in quartz at Charlevoix and Slate Islands, argue for $P \propto R^{-5}$–$R^{-5.5}$. Data for samples at the base of Brent call for an uncorrected $P \propto R^{-20}$ curve. Attenuation rates are inferred from field observations of samples around large craters by restoring the samples to their position at the time of passage of the shock wave, and because the bottoms of large craters have all been displaced owing to extensive collapse or other modifications late in the cratering process, the derived attenuation rates depend critically on the model used to restore the crater geometry. For example, *Dence et al.* [1977], using the same data as *Robertson and Grieve* [1977], concluded that rates of R^{-3}–$R^{-4.5}$ are most reasonable by using a slightly different restoration model; rates as low as R^{-2} can be derived for Brent [*Robertson and Grieve*, 1977]. *Stöffler* [1977, p. 454] believes that the near-field attenuation [for $P > 100$ kbar] was at least as rapid as $R^{-2.7}$.

Attenuation rates derived from theoretical models span nearly as broad a range as the field estimates, although the absolute values tend to be lower. Purely geometrical attenuation of an elastic (for example, acoustic) wave without absorption results in $P \propto R^{-1}$. If the energy is evenly deposited throughout a sphere which continuously expands, the attenuation would be $P \propto R^{3/2}$. The *Gault and Heitowit* [1963] model for low-speed impact (6.25 km/s) of aluminum into basalt yielded the values shown in Figure 6. This model, derived, as is ours, by using a Charters-Summers approach, matches ours for $R/R_0 = 1$–2 but falls off to about R^{-2} in the far field. For a very high velocity impact, *Ahrens and O'Keefe* [1977] calculate very low rates ($P \propto R^{-0.2}$) of attenuation in the near field and rates increasing to about R^{-2} farther out. We note in passing that field and theoretical models give attenuation rates spanning 2 orders of magnitude in the exponent of the radius.

Table 4 lists the distances from the center of the crater to selected peak pressure isobars for the impact of our standard 1-km diabase meteorite on the various targets. Table 3 lists estimates of the volume of rock melted or vaporized for the same impacts and estimates of the total size of the crater produced. The melt and vaporized volumes are minimum estimates, as they are based on peak pressure isobars that are at the upper end of proposed melting ranges for each target material. The melting of diabase was taken to occur at 1000 kbar, the value for total melting of Lonar Crater, India, Deccan Trap basalt [*Kieffer et al.*, 1976*b*]. We take 750 kbar as the limit of total melting for granite (*Stöffler* [1972] suggests 600 kbar for incipient melting). Melting of dry porous quartzite or quartz sand was estimated to be at about 600 kbar and is estimated for permafrost at about 400 kbar. A range of peak isobars for the bottom and sides of craters is given in Table 3, with preferred values (marked with double daggers) selected according to the criteria discussed in Appendix C. The volumes excavated were calculated from the volume of a paraboloid [after *Dence*, 1973] formed by rotating a function of the form $Y = aH^2 + b$ about a vertical axis, where Y is the distance from the center line to a point on the outside of the excavation, H is the depth, and a and b are constants. The volume of the craters is $1.67r_m^2H_m$, where H_m is the depth and r_m is the radius. We give volume estimates for a range of plausible bottom and rim pressures (see Appendix C). We note that an uncertainty of 150 kbar [*Dence et al.*, 1977; *Grieve et al.*, 1977; *Simonds et al.*, 1978*b*] in bottom limiting peak pressure (100–250 kbar) has a small effect on the excavated volume. However, variation in limiting rim pressure from a value of 2 kbar to the 20-kbar level preferred by *Dence et al.* [1977] greatly reduces the volume excavated, because the volume varies as R^2 and the difference in distance between the 2- and 20-kbar isobars is large. For crystalline rocks the percentage melt calculated for a crater based on a 250-kbar bottom isobar and a 2- or 1-kbar rim isobar approximately matches the percentage melts calculated by *Grieve et al.* [1977] from studies of large craters in crystalline rocks. Use of the 10- or 20-kbar isobar for the rim diameter results in calculated melt fractions being much higher than field estimates, suggesting that even a 10-kbar peak pressure for the rim of hard-rock craters may be too high. The relative positions of various key isobars are shown in Figure 9 for the standard impact into diabase, dry Coconino sandstone, and permafrost. The comparable sizes of the melt zones in all three cases are easily seen, as well as the rather large differences in position of the low-pressure, crater-bounding isobars.

Examination of Table 3 and Figure 9 provides an answer to the first part of our basic question: Are the differences observed in melt abundance at craters in crystalline and sedimentary rocks due to differences in the melting behavior of the rocks or to the fate of the melt? In terms of volume of melt produced (rather than percentages) the calculations show that the wet and dry sedimentary rocks yield more melt on impact than the crystalline targets; for example, a diabase meteorite striking diabase or granite at 24.6 km/s yields 4–5 km^3 of

melt, whereas in dry Coconino sandstone or permafrost the yield is 6–8 km^3 of melt. We state this conclusion in terms of actual melt volume rather than percentages so that it is independent of model values for crater volume, which are subject to much more uncertainty than the model volumes for melt. Nevertheless, there are no field or theoretical data to suggest that craters in sedimentary rocks are more than 1 order of magnitude larger than their energy-equivalent counterparts in crystalline rocks; thus even in terms of melt fraction the sedimentary targets should have approximately (within 1 order of magnitude) the same fraction of excavated volume melted.

There remains the paradox that impacts into sedimentary rocks should produce as much or more melt than impacts into crystalline rocks, yet there is a virtual absence of melt in the sedimentary target craters or melted sediments at the targets with thick sediments overlying crystalline rocks. We conclude that processes going on after passage of the rarefaction (stages 4–7) must disperse the melted and decarbonated sediments and render them unrecognizable or deposit them as a thin superficial layer which has been eroded from even the freshest terrestrial structures.

Stage 4: Excavation and Flow Within the Crater (Figures 10a–10c and 11a–11c)

As the rarefaction passes through the target during stage 3, it decompresses the shocked material, rotates the direction of particle motion from radially away from the meteorite and into the ground to tangentially outward (parallel to the crater floors and walls), and accelerates the particles into ballistic trajectories (Figures 10 and 11). For very simple substances, such as aluminum, the velocity obtained in the rarefaction (denoted as $u_{r,p}$) is twice the shock particle velocity [*Walsh and Christian,* 1955]:

$$u_{r,p} \simeq 2u_p$$

This approximation can be applied to some dense crystalline rocks and even to dry porous rocks at pressures of a few hundred kilobars [e.g., *Ahrens and Gregson,* 1964], but important departures occur for wet soils [*Anderson et al.,* 1966; *Anderson,* 1967]. In particular, materials containing water undergo large expansions accompanied by high velocities due to vapor expansion when they are shocked to pressures above 100 kbar. For example, dry soil shocked to 300 kbar has a particle velocity of 3 km/s in the shock state and releases with a velocity of approximately 5.7 km/s, whereas wet soil shocked to the same pressure has the same particle velocity in the shock state but releases with a particle velocity of approximately 7.3 km/s [*Anderson et al.,* 1966, Figures 3–10 and 3–11].

The duration of this stage is approximately $d'/2u_p$, where d' is the slope distance rock must travel to leave the crater and $2u_p$ is the approximate particle velocity in the rarefaction. For our standard impact, $d' \sim 7$ km, and $u_p = 10^1$–10^3 m/s, so the stage lasts a few minutes. During this time the major processes which must be considered are (1) movement and internal mixing of rock, melt, and gas and (2) heat transport by radiation, conduction, and mass transport.

By this time the flow fields are no longer well described by the spherically symmetric model, and we have modeled our flow fields (shown in Figures 10*a*–10*c* and 11*a*–11*c*) in part after the numerical models for flow within impact craters [*Bjork,* 1961; *O'Keefe and Ahrens,* 1975, 1976] and shallow buried explosion craters [e.g., *Oberbeck,* 1977; *Orphal,* 1977; *Maxwell,* 1977] and in part on field observations which reveal complexities superimposed on the basic flow pattern predicted by the numerical models. The basic flow pattern is outward movement of a series of concentric shells of progressively less shocked and slower moving rock. Through the rarefaction wave and reflection of the flow field from the rigid bottom of the cavity the motion of most material is upward and outward. Thus the basic flow patterns predicted by computer models would give a series of stratified ejecta shells in which material initially separated by great distances remains relatively separated in the flow.

However, significant deviations from this simple pattern are implied by (1) the observed microscale chemical homogeneity of impact melts from large craters, such as Manicouagan [*Floran et al.,* 1978], West Clearwater [*Simonds et al.,* 1978*b*], Popigai [*Masaitis et al.,* 1975], and the Ries [*von Engelhardt,* 1972], where large-scale lithologic differences present in the target rocks are not apparent in the melt sheet; (2) the admixing of relatively unshocked and cold crystalline debris into the melt sheet; and (3) the presence of mixed debris units containing unshocked and shocked crystalline rocks, melt fragments, and pieces of meteorite [*Shoemaker,* 1963]. All of these observations imply that material initially at different horizontal and vertical distances from the center of the impact is mixed together. Although some of this mixing undoubtedly takes place after the ejection of the material from the crater into different ballistic trajectories, some must also take place during flow within the crater because the material is flowing along the transient cavity boundary, which is not at a specific isobar but cuts across isobars (see Figures 10*c* and 11*c*). *Grieve et al.* [1977] and *Phinney et al.* [1978] argue that the mixing takes place largely at the boundary of the transient cavity and that the Reynolds number is likely to be quite high there.

The mixing of the relatively cold unshocked fragments into the melt rapidly decreases the temperature of the melt and causes local to total quenching. *Simonds* [1975], *Simonds et al.* [1978*a*], and *Onorato et al.* [1976, 1978] estimate that this quenching can occur in less than 100 s. In the case of Manicouagan, at least 40% of the mass of the final melt sheet consists of clasts of (anhydrous) crystalline rocks admixed during the flow. This admixing, with partial digestion of the cold debris, changes the shock-produced melt unit from a relatively homogeneously shock-melted unit to a clast-laden melt sheet and increases the volume of the sheet over the volume of shock-melted rock by the amount of clasts added. The physical effect of the admixing of clasts is to raise the viscosity of the melt by both rapid cooling and mechanical interactions between the clasts and the clasts and melt. However, even with the admixture of 40% by weight clasts the melt sheet at Manicouagan still flowed and formed a sheet with an igneous texture. The chemical effect of admixture of this large number of clasts is also significant. It might be expected that because of admixing, melt composition would not exactly match basement rock composition (depending on the relative sources of the melt and clasts) and that the modes of mineral clasts in the melt or even in glass bombs would be different from those of the crystalline basement modes. D. Stöffler (personal communication, 1979) has called our attention to these effects in the Ries melt and glass bombs [*Stöffler,* 1977, pp. 183, 184; *Pohl et al.,* 1977].

The effects of admixing relatively dry crystalline rocks and wet sediments or carbonates into the melt will be quite different, as can be seen by considering Figure 12. The proportion of inclusions required to cause quenching of the melt depends

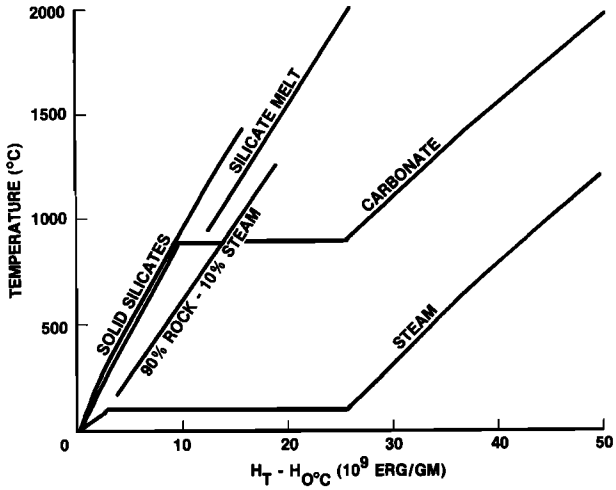

Fig. 12. Enthalpy versus temperature for crystalline rocks. Solid silicates plot along the line shown. Melting adds a significant amount of latent heat shown, but far less than that required for vaporization of water or carbonates.

on the enthalpy of the resulting mixture. (It also depends on the relative sizes of the clasts, but this mainly affects the rate of quenching; we consider here only the limiting case of total heat transfer during mixing.) Consider in Figure 12 the enthalpy-temperature relations for anhydrous silicates, carbonates, pure water, and a hypothetical water-saturated sediment containing 10% water by mass. The following calculations apply to sediments containing unbound water, i.e., pore water. The heat content of typical anhydrous silicates rises smoothly to the melting point; the latent heat of melting is typically about 25% of the heat required to reach the melting point from ambient conditions. Thus if anhydrous rocks are mixed into melt, equilibration of the hot melt with the cold inclusions occurs solely by increasing the temperature of the included fragments. In contrast, water, wet sediments, or carbonates have low-temperature phase changes with large latent heats of vaporization, and equilibration of the cold clasts with the melt sheet will cause vaporization as well as heating. The enthalpy of pure water rises smoothly to 100°C, where there is a large increase of heat content because of the large latent heat of vaporization. Thus the addition of, say, 10% water to a dry rock appreciably increases the heat content of the system at a given temperature (Figure 12). An appreciable fraction of the heat in the system is stored in the volatile phase. Similarly, for carbonates, e.g., calcite, an appreciable fraction of the heat content is stored in the gas phase at temperatures above the decarbonation temperature. Consideration of ice in permafrost would make only a small change in the graphs because the latent heat of fusion is small in comparison to the latent heat of vaporization.

The enthalpies of the water-bearing and carbonate systems are so high that a much smaller proportion of admixed sedimentary rock than of anhydrous crystalline rock is required to quench the melt to subsolidus temperatures. Thus the process of admixing superheated melt with sedimentary rocks will not result in as large an increase of melt sheet volume as the admixing of superheated melt with crystalline rocks. However, because we estimate that the increase of melt volume by admixture of crystalline rocks is about 40%, this process could account for only a difference of about 50% in the comparative volumes of melt sheets from crystalline versus sedimentary craters. This is not nearly sufficient to account for the 1–2 orders of magnitude difference observed in the field. In neither case does this process directly destroy the melt produced by the shock; that is, at stage 4 in the cratering process there are still several cubic kilometers of melt flowing out of the crater of our model impact. However, in the case of a crater in crystalline rock this volume is being augmented by about 50% by crystalline rock inclusions, but in the case of a crater in sedimentary rock this much rock cannot be included before the melt unit is quenched. If more inclusions are picked up, they are admixed into a quenched, relatively solid unit rather than a fluid melt unit. We will propose below that during stage 5 the admixing of melt with sediments is accompanied by the production of vast amounts of gas (both from the included sediments and from sediments shocked to high pressure) and that the volume expansion of these gases upon release to low pressures is the mechanism by which the shock-produced melt unit is dispersed around craters in sedimentary rocks and is one mechanism by which suevite is formed.

The apparent facility with which melt mixes with less shocked fragmented cold rock suggests that the vaporized rock subjected to peak shock pressures over 2000 kbar may also become mixed with cooler material surrounding it. The higher postshock particle velocities and lower viscosity of gases than melt implies vastly higher Reynolds numbers and more turbulent flow. Such mixing would probably condense the vaporized silicates (if not H_2O and CO_2) and may virtually eliminate the effects of an expanding cloud of rock vapor, as was discussed by *Rehfuss et al.* [1977]. Mixing of the vaporized rock and meteorite back into the solid debris which lands back in and around the crater might also increase the overall fraction of the projectile's kinetic energy which goes into heat within the crater.

Stage 5: Ejecta and Fallback (Figures 10b–10d and 11b–11d)

The ejection of material from the crater and the fall of rock back into the cavity begin during the excavation stage and then continue for several minutes after the excavation is complete for an impact on the scale of our model event (Figures 10 and 11). Most of the experimental data on hypervelocity impact ejecta paths are derived from photographs of ejection of debris after impact of small projectiles traveling at less than 10 km/s at the Ames Research Center's vertical gun range [*Gault et al.*, 1968; *Oberbeck*, 1977; *Oberbeck and Morrison*, 1976]. In these events, ejecta is thrown out through a restricted range of angles from the vertical (36°–44° in the experiments illustrated by *Oberbeck and Morrison* [1976]). The material derived from the center of the crater is ejected at higher velocities and slightly lower angles than the material from nearer the rim. The ejecta expands outward during and after the formation of the crater. On a larger scale, *Shoemaker* [1963] demonstrated that the ejecta first laid down on the rim is that from the top of the target stratigraphy and that it is progressively overlain by brecciated material from the lower units. By this process an overturned flap and rim deposit sequence are laid down.

We wish to discuss here particularly the role of the volatiles at this stage of the cratering process, referring the reader to the papers mentioned above as well as numerous others for discussions of the rock behavior. Volatiles can be produced

from at least three sources during an impact: (1) vaporization of silicates at pressures in excess of 1000 kbar, (2) decarbonation of limestones at pressures in exesss of ~400 kbar, and (3) vaporization of H_2O at pressures in excess of 100 kbar. Before proceeding further with a discussion of stage 5 we discuss briefly the behavior of bound and unbound water and carbonate.

The behaviors of bound and unbound or 'free' pore water during shock compression and release are strikingly different. The decomposition of hydrous minerals and, presumably, the release of the water bound in these minerals occur at pressures only slightly below those required for the onset of melting of rocks. Biotite, which shows signs of shock deformation, including kink bands, at only a few tens of kilobars, does not decompose until about 450 kbar [*Stöffler,* 1972]. Amphiboles (at least in the presence of melted feldspar or quartz) show shock-induced twinning at 50 kbar, but decomposition does not take place until about 450 kbar [*Stöffler,* 1972]. Thus the range between decomposition of the common hydrous silicates and onset of single-crystal or whole-rock melting is fairly small. Data on the pressure required to fuse granite totally do not exist at present; however, data for melting of basalt from the Lonar, India, impact crater suggest that melting begins at 600 kbar and is not complete until over 1000 kbar [*Kieffer et al.,* 1976*b*; *Schaal and Hörz,* 1977]. We assume that the pressures are somewhat (perhaps 100–200 kbar) lower for melting of granites because the constituent minerals are more compressible and therefore are subjected to higher internal energies and temperatures at a given shock pressure.

Melt rocks from craters in quartzofeldspathic gneisses at Manicouagan and West Clearwater are rarely vesicular and typically yield analyses of about 2% water [*Floran et al.,* 1978; *Bostock,* 1969; *Simonds et al.,* 1978*b*]. These low water contents are less than those required to saturate totally fused magmas at pressures over 1 kbar [*Carmichael et al.,* 1974]. Although the load pressures on the melts are probably less than 1 kbar, the melt may not vesiculate if it is only slightly oversaturated. At Manicouagan the melt did reach saturation and formed micropegmatite patches and quartz veins when the melt was about two-thirds crystallized [*Simonds et al.,* 1978*a*]. The West Clearwater melt may also have formed a free vapor phase slightly later in the crystallization sequence [*Simonds et al.,* 1978*b*]. We conclude that crystallographically bound water is (1) generally released only from rocks shocked to high pressures, comparable to those required for partial melting of the rock containing the minerals, and (2) generally not an important component of the active volatiles in the impact process. We therefore need only consider pore water and CO_2 from the decomposition of carbonates as mechanically 'active' volatiles.

Because typical porosities are 10–20% in the rocks considered, 'free' water is much more abundant than crystallographically bound water. Petrographic observations and high-resolution transmission electron microscope observations on weakly, moderately, and strongly shocked Coconino sandstone from Meteor Crater, Arizona, have demonstrated that such free water interacts with both the shocked minerals and the shock-produced melt [*Kieffer et al.,* 1976*a*]. The observations are restricted to the system quartz-water, but similar phenomena should be expected for any system in which hot water reacts with the crystalline material or dissolves in melt. Rock-water interactions are apparently negligible below ~100 kbar in weakly shocked Coconino sandstone. However, in rocks shocked to pressures above 100 kbar but below those required for melting (~250 kbar), hot water vapor reacts with quartz, coesite, and stishovite crystals to form an amorphous froth which occurs near or within regions that were the sites of pore water in the unshocked rock. The froth occurs in cracks within the quartz grains and around grain boundaries of coesite and stishovite. The froth must have formed late in the shock event because it occurs in and around grains of the high-pressure phases and because the delicate vesicles could not have withstood high pressure. The cryptovesicularity of the froth and the irregularity of the vesicle shapes suggest that it was produced by the violent separation of a gas phase (water vapor) from a liquid phase (water with dissolved silica) by 'fritting.'

Observations show that at pressures where melt is produced (>250 kbar for Coconino sandstone) the water and SiO_2 melt formed a supercritical fluid phase at high pressures [*Kieffer et al.,* 1976*a*]. Upon decompression, water exsolved from this mixture, resulting in the formation of spherical vesicles which pervade the lechatelierite. It should be emphasized that these vesicular areas encompass areas which originally contained many (dry) quartz grains and (wet) pores. Therefore the water was absorbed and mixed into silica melt over distances of a few millimeters. Simultaneously with vesicle formation, coesite crystals nucleated and grew in the glass.

The conclusions from this petrographic evidence are (1) that H_2O is an important volatile phase that influences the chemical and thermodynamic behavior of a rock-water system at all pressures above 100 kbar and (2) that water and rock (i.e., at least quartz and probably rocks in general) interact by a solution mechanism in the 100- to 250-kbar range and by supercritical fluid formation at pressures above 250 kbar. These latter mechanisms tend to reduce the expansion of the volatile phase from that expected from shocking an isolated pore water phase.

Decarbonation of limestone, dolomite, or marl should also produce a free volatile phase. Calculations of waste heat suggest that calcite begins to break down to CaO and CO_2 at about 450 kbar and completely decomposes at about 700 kbar. Shocking of pure carbonates might be expected to result in the formation of highly reactive oxides, which then recombine with CO_2 into carbonates. Decarbonation of impure carbonates should result in the formation of rocks containing natural 'concrete,' wollastonite, diopside, tremolite, or other calcium magnesium silicates. Documentation of such a process is difficult, and to our knowledge, reports of such materials at terrestrial craters do not exist except for a report of wollastonite formation around a limestone block at the Ries [*von Engelhardt et al.,* 1969] where the block reacted with surrounding hot glass. We suggest that a study of the fate of carbonates during impact, particularly of the fate of the high-pressure products, is needed.

Returning now to the discussion of stage 5, consider first the silicate vapor produced in the very high pressure region close to the meteorite. Our calculations, as well as calculations for the flow fields in craters of much larger events, indicate that large amounts of vaporized silicates are produced. *O'Keefe and Ahrens* [1976] suggest that one of the effects of this vast amount of gas is to accelerate the ejecta out of the crater over a broad range of angles with no pronounced preferential angle of ejection. Similarly, the calculations of *Trulio* [1977] suggest

that the gas pressure due to vaporized rock can deepen the excavation of an explosion and can accelerate the ejecta out of the crater early in the crater-forming process, before the bounding of the flow by the walls of the transient cavity. Trulio also emphasizes that the Reynolds numbers in the ejecta are very large and that all flow will be extremely turbulent. *Rehfuss et al.* [1977] suggested that great outward directed winds arise from the vaporized silicates and continue to accelerate the ejecta well after the mechanical formation of the crater is complete. *Jones and Sandford* [1977] suggested that large impacts are accompanied by a fireball which can rise adiabatically at tremendous speed, actually accelerating material above the earth's escape velocity. They calculate that inward directed winds of as much as 300 m/s several kilometers from the center are required to feed the rising fireball. Such winds presumably would have some effect on the terminal phases of the ejection process. Thus a variety of mechanisms related to the presence of silicate vapor have been postulated for excavating material out of the crater; existing experimental and field data only broadly constrain the possible mechanisms.

All of the above mentioned calculations and theories are for dry crystalline rock targets, which will yield rock vapor only from regions subjected to peak pressures well in excess of 1000 kbar. The calculations all assume that the silicate vapor does not interact with or condense on the less intensely shocked, comminuted material in the crater. Although the existence of such interactions is hypothetical, the field evidence discussed above for intermixing of liquid and solid phases strongly suggests that similar mixing of vapor, liquid and solid phases must also occur. The effect of mixing any of the vapors into the less shocked material would be to condense some of it and thus to reduce the expansion that it is able to produce. Thus the amount of expandable vapor produced and its effects may be overestimated in models that do not account for such intermixing (this effect is in addition to actual vapor-silicate chemical interactions under stage 4). However, impacts into water-saturated targets or into carbonates will produce many orders of magnitude more vapor than impacts into dry crystalline targets because H_2O and CO_2 vapor are produced throughout a volume of rock subjected to a much broader range of pressures than can produce silicate vapor (e.g., at all pressures above 100 kbar for H_2O and above 400 kbar for CO_2 in comparison to 800–1000 kbar for silicate vapor production). For example, the impact of the diabase meteorite at 24.6 km/s into permafrost, containing 22% by weight of water, will produce more than 1.75 km^3 of condensed water inside the 400-kbar isobar, equivalent to 2100 km^3 of vapor at standard temperature and pressure. If even only a fraction of that water escapes the crater, a massive cloud would be formed. For a similar impact into carbonate the volume of gaseous CO_2 produced at standard pressure and temperature would be 670 km^3. Thus although recondensation of the silicate vapor might preclude the above models from applying quantitatively to craters in crystalline rock, gas-driven effects as proposed might still take place during cratering events in sediments or limestone.

Although we believe that mixing of rock types and fragments of differing degrees of shock is extensive, the actions of the vapors produced, at least on the high-pressure zone near the meteorite, would probably be the most effective on the materials immediately adjacent to the sites of vapor production; that is, CO_2 gas would accelerate and interact most violently with the decarbonated carbonate from which it originated rather than, say, underlying or overlying bedrock; the silicate vapor would interact with and accelerate most intensely the melted silicate near it; and the H_2O vapor would interact with and accelerate most efficiently the sediments of its source region. It is therefore possible that the lack of observed melt or products of decarbonated limestone around the sediment target craters may occur because these fragments were blown away with the vapor and could not follow ballistic trajectories. This is plausible because sediments and carbonates shocked to sufficient pressures for the volatile components to be vaporized are usually vesicular, of very low density (viz., the highly shocked Kaibab limestone fragments or class 4 Coconino sandstone fragments and lechatelierite at Meteor Crater, Arizona), and rather small. It is only a slight extension to note that if such glass fragments were to become slightly more expanded, they would resemble vesicular volcanic ash. Part of such ash would undoubtedly fall back and be mixed into the ballistically ejected material, but because it is fine grained and volatile-rich, chemical alteration might quickly render it unrecognizable. Alternatively, if the material were to follow the ejection path of the vapors, it might be deposited on top of other debris or at the distal edges (particularly downwind) of the event. If this were the case, the missing 6–8 km^3 of 'melt' from the typical crater in sedimentary rocks would typically form a layer 5 m thick over an area of 20-km radius. Because all of the known terrestrial craters have undergone much more than 5 m of erosion, there is little chance of testing this hypothesis. However, an interesting possibility is that there are enigmatic deposits of bentonite and glass tuff layers thought to be the remnants of decomposed and fused sediments about 70 km southeast of the Ries within a sequence of Tertiary sediments [*Pohl et al.*, 1977]. They are of rhyolitic composition (glass recrystallized to montmorillonite) and are believed by most to be of volcanic origin. However, the facts that source areas for these volcanic beds are not known and that their fission-track age corresponds with the Ries event are suggestive of an association with the Ries. *Pohl et al.* [1977] have suggested that they might have formed during the jetting stage of impact. Under this hypothesis they might be expected to coincide geographically with the moldavite tektites, also attributed to the Ries impact. This presents a problem in that the bentonites occur to the south and east of the crater and the moldavites occur to the east. An alternative explanation might be that the bentonite and glass tuff beds represent some of the highly shocked and fused sediments from the sedimentary beds at the Ries, transformed to a vesicular, ashy melt, not during the jetting stage of the impact but in the region between approximately the 500- and 1000-kbar isobars, and subsequently transported with the expanding volatiles released.

In addition to this postulated glassy ash (which would probably originate from the vicinity of the 500-kbar isobar) we postulate that the suevite forms as a result of the interaction of melted and shocked sediments with large volumes of vapor derived from them, that is, from any sediments shocked to pressures above approximately 100 kbar. At the Ries the suevite is in the same stratigraphic position that clast-laden melt occupies at the crystalline target craters; that is, in both cases the melt equivalent unit lies on top of a less melt-rich polymict fragmental breccia. In the case of the Ries, outside of the crystalline ring the breccia is the Bunte breccia, and inside of

the crystalline ring it is on top of a polymict crystalline breccia; at Manicouagan and West Clearwater the melt sheet overlies a discontinuous melt-bearing fragmental breccia.

We suggest that the suevite formed as the original shock-melted sediments and other sediments shocked to over 100 kbar were dispersed as small fragments owing to the formation of vast quantities of sediment-derived gas. These fragments were probably transported in a volatile-lubricated flow, continually fed by expanding gases. Less shocked sediments, crystalline rocks, and melt bombs derived from the underlying crystalline basement rocks or from material thrown out on earlier, but higher, trajectories were continuously included in the flow. Some of the unique properties of the suevite at the Ries that suggest involvement of large volumes of volatiles during transport include (1) the high porosity of the suevite, (2) the occurrence of degassing vents, (3) an abundance of clays apparently formed while the suevite was still hot, and (4) evidence for CO_2 depletion in reaction rims around limestone inclusions. D. Stöffler (personal communication, 1979) has also called attention to the fact that the low melt content of the fallback suevite (4–6% by volume) cannot be the reason for the high 'equilibration' temperature derived from fission track studies of various minerals in the suevite and from the remanent magnetization [*Stöffler*, 1977]; these high temperatures may indicate the involvement of hot gases. We are greatly oversimplifying the concept of a suevite unit here in an effort to formulate a generalized process description. As was demonstrated by *Stöffler* [1977], the units generally described compositely as 'suevite' may, in fact, consist of several units of different melt contents and modes of deposition (e.g., suevite inside and outside of the crystalline ring at the Ries). Our model may apply most specifically to the lower melt-poor layers of the Ries suevite, described by *Stöffler* [1977, p. 443] as being deposited by a 'ground surge.'

We suggest that the aerodynamically shaped bombs which are found in most suevites (and, indeed, are included in the definition of suevite) are incidental inclusions and that these bombs originate from the nearly anhydrous crystalline basement rocks underlying the sedimentary strata. We envision that they were thrown up on high-angle trajectories and landed relatively late in the impact process, to be included in the flowing and settling suevite, which is also emplaced relatively late because it can originate from sediments shocked to pressures as low as 100 kbar. Thus in our model for the formation of suevite the glass bombs are not related to the early-stage history of suevite formation. Any volatile-containing target rock that is shocked to pressures sufficient for melting ends up as a suite of hydrated minerals in the suevite rather than as an anhydrous glass fragment as a result of either shock-rarefaction-associated heating or penecontemporaneous hydrothermal alteration. The glass bombs must have originated from (nearly) anhydrous rocks external to the rocks that formed the suevite.

We should reemphasize that whereas we consider suevite to be stratigraphically equivalent to a melt sheet in that (1) it originates at comparable pressures and initial distances from the meteorite and (2) the sequence of ejection of materials shocked to various pressures is more or less preserved until release to quite low pressures so that the relative order of ejecta is preserved, the suevite is quite different from a melt unit in that (1) it includes material shocked to pressures as low as the limiting pressure for H_2O vaporization, approximately 100 kbar, and (2) its mode of transport may be greatly altered at low pressures by volatile expansion.

Stage 6: Mechanical Modification (Figures 10d and 11d)

Mechanical and chemical modification of the crater probably takes place while the excavation and movement of melt are still in progress. Penecontemporaneous slumping and wall collapse are common at all terrestrial craters, and central uplifts are present in craters in crystalline rock greater than 5 km in diameter and in craters in sedimentary rock greater than 2–3 km in diameter. Impact melt begins to crystallize immediately because of quenching by the finely subdivided clastic debris which it contains. Such crystallization can be initiated in 10–100 s in craters such as Manicouagan [*Onorato et al.*, 1978], thus rapidly resulting in a large increase in the melt viscosity. The melt does, however, appear to retain sufficient fluidity to flow around irregularities associated with the slumping and rebound (e.g., at Manicouagan and West Clearwater [*Simonds et al.*, 1978*a*, *b*]). Our sketches (Figures 10 and 11) show modifications which we believe occur within a few minutes, but we do not know the extent to which the various processes are completed.

Melosh [1976] pointed out that the collapse of the relatively modest slopes associated with a transient crater requires failure of rock as if it had a coefficient of internal friction of only a few degrees instead of the 30°–40° characteristic of a wide range of granular and solid natural materials. *Hughes et al.* [1977] suggested that there is extensive seismic shaking after a cratering event, and this may be a mechanism for producing the required physical properties. This hypothesized behavior of the crater walls is inconsistent with the static mechanics of any known type of rock or ground that is not saturated with fluids. Thus if the effect of the seismic activity were to set up vertical accelerations which may be of the order of the acceleration of gravity or more, downward accelerations might effectively relieve the gravitational compressive stresses and allow the material to fail. Such a mechanism would be insensitive to the type of target rock or the presence of volatiles, a fact required by the solar-system-wide occurrence of crater modifications.

There is no doubt that the presence of pore fluid enhances slumping and collapse, just as high pore pressures promote landslide and slumps on a smaller scale [*van Terzaghi*, 1945]. *Moore* [1976, p. B34] showed that pore pressures only slightly exceeding the lithostatic load have an appreciable effect in wall modifications of missile impact in sediments containing water.

Stage 7: Hydrothermal and Chemical Alteration

Most terrestrial craters show the effect of the movement of groundwater into the impact breccias. Many of the less eroded craters, such as Meteor, Ries, East Clearwater, Brent, and Boltysh (see Table 1 for references), have lake or marine sediments filling part of the cavity. Studies of the melt sheets at Manicouagan and West Clearwater [*Simonds et al.*, 1978*a*, *b*] demonstrate that some water does move into the impact-formed melt sheet, oxidizing and hydrating the more reactive minerals and glass. At the Ries, degassing vents (Figure 1*b*) indicate that hot vapors, presumably steam, escaped from the suevite. The timing of these alterations and influx of water is

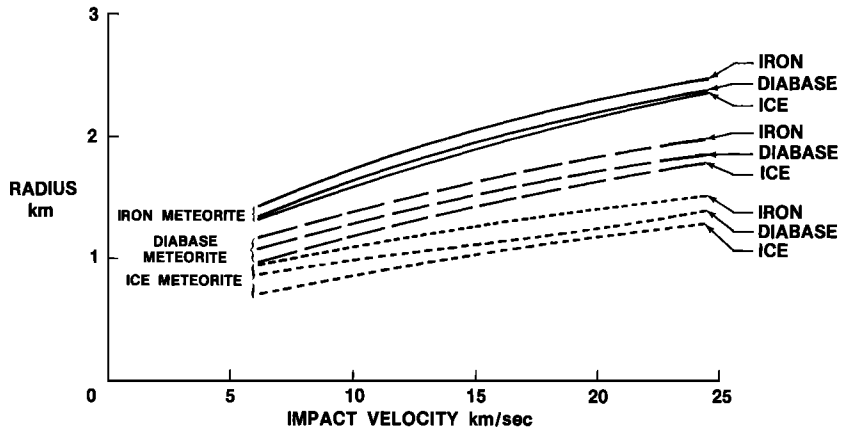

Fig. 13*a*. Radius to the 100-kbar isobar for the impact of a 1-km-diameter meteorite at velocities from 6.25 to 24.6 km/s.

not well established in most cases. However, at the Ries the rapid activity of hydrothermal water during cooling of the suevite is also indicated by the characteristic way of alteration of melt products and by the typical paragenesis of montmorillonite, analcime, and certain zeolites [*Stähle and Ottemann,* 1977; *Stöffler et al.,* 1977]. In the case of West Clearwater, *Phinney et al.* [1978] also established that the hydrothermal alterations took place at a temperature of several hundred degrees Celsius, implying that the groundwater influx took place before the rocks could cool.

Conclusions on Planetary Cratering

The generalized model for the cratering process developed above can be used to discuss impact craters not only on the earth and the moon but on the other planets and their satellites, providing one can specify the projectile type, target type, impact velocity, and whether or not the planet in question had an atmosphere. We believe that the calculations of attenuation, peak shock pressure, and penetration can be used with some confidence in predicting the distribution of peak shock pressure in the target, impact melt volumes, and the volume of impact-produced gas. We place less confidence in calculations of crater volume, because, as is discussed in Appendix B, the criteria that determine the size of the excavation are not well understood and selection of peak shock pressures characteristic of the bottom and rim of craters on the earth is difficult. These criteria may change with gravity on other planets. However, we do have a qualitative understanding of differences in the mechanics of excavation and melt transport as a function of target type. The major parameter appears to be the target's ability to yield H_2O, CO_2, or other relatively volatile species (e.g., SO_2). Impacts yielding these gases are likely to induce gas-driven transport of impact melt and other intensely shocked materials, dispersing the highly shocked materials over a wide area. In contrast, targets such as terrestrial crystalline rocks, which yield gas only from materials shocked to pressures well over 1000 kbar, will show a much more restricted distribution of the intensely shocked materials. In craters in the crystalline targets much of the melt is confined to sheets not extending much beyond the crater rim in its modified form.

Effects of Projectile Type

Peak shock pressures (Figure 9), calculated by using the simplified representation of the Hugoniot, show substantial variation with meteorite type. Stony meteorites produce pressures between those induced by iron and ice meteorites. Calculation of the position of a selected isobar (for example 100 kbar in Figure 13*a*) reveals that the radius to that isobar is greater for a 1-km-diameter iron object than for a 1-km stone or ice object. However, if the calculation is done for meteorites of the same mass, hence the same kinetic energy at a given

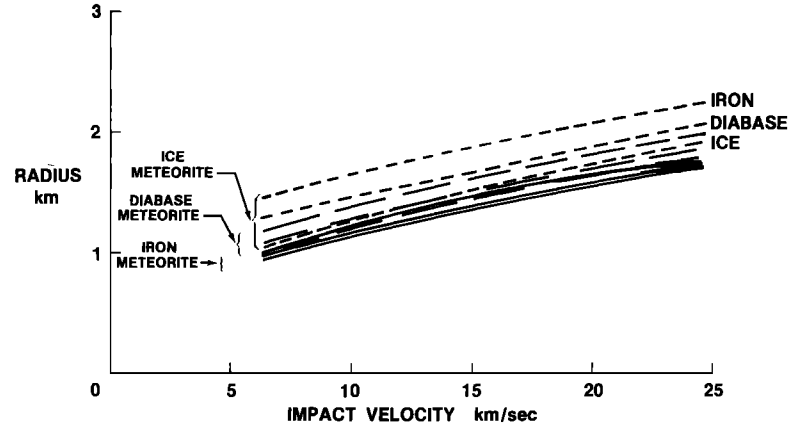

Fig. 13*b*. Radius to the 100-kbar isobar for the impact of iron, diabase, and ice meteorites of mass equivalent to a 1-km-diameter diabase meteorite. The increased diameter of the ice meteorite has a greater influence than the lower peak pressure that its impact induces, compared to the denser meteorite types.

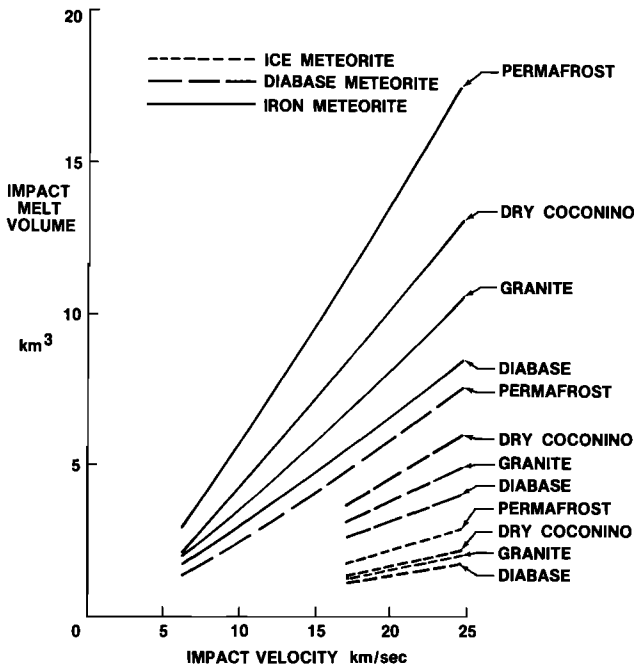

Fig. 14*a*. Volume of impact melt produced by the impact of 1-km ice, diabase, and iron meteorites at 6.25, 17, and 24.6 km/s. Volumes are calculated from the radii to the following isobars: permafrost, 400 kbar; dry Coconino sandstone, 600 kbar; granite, 750 kbar; and diabase, 1000 kbar. The volume of melt produced by each projectile is dominated by the minimum pressure required to induce melting; i.e., the lower the melting pressure, the larger the volume of melt. Thus the sedimentary targets yield more melt.

velocity, the pattern is reversed (Figure 13*b*): the impact of an ice meteorite produces a larger volume shocked to 100 kbar than that of an equally massive nonice meteorite. Thus for events of equal energy the increased volume of the low-density meteorite results in better coupling with the ground, which overrides the effect of the greater peak shock pressure induced by the denser objects. A similar dependence of impact melt volume on projectile type is shown in Figures 14*a* and 14*b*.

Encounter velocities for objects with orbits similar to earth-crossing asteroids are over 19 km/s for all planets in the inner solar system. *Shoemaker* [1977] calculates impact velocities of 34.2 km/s with Mercury, 27.3 km/s with Venus, 24.6 km/s with the earth, 21.7 km/s with the moon and 19.0 km/s with Mars. Peak pressures of at least 4000 kbar are generated by stony (diabase) objects striking even low-density, low-bulk-modulus targets, such as sand, at 19 km/s. Thus for the terrestrial planets, impact-induced peak shock pressures are more than adequate for melting substantial quantities of any target. Low-density objects such as comets, which are typically in more eccentric orbits than stony asteroids and which would have even higher encounter velocities, should be particularly effective in producing impact melt.

Penetration Mechanics

The calculations of penetration depths presented in Table 2 and Figure 7 indicate that at 24.6 km/s, even ice meteorites penetrate substantial distances and that all impacts can be approximated by a subsurface burst model. Surface bursts are appropriate, however, for slower impacts of ice and permafrost meteorites into rock. In the former (subsurface) case, spherical expansion of a shock from the apparent 'depth of energy deposition' is an appropriate model; in the latter (shallow) case, hemispherical expansion of a shock is more appropriate. However, the very eccentric orbits of most comets would result in higher encounter velocities than those for earth-crossing asteroids. Since the rms impact velocities for all the inner solar system exceed 19 km/s, the subsurface burst model should be usable for the terrestrial planets and their satellites (Figure 7).

The model calculations place the center of the melted zone well below the surface of the ground (see Figure 9, for example). (Although in our idealized model the melt zone does not extend all the way to the surface rocks, in a real impact, rock would be melted and vaporized along the whole penetration path of the meteorite.) Field evidence supports the model idea that the melt zone is centered at some depth because in craters such as the Ries, Popigai, and Lake St. Martin, which involved both a thick sedimentary cover and underlying crystalline basement, the recognizable melt geochemically matches the underlying bedrock and not the sediments.

The plug-shaped mass of sediments which must be pushed ahead of the penetrating projectile is not apparent geochemically either intermixed with the melt or as a separate debris

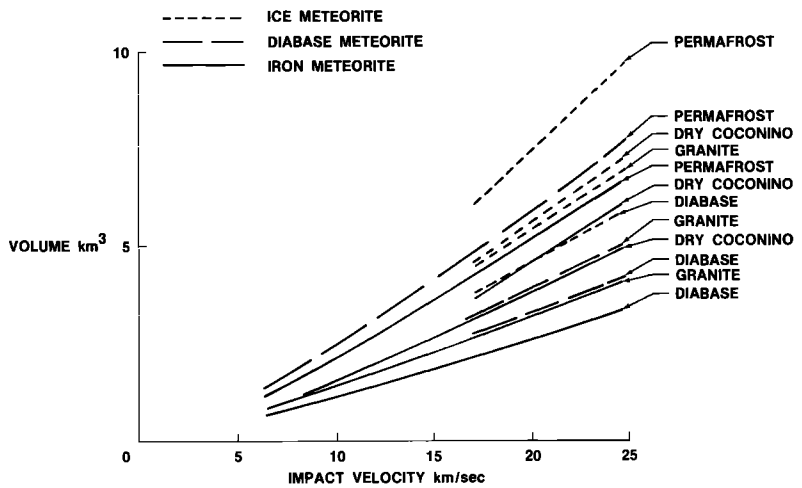

Fig. 14*b*. Calculations similar to those in Figure 14*a* but for meteorites of the same mass, equal to a 1-km sphere of diabase.

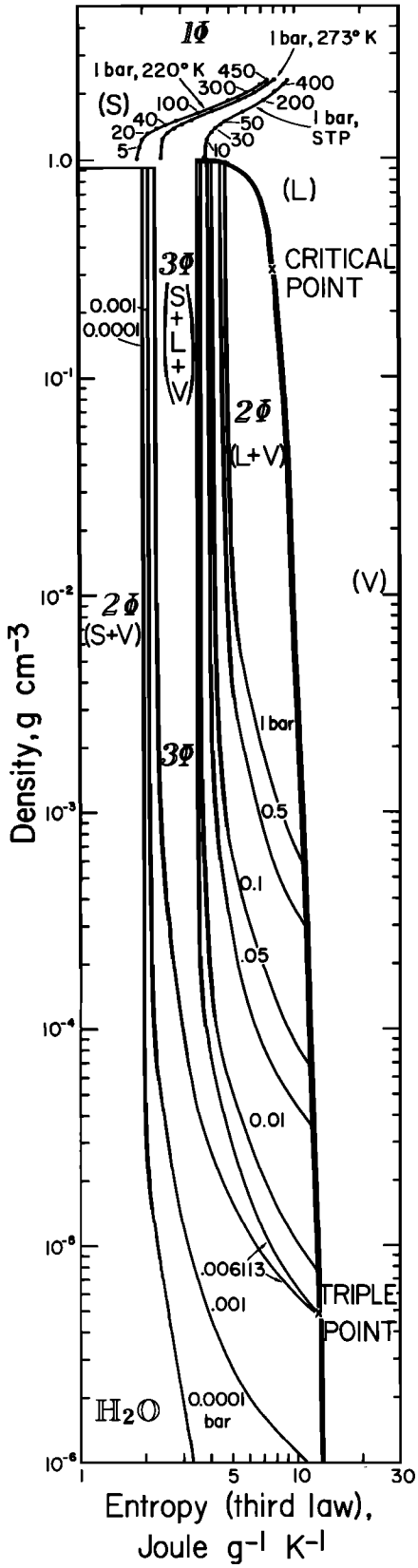

Fig. 15. Entropy-density phase diagram for H_2O and three Hugoniots for H_2O. The one on the right is from *Rice and Walsh* [1957] for liquid water centered at 1 bar, 20°C (STP). The center Hugoniot is calculated for ice at 0°C by subtracting the entropy of fusion and of cooling from 20° to 0°C from all states on the STP Hugoniot. It is assumed that the compression obtained is identical to the compression on the STP Hugoniot. The 'Martian' Hugoniot on the left is obtained by subtracting the entropy for cooling another 50°K.

unit. However, the sedimentary plug in front of the meteorite should not form more than a few percent of the total volume melted. Such low percentages of sediments are difficult to detect geochemically and may be present in the melts from the craters but at very low concentrations. The plug may be partly volatilized in high-velocity impacts and partly dispersed during ejection, further hindering its detection.

Finally, the agreement of our calculated crater depths (which are quite dependent on the model used for penetration depth) with observed estimates of depths of transient cavities based on field observations is surprisingly good, given the simplicity of the model. The depths are compatible with published estimates for the Ries [*Pohl et al.*, 1977] and Manicouagan [*Sweeney*, 1978]; however, when we scale our model down to the size of Meteor Crater, Arizona, the estimated depth is shallower than the measured depth [*Shoemaker*, 1963].

Volume and Form of Melt Deposits

The variations in mode of occurrence of melt in various types of terrestrial targets can be used to predict modes of melt occurrence on other planets. We conclude from study of published work on 32 terrestrial craters that melt sheets occur only in craters penetrating crystalline rocks with little or no sedimentary cover compared to the depth excavated. We further conclude that the fraction of the excavated volume which is recognizable melt in the terrestrial sedimentary craters is far less (as much as 2 orders of magnitude) than the 1–5% of melt that is characteristic of craters in crystalline rock. However, our modeling indicates that sediments should be melted to a greater extent than crystalline rocks. We propose that the resolution of this apparent paradox lies in the hypothesis that sediments are in fact melted to the same or greater degree as crystalline targets but that the resulting melt is no longer recognizable in the sedimentary craters. We conclude from this study that melt sheets are not found around craters in volatile-rich sedimentary rocks because steam from pore water and CO_2 from the breakdown of carbonates expand enormously and widely disperse the melted silicates, thus preventing formation of a melt sheet. Much of the melt and decarbonized limestone from the sediments may become fine ash which could be easily dispersed over a wide area. If such a material forms the upper deposits of a crater, it could have been eroded from all the terrestrial structures, since all have been subjected to at least several tens of meters of erosion. The melt found around craters in sedimentary rocks occurs as glass or crystalline lumps encased in less shocked debris and fine, often clay-rich matrix. Such breccias are often termed suevites in the literature. We suggest that these units are the stratigraphic equivalent of the melt sheets found in the crystalline target craters, although their mechanism of deposition is almost certainly quite different from that of the melt sheets owing to the large amount of gas evolved and the probably much lower temperature of the unit at the time of emplacement.

Crater Size and Impact Melt

The simplest and most direct application of our work to the study of the planets is to compare the range of rock types which we have studied with the surfaces of the various planets. Studies by *Cintala et al.* [1977] suggest that both the smooth plains and the cratered plains of Mercury are covered with a hard coherent rock much like the mare surfaces of the moon or the terrestrial crystalline targets. Samples of the moon have demonstrated, and infrared data and cosmic con-

densation modeling of Mercury suggest, that these planets are effectively volatile-free. Thus we would infer that both planets would contain craters with melt sheets and that the craters would be a bit smaller than those in highly fractured debris, although the magnitude of the effect is only a few percent in crater radius. The large craters in the dry, poorly consolidated lunar highlands should also yield melt sheets in accord with orbital observations and observations of the high abundance of melt in the Apollo 14, 16, and 17 collections [*Simonds,* 1975; *Simonds et al.,* 1977; *Warner et al.,* 1973].

On the other hand, Viking observations of Mars have suggested that volatiles are present on or near the Martian surface. Carbonates, water ice, CO_2 ice, and H_2O- or CO_2-saturated soils would all have a strong effect on Martian cratering mechanics. For all of these cases we would expect (1) a general absence of lunarlike melt sheets on Mars, (2) a cratering process quite different from lunar impact processes, and (3) where H_2O occurs in the surface soil [*Biemann et al.,* 1977], the possibility that the claylike soil of Mars [*Toulmin et al.,* 1977] may be in part the result of hydration of our hypothesized impact ash, perhaps made extremely reactive chemically by the effects of ultraviolet radiation [*Soderblom and Wenner,* 1978].

For the case of H_2O in the Martian soil or on the Jovian satellites we can speculate somewhat more quantitatively about the behavior of the water during impact. In Figure 15 we show an inferred Hugoniot for Martian conditions on an entropy-density graph for water (see *Kieffer and Delany* [1979] for details of entropy-density representations of Hugoniots and Appendix A of this paper for a discussion of the Hugoniot and release adiabats). The Martian Hugoniot, on the left of this figure, was obtained by taking the STP Hugoniot of liquid water, shown on the right, subtracting the entropy required to center the Hugoniot as ice at 0°C and then subtracting the entropy required to center the Hugoniot at the Martian surface temperature of 220°K. It is assumed that all shock states differ by the same entropy. On this graph, release adiabats are assumed to be isentropes and therefore vertical lines. The Martian surface pressure is about 6 mbar; thus a Hugoniot centered at 1-bar pressure corresponds to ice initially under about 20 m of overburden (at density 1.5 g/cm^3), not surface ice. However, for discussion of large impacts, the 1-bar Hugoniot is probably representative of much of the ice phase in the Martian soil.

Consider first ice which is released totally to Martian surface pressure, 6 mbar. If the ice is shocked to less than about 30 kbar, it will decompress totally into the solid + vapor ($S + V$) field and therefore sublimate to form a gas phase (the fate of all ice released to the surface pressure). This would perhaps correspond to ice near the periphery of a crater shocked to low pressures. Ice shocked to between 30 and about 100 kbar will decompress into the three-phase solid + liquid + vapor ($S + L + V$) field and form a liquid as well as a vapor phase. Ice shocked to pressures above 100 kbar will decompress through the two-phase ($L + V$) field to give a liquid + vapor mixture, which could begin evaporating as the pressure falls. Ice shocked to more than 500 kbar may enter the two-phase ($L + V$) field on the right-hand side of the critical point, with vapor condensing to give a two-phase ($L + V$) mixture. Extrapolation of the Martian Hugoniot suggests that only at pressures well above 1000 kbar will the released gas remain entirely vapor. Thus liquid water could be produced from any part of a Martian impact where the shock pressure is greater than 30 kbar, and vapor would be produced by any release to surface pressure because the Martian surface pressure is so low. Note, however, that if there is any overburden pressure on the ejecta, vapor production will be suppressed. Current cratering models are not detailed enough for us to specify the overpressure on various parts of the ejecta throughout the cratering process. However, if the debris lobes which form the rampart craters are more than 20 m thick, the overpressure on the volatile phase in those lobes is continuously 1 bar or more. In this case, if the texture of the debris lobes indicates a liquid component and if that liquid were H_2O, we might suggest, on the basis of Figure 15, that the liquid came from that part of the cratering event where shock pressures were greater than 100 kbar. Between 100 and 200 kbar, release to 1-bar pressure would produce a liquid phase only; at higher pressures, liquid and vapor are both produced. Although such an analysis is necessarily somewhat speculative at the present time, as geologic constraints on the impact units become available, such analyses should provide reasonable constraints on the sources of the units.

Cratering of the low-density icy satellites of Jupiter (Ganymede and Callisto) should produce vast quantities of melt (water) and gas. Ice should be melted at about 100 kbar, and impact into ice at high velocities yields approximately 5 times more melt than would be produced from diabase or granite targets (see Table 4). The abundant steam generated should drive the water out of the crater and spread it over a wide area in a manner similar to the transport mechanism that we propose for our instantly produced impact ash and clay in silicate targets. (Impacts into ice would probably result in huge snow or rain storms, depending on the ambient pressure and the initial temperature of the ice.) Because we hypothesize widespread dispersal of the melt derived from volatile-rich terrestrial targets, we expect relatively little of the material shocked to over 100 kbar to fall back into a large crater in ice.

Planetary Heating and Degassing

Kaula [1978] discussed the importance of the fraction of impact energy retained during accretion in determining planetary thermal evolution. Besides the normal energy partitioning during the compression and rarefaction stages of the impact event, heat transfer during the excavation and ejection stages is important in determining the fraction of meteorite kinetic energy that eventually resides in the target. Heat transferred into the volatile phases, for example, by ingestion of wet sediments or carbonates into the melt, can potentially be removed from the ground if the gas leaves the ground and escapes into the atmosphere or space. The magnitude of the energy transferred by gas escape cannot be predicted because we have no model for how much of the gas produced will be immediately recondensed on unshocked, essentially cold debris. We would infer that remixing is rapid and that a substantial fraction of the gas is recondensed by analogy with the rapid mixing of melt with the cold clasts. It is even possible that carbon dioxide from the breakdown of carbonates may partially recombine with CaO and MgO during the excavation process. The processes of gas recondensation and clast admixture into melt produced will both tend to confine the impact-induced heating within the planet rather than in ejecta which can cool by radiation. The relative importance of radiative heat loss from gas and condensation and cooling of impact-produced silicate vapor and melt by mixing with colder debris is not easily evaluated.

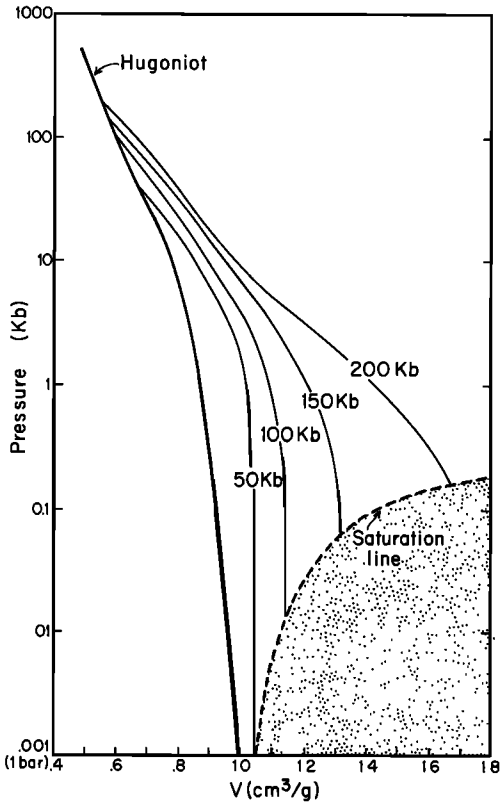

Fig. A1*a*. Pressure-volume Hugoniot and calculated release adiabats (data from *Riney et al.* [1970]) of water. At shock pressures greater than 50 kbar the release adiabats enter the two-phase field. (Figure from *Kieffer et al.* [1976*a*], reprinted with permission of Springer.)

Repeated impacts into targets with abundant H_2O and CO_2 could substantially alter the radial distribution of these materials in a planet. Primitive planetary surfaces have been saturated with impact craters which have reworked the planets to an average depth of several kilometers [*Hörz et al.*, 1976; *Short and Foreman*, 1972]. On volatile-rich planets, impact fracturing and heating could assist in releasing a gas to form a primitive atmosphere, although the efficiency of this process is unknown. Even if the recondensation of released volatiles is very efficient, the cumulative effect of repeated impacts on accreting planets would be to continually transfer volatiles toward the outer surface because in each event volatiles are released from depths shocked to, say, 100 kbar and then either released completely or redeposited near the surface with ejecta. By this process, volatiles might be enriched toward the outer layers of a growing planet.

APPENDIX A: BEHAVIOR OF VOLATILE-FREE AND VOLATILE-CONTAINING ROCKS UNDER SHOCK

Hugoniot data on dry crystalline rocks are relatively abundant [e.g., *Ahrens and Gregson*, 1964; *McQueen et al.*, 1967]. The Hugoniots of most crystalline substances are characterized by a low-pressure-phase regime (to a few hundred kilobars), a mixed-phase regime (to about 500 kbar), and a high-pressure-phase regime (at higher pressures). Through compression and phase changes, the crystalline rocks are typically compressed to about 0.55 of their initial volume by 1 Mbar and to 0.35 or 0.40 of their initial volume by 5 Mbar (Figure A1*a*). Release adiabat data are relatively scarce, but a few generalities can be assumed from single-crystal data [*Ahrens and Rosenberg*, 1968]. Upon release from pressures in the low-pressure-phase regime the decompression curves appear to represent decompression of the low-pressure phase and follow the shock Hugoniot quite closely. Upon release from the mixed-phase regime the release adiabats apparently reflect decompression of a metastable mixed-phase assemblage, possibly with some inversion to low-pressure phases. Upon release from the high-pressure-phase regime the release adiabats usually show inversion of the high-pressure phase to a low-pressure assemblage. In comparison to the behavior of the volatile materials discussed in the next section the overall volume changes and the volume changes across phase changes of the dry crystalline rocks are relatively small.

The behavior of volatiles is much more complex, and existing equation-of-state data on volatile-rich materials are fragmentary and often do not cover the range of pressures or materials necessary for an adequate description of hypervelocity impacts. However, enough data exist on various volatiles and volatile-rich materials (air, water, wet porous playa, carbonate) to allow some generalizations to be made. In this section an attempt is made to synthesize the existing data into a consistent model for volatile behavior under shock compression and adiabatic release.

Both air and water in pores affect their behavior under shock loading and release. *Kieffer* [1975*a*] summarized existing laboratory and field data on the behavior of air in the pores of terrestrial soils in an attempt to understand the formation of 'instant rock' by shock compression. This model accounts for (1) observed petrographic properties and densities of shock-lithified material from missile impact craters at

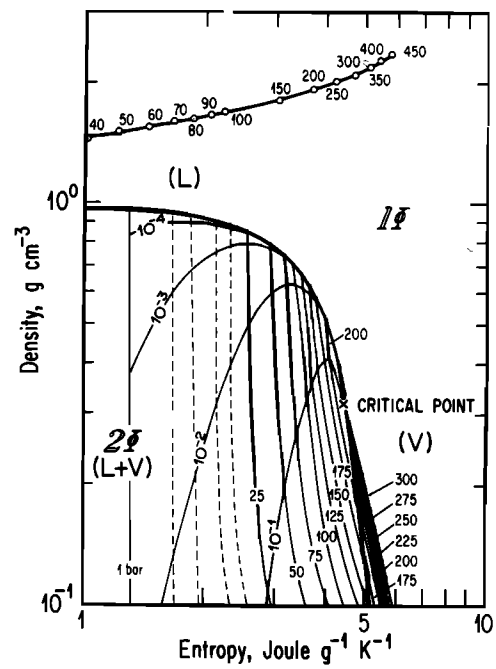

Fig. A1*b*. Hugoniot of water from 40 to 450 kbar on an entropy-density graph. Release adiabats, if they are assumed to be isentropes, are vertical lines on this graph. The saturation curve is the heavy curve separating the one-phase field (liquid or vapor) from the two-phase (liquid + vapor) field. Isobars (generally trending toward the upper left) and isopleths of constant mass fraction (generally trending toward the upper right, but bending over near the saturation curve) are shown. From an expanded graph such as this it is possible to read the mass fraction vaporized at any pressure on release. For a larger graph, see Figure 15, and for further details, see *Kieffer and Delany* [1979].

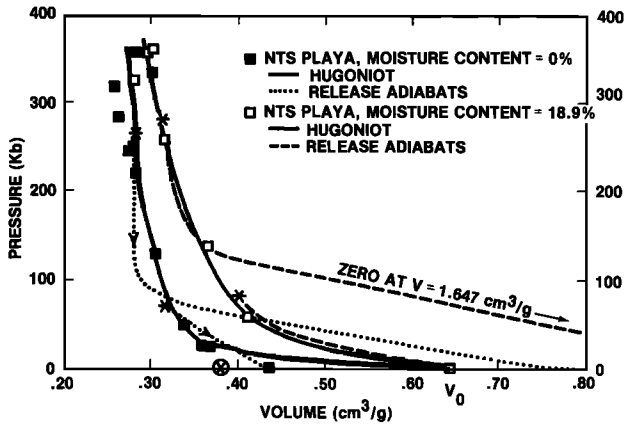

Fig. A2. *P-V* Hugoniots (solid curves) and release adiabats (dotted and dashed curves) for wet and dry Nevada test site (NTS) material of initial density 1.55 g/cm^3 (data from *Anderson et al.* [1966]; figure from *Kieffer* [1975*a*], reprinted with permission of D. Reidel).

White Sands, New Mexico, and from Meteor Crater, Arizona; (2) observed petrographic textures of lunar soil and lunar soil analogs experimentally shocked to known pressures in laboratory experiments; (3) theoretical calculations of the behavior of air and water under shock compression; and (4) measured Hugoniot and release adiabat data on dry and wet terrestrial soils and lunar regolith. Kieffer proposed that terrestrial soils form shock-lithified breccias if shock pressures are below about 50 kbar but are fragmented, rather than lithified, if pressures are in the range 100–200 kbar (10–20 GPa) because pore pressure due to shock heating of air and/or water in the pores exceeds the strength of the lithification mechanisms available in this range of pressures. At pressures above 200 kbar, lithification of porous samples can occur because the formation of intergranular glass or high-pressure phases at these pressures provides a lithification mechanism which has sufficient strength to withstand the pore pressure generated by shock heating. The same general sequence was found by *Stöffler et al.* [1975], although they assigned higher pressures to the range of lithification; this may have been because they used dry sand, whereas the natural soils studied by Kieffer all probably contained some H_2O which would affect the lithification process.

The pressure-volume behavior of water under shock heating is summarized in Figure A1*a*. The Hugoniot data for water were obtained by *Rice and Walsh* [1975]. Release adiabats have not been measured, but those calculated by *Riney et al.* [1970] from an assumed equation of state are shown. An alternative way of examining the shock equation of state of water is shown in Figure 15, which is a plot of entropy versus density for water and for the Hugoniot states of water [*Kieffer and Delany,* 1979]. An expanded version of this graph is shown in Figure A1*b*. Release adiabats of a liquid or gas can be assumed to be isentropes [*Kieffer and Delany,* 1979] and are therefore vertical paths on such a plot. From this plot the mass fraction vaporized upon release from any pressure can be read from the isopleths plotted in the two-phase field. Hugoniot states less than 40 kbar are not shown on the plot because those states and their release adiabats lie entirely within the single-phase liquid field. Incipient vaporization occurs upon release from 50 kbar [*Riney et al.,* 1970; *Kieffer and Delany,* 1979]. Upon release from pressures up to 275 kbar, partial vaporization occurs (continuous equilibrium is implicitly assumed). For example, using Figure 8 of *Kieffer and Delany,* [1979], one can see that upon isentropic release from 60 kbar, vaporization begins at approximately 2 bars of pressure, and about 6% of the liquid is vaporized by decompression to 1 bar; upon release from 100 kbar, vaporization begins at 10 bars, and about 20% of the liquid is vaporized by decompression to 1 bar. Similar behavior occurs to 275 kbar, from which decompression is through the critical point (221.29 bars, 4.47 × 10^7 ergs g^{-1} K^{-1}) and 50% of the liquid is vaporized upon decompression.

Upon decompression from pressures greater than 275 kbar the behavior differs. The compressed liquid expands isentropically around the critical point into the vapor phase, and as decompression brings the material to pressures lower than the critical pressure, a part of the vapor condenses to give a liquid fraction. For example, from 300 kbar, liquid begins condensing at about 220 bars, and nearly 50% of the vapor condenses. From 500 kbar, liquid begins condensing at 75 bars, and approximately 20% of the vapor condenses. At shock pressures of the order of 1 Mbar the unloading isentrope may remain entirely in the vapor-alone region at all pressures greater than 1 bar (entropies greater than 7.4 × 10^7 ergs g^{-1} K^{-1}). At all pressures the formation of a two-phase fluid is accompanied by enormous expansion of the volatile phase upon decompression.

The only shock and release data available for wet granular materials over a wide range of pressures are the data on wet Nevada test site playa material shown in Figure A2 [from *Anderson et al.,* 1966]. This playa material is a silica-rich deposit and therefore shows some features in common with the sediments of interest at cratering locales. In Figure A2 the curves on the left or bottom are for dry soils and exhibit the characteristic behavior of dry, porous materials which, at high pressure, undergo a phase change to a dense phase (generally believed to be one with silicon in six-fold coordination) and then revert to an expanded phase upon release. This behavior (shown on the release adiabat from ~270 kbar) has been interpreted to reflect melting or inversion of the high-pressure phase. The curves on the right or top are for wet playa. The release adiabat from the 280-kbar state in the wet material shows the initially steep decrease with pressure characteristic of the high-pressure phase but then shows a large increase in specific volume at low pressure; there is considerable experimental uncertainty in the detailed form of this release curve. *Anderson et al.* [1966] attributed the expansion to vaporization of water, and this interpretation is consistent with the behavior of water shown in Figure A1*a*. Our conclusion then is that the behavior of wet materials during release from shock compression above about 100 kbar is dominated by the water, not the rock, component. In an actual cratering event the effect of water shows up as a change in the energy-diameter scaling relations—craters in water-saturated sediments are typically 20–50% larger than their energy equivalents in dry soils (some unknown part of this enlargement is due to differences in mechanical strength at low pressures). This effect was recognized by *Higgins and Butkovich* [1967], and the influence of water in rocks on the effects of underground nuclear explosions was modeled reasonably successfully by Butkovich simply by treating wet soil as a two-component system in which there was no interaction between the rock and the water. This model is called the water boost model. (Note that the petrographic observations described in the text show that the assumption of no water-rock interaction is not valid at pressures above which water is vaporized.)

The only equation-of-state data available on carbonates are the data of *Ahrens and Gregson* [1964] on calcite, marble, and limestones to pressures of about 300 kbar and the data of *Kalashnikov et al.* [1973] on calcite, dolomite, magnesite, and wet and dry chalk to pressures of about 1.2 Mbar. Release adiabats of these substances have not been measured, and therefore no information is available about decarbonation upon release. The Hugoniot data indicate that calcite is intermediate between a granite and a diabase in its shock compression characteristics, i.e., that carbonates resemble crystalline rocks as far as shock compressibility. We estimated the pressures required to cause decarbonation as follows: We assumed that decarbonation occurred if the release temperature at 1 bar exceeded 894°C, the temperature at which calcite breaks down to CaO + CO_2. We assumed that the release adiabat of calcite was the same as the Hugoniot (only from pressures lower than those at which decarbonation begins) and assumed that all waste heat (given by the area between the Rayleigh line and the Hugoniot) was retained in the calcite. An energy of 9×10^9 ergs/g is required to bring calcite to the temperature at which breakdown begins; this is reached at about 450 kbar; the latent heat of the breakdown is 16×10^9 ergs/g, and this additional energy is supplied by shock to 700 kbar; therefore we take 450–700 kbar as the range of pressures required for partial to total decarbonation of calcite. This simple model ignores phase transitions reported at 30, 45, and 95 kbar in calcite [*Ahrens and Gregson,* 1964], but latent heat subtractions arising from these phase changes would be approximately compensated for by offset of the release adiabats to lower volumes, and therefore to some degree, offsetting approximations have been introduced.

APPENDIX B: SIMPLIFIED REPRESENTATION OF HUGONIOTS AND RELEASE ADIABATS

Because of the volume changes which occur across phase changes it is not possible to represent accurately the shock Hugoniots and release adiabats of all of the substances of interest by the type of simple, universally applicable equation of state required for a comparative study such as this. We have therefore made two simplifying assumptions:

1. Shock velocity (U_s)–particle velocity (u_p) data (to as high a pressure as data are available) can be fitted with a straight line which will give an equation of state which represents first-order effects in compressibility adequately. A single straight line is drawn through low- and high-pressure data. This line is represented by

$$U_s = c_0 + su_p \tag{B1}$$

where c_0 is constant (not to be confused with the sound speed of the low-pressure phase (see below)) and s is the slope of the averaged U_s-u_p curve. 'Effective bulk moduli' (K_0) and 'bulk moduli pressure derivatives' are obtained from

$$K_0 = c_0^2\rho_0 \tag{B2}$$

$$n = 4s - 1 \tag{B3}$$

[after *Ruoff,* 1967], where ρ_0 is ambient density. Fitting of the data in this way allows us to use a simple and convenient Murnaghan equation for the Hugoniot and release adiabats:

$$P = \frac{K_0}{n}\left[\left(\frac{V_0}{V}\right)^n - 1\right] \tag{B4}$$

In this equation, P is the pressure, V is the volume, and V_0 is the volume at ambient pressure, assumed to be 1 bar.

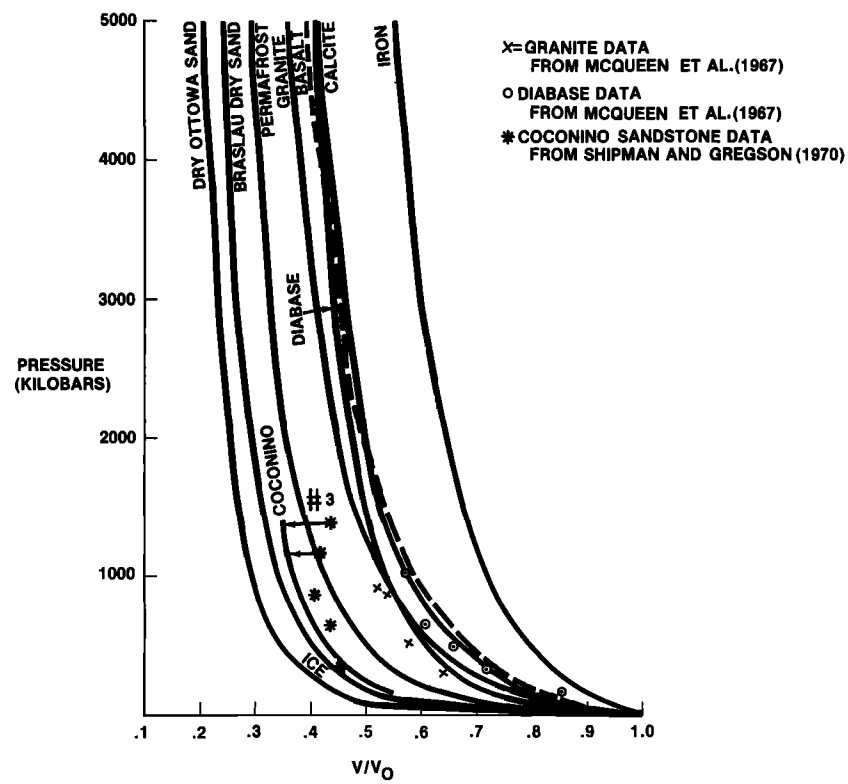

Fig. B1. Pressure-volume relations from (4) using the values of bulk modulus and derivative given in Table 2. For most of the materials, measured data would lie on these lines; measured data points for the worst fit cases (Coconino sandstone, granite, and diabase) are shown.

TABLE B1. Parameters Used for Equation of State

Material	ρ_0, g/cm	c_0, km/s	s	K_0, kbar	n	Reference and Comments
Iron	7.86	3.80	1.58	1135	5.32	*Al'tshuler et al.* [1978]
Aluminum	2.75	5.30	1.37	772	4.48	*Gault and Heitowit* [1963]
Diabase	3.00	4.48	1.19	602	3.76	*McQueen et al.* [1967]
Basalt	2.86	2.60	1.62	193	5.5	*Gault and Heitowit* [1963]
Granite	2.63	3.68	1.24	357	3.94	*McQueen et al.* [1967]
Calcite ('carbonate')	2.67	3.80	1.42	385	4.68	*Kalashnikov et al.* [1973]
Permafrost (water saturated)	1.96	2.51	1.29	123	4.15	*Anderson* [1967] (100% saturated frozen sand)
Coconino sandstone	2.00	1.50	1.43	45	4.72	*Shipman and Gregson* [1971] (note Figure 4, which shows that these parameters slightly overestimate compression at high pressure)
Dry sand (1)	1.60	1.70	1.31	46	4.24	*Braslau* [1970] (these values are used in the model)
Dry sand (2)	1.65	1.00	1.42	16.5	4.66	*Anderson* [1967] (for comparison with values of *Braslau* [1970], above)
Ice	0.91	1.28	1.56	15.02	5.23	*Anderson* [1967]
Water	1.00	1.48	1.60	22.00	5.40	*Rice and Walsh* [1957] (for comparison with ice, above)

Parameters c_0, s, K_0, and n represent 'effective' moduli representing behavior averaged by fitting linearly to U_s-u_p curves over a wide range of pressures (see text). They do not represent the moduli of the low-pressure phases except in the accidental case where there are no phase changes or the phase changes represent minor volume changes.

Although phase changes are approximately accounted for in the overall compression, the parameters c_0, bulk modulus K_0, and pressure derivative n so obtained do not represent the sound speed or bulk moduli of either the low-pressure initial phases or the high-pressure shock state phases except in accidental cases where there are no phase changes. Rather, they represent average equation-of-state parameters which reproduce known pressure–particle velocity and pressure-volume data to less than 10% and therefore allow calculation of bulk thermodynamic properties and extrapolation of measured data. The equations of state used and their relation to measured data are shown in Figure B1. Only in the cases of water, ice, aluminum, iron, and perhaps calcite, for which either there are no high-pressure transitions in the shock state or for which the transitions have very small volume changes, do the parameters obtained from equations (B1)–(B3) give the correct moduli of the low-pressure phases. The parameters and moduli used for the representative substances are given in Table B1.

2. The release adiabats are adequately approximated by the Hugoniot. The Hugoniot is a good approximation to release adiabats for metals or materials which do not undergo phase changes characterized by large volume differences [e.g., *Walsh and Christian,* 1955; *McQueen et al.,* 1967]. On the other hand, for high-velocity impacts such as those considered here, silicate materials are generally shocked into high-pressure phases. (Very complex release adiabats characteristic of materials which can undergo both phase changes to denser phases under shock compression and to highly expanded vapor phases upon release are shown in Figure A2.) The release from these states generally lies not along the Hugoniot but along an adiabat characteristic of the high-pressure phase, with reversion at 50–100 kbar to an expanded low-pressure phase [*Ahrens and O'Keefe,* 1971]. The release from the high-pressure phase will generally follow a P-V curve which lies below the averaged Hugoniot derived above; the reversion to the low-pressure phase will generally cross over the Hugoniot derived above, to lie above it at low pressures. In a general way, therefore, the averaged Hugoniot used in this model accounts for an 'averaged' release behavior, and we do not believe that serious error results from lack of detail in the release adiabat descriptions of the solid phases. The processes least adequately represented by this approximation are irreversible compaction and low-pressure expansion of the volatile phases. Both of these effects become very important at pressures of a few to a few tens of kilobars, and therefore calculated attenuation rates at low pressures have relatively large uncertainties, as do the estimated crater volumes. However, at that point, much of our process description is based on field results rather than on theory.

As can be seen from Table B1 and as has been demonstrated throughout the calculations in the discussion section, the shock properties of the substances of interest allow them to be grouped into four classes: (1) crystalline, nonporous rocks, which, along with the metals, have real or 'effective' bulk moduli of the order of hundreds to 1000 kbar; (2) permafrost and wet sands (data not given), which have effective bulk moduli of the order of 100 kbar; (3) dry sands and sandstones with effective bulk moduli of the order of 50 kbar; and (4) ice (and water) with actual bulk moduli of 15–25 kbar. The effective bulk modulus derivatives n generally range from 4 to 6, and for many substances, $n = 4.5$ or 5 is a good approximation. The lowest value of n found for any substance examined was $n = 2.6$ for dunite, and the highest values were $n = 5.5$ for the *Gault and Heitowit* [1963] equation of state for basalt and 5.4 for water.

APPENDIX C: BOUNDARY CONDITIONS ON THE CRATER FLOOR AND AT THE WALLS

The processes which determine the floor and wall isobars are complex. Material properties, crater size, particle velocities (and therefore, ultimately, meteorite impact velocity), and gravitational field are all important. The reader is referred to *Schock* [1977] and *Curran et al.* [1977] for recent reviews and syntheses of work pertaining to this subject.

The nature of the target material is important because the microstructure of the material determines the mode of failure. Brittle, ductile, and porous rocks all behave differently. Dry porous rocks behave differently from water-saturated rocks (and, by inference, from ice-saturated rocks) because in the former case the failure of the rock is controlled by the strength of the pore wall but in the latter the compressibility and thermodynamic state of the pore fill is also important.

In general, rocks are fragmented by stresses comparable to or greater than the dynamic yield strength, which is a few

TABLE C1. Peak Pressures at Bottoms and Rims of Craters

	Peak Pressure, kbar		
	Bottom	Rim	Reference
		Laboratory Impacts	
Granite		~30	
Loose sand		~5	*Stöffler et al.* [1975]
		Explosion Craters	
Shallow (~3 m) buried megaton event in 'hard rock'		1–4	*Cooper* [1977]
Shallow (3 m) buried megaton event in unsaturated porous rock		~0.5–2	*Cooper* [1977]
Deep (200 m) events in 'hard rock'		~1	*Cooper* [1977]
Deep (100 m) events in unsaturated porous rock		0.1	*Cooper* [1977]
		Meteorite Craters	
Brent (crystalline)	>230		*Robertson and Grieve* [1977]
Ries (crystalline)	>160		*von Engelhardt and Graup* [1977]
West Clearwater (crystalline)	200–250		*Simonds et al.* [1978*b*]
Charlevoix (crystalline)	>225		*Robertson* [1975]
Lake St. Martin (crystalline)	~150		*Simonds and McGee* [1979]
Gosses Bluff (sandstone)	>140		using data of *Milton et al.* [1972] and *Robertson and Grieve* [1977]

kilobars. Yet field evidence clearly demonstrates that rocks which have experienced pressures as high as 200 kbar (see discussion below) are still nearly in situ in the craters. A particle is excavated from a crater only if it is accelerated to sufficient velocity and at an appropriate angle to be ejected beyond the crater rim. Thus the velocity obtained by the particle, the distance that it must travel (i.e., the size of the crater), and the gravitational field that it must work against are all important. Keeping the gravitational effect in mind for later discussion, consider here only terrestrial craters.

We have found the data shown in Table C1 for bottom and rim isobars from field and laboratory data.

Although the compilation is by no means complete, it illustrates the complexity introduced by both scale and lithology. Because we are concerned with modeling of large craters, we have attempted to account for the effect of variation of target strength on crater volume by using different rim and bottom isobars based on the field evidence cited above: 10 kbar as the rim pressure for craters in crystalline rock, 2 kbar for craters in permafrost, and 1 kbar for craters in dry sand, Coconino sandstone, or ice. We take 250 kbar as the isobar at the bottom for all craters. We recognize that the data on Gosses Bluff, Steinheim, and Flynn Creek suggest that this isobar may be lower for the craters in sediments and discuss the effect of varying bottom and rim isobars in the text and in Table 3.

NOTATION

a, b coefficients of paraboloid $Y = aH^2 + b$ fitted to crater shape.
c sound speed.
c_m, c_t sound speed in compressed meteorite and target, respectively.
c_{0m}, c_{0t} sound speed at zero pressure in meteorite and target, respectively.
d, d' diameter of uncompressed and compressed meteorite, respectively.
E internal energy.
E_0 initial energy of meteorite.
E_T total energy.
ΔE_w waste heat.
f_f fraction of the original kinetic energy of the meteorite transmitted to the target by the end of stage 2.
f_j fraction of the original kinetic energy of the meteorite carried off during jetting.
f_m fraction of the original kinetic energy of the meteorite retained by the meteorite during energy partitioning during stage 2, substage A.
f_t fraction of the original kinetic energy of the meteorite transferred to the target during stage 2, substage A.
H depth of crater, assumed to be a paraboloid $Y = aH^2 + b$.
K_0 adiabatic bulk modulus.
n adiabatic bulk modulus derivative.
p penetration depth.
P_0, P ambient pressure and shock pressure, respectively.
r radius.
r_0 radius of volume (assumed to be spherical or, in a few cases, hemispherical) of target rock which would contain all of the initial meteorite energy partitioned equally into kinetic and internal energy at pressure P.
r_{0m} original radius of meteorite.
r_{0t} radius of target rock containing energy deposited in target during stage 2, substage A.
$R = r/r_0$.
s slope of the linear shock velocity–particle velocity relation
t_1, t_2 duration of compression stage 2, substages A and B, respectively.
u_p particle velocity.
u_m, u_t particle velocity in the meteorite and target, respectively.
$u_{r,p}$ particle velocity attained in the rarefaction.
U_s shock velocity.
$U_{s,m}$ shock velocity in meteorite.
v_i impact velocity.
V_0, V volume at ambient pressure and under compression, respectively.
$X = P/K_0$.
Y distance from center line of paraboloid $Y = aH^2 +$

b fitted to crater shape to a point on the crater wall.
Z scale of irregularity on meteorite or ground.
ρ_{0m}, ρ_{0t} original densities of meteorite and target, respectively.

Acknowledgments. This manuscript was greatly improved by critical reviews from W. von Engelhardt, R. A. F. Grieve, F. Hörz, D. Milton, H. Moore, D. Orphal, and D. Stöffler. Their help is gratefully acknowledged, although the authors are solely responsible for errors which may remain. S. W. Kieffer thanks Gene Shoemaker for suggesting the petrographic study of the shocked Coconino sandstone which led to the recognition of the importance of volatiles during cratering. S. W. Kieffer was supported from 1974 to the present by NASA grant NSG-7052 at the University of California in Los Angeles for much of this work. C. H. Simonds is supported through task order 60 of NASA Contract NAS 9-15425 for operation of the Lunar Curatorial Laboratory by Northrop Services, Inc.

REFERENCES

Adams, J., and T. McCord, Mercury: Evidence for an anorthositic crust from reflection spectra, paper presented at the Meeting of the Division of Planetary Science, Amer. Astron. Soc., Honolulu, Hawaii, 1977.

Ahrens, T. J., and D. M. Cole, Shock compression and adiabatic release of lunar fines from Apollo 17, *Geochim. Cosmochim. Acta, 3,* 2333–2345, 1974.

Ahrens, T. J., and J. R. Gregson, Shock compression of crustal rocks: Data for quartz, calcite, and plagioclase rocks, *J. Geophys. Res., 69,* 4839–4874, 1964.

Ahrens, T. J., and J. D. O'Keefe, Shock melting and vaporization of lunar rocks and minerals, *Moon, 4,* 214–247, 1972.

Ahrens, T. J., and J. D. O'Keefe, Equations of state and impact-induced shock wave attenuation on the moon, in *Impact and Explosion Cratering,* edited by D. J. Roddy, R. O. Pepin, and R. B. Merrill, pp. 639–656, Pergamon, New York, 1977.

Ahrens, T. J., and J. T. Rosenberg, Shock metamorphism: Experiments on quartz and plagioclase, in *Shock Metamorphism of Natural Materials,* edited by B. French and N. Short, Mono, Baltimore, Md., 1968.

Allen, W. A., H. L. Morrison, D. B. Ray, and J. W. Rogers, Fluid mechanics of copper, *Phys. Fluids, 2,* 329, 1959.

Al'tshuler, L. V., S. B. Kormer, A. A. Bakanova, A. P. Petunin, A. I. Funtikov, and A. A. Gubtin, Irregular conditions of oblique collision of shock waves in solid bodies, *Sov. Phys. JETP,* Engl. Transl., *14,* 968, 1962.

Al'tshuler, L. V., K. K. Krupnikov, B. N. Ledener, V. I. Zhuchnikhin, and M. I. Brazhuik, Dynamic compressibility and equation of state of iron under high pressure, *Sov. Phys. JETP,* Engl. Transl., 34, 606–614, 1978.

Anderson, G. D., The equation of state of ice and composite frozen soil material, interim technical report, project FGU-6392, contract DAAG 23-67-C-0D11, SRI Int., Menlo Park, Calif., 1967.

Anderson, G. D., G. E. Duvall, J. O. Erkman, G. R. Fowles, and C. P. Peltzer, Investigation of equation of state of porous earth media, *Tech. Rep. AFWL-TR-65-146,* p. 176, SRI Int., Menlo Park, Calif., 1966.

Biemann, R., et al., The search for organic substances and inorganic volatile compounds in the surface of Mars, *J. Geophys. Res., 82,* 4641, 1977.

Birkhoff, G., D. P. MacDougall, E. M. Pugh, and G. Taylor, Explosives with lined cavities, *J. Appl. Phys., 19,* 563, 1948.

Bjork, R. L., Analyses of the formation of Meteor Crater, Arizona: A preliminary report, *J. Geophys. Res., 66,* 2379–2387, 1961.

Bjork, R. L., K. N. Kreyenhagen, M. H. Wagner, Analytical study of impact effects as applied to the meteoroid hazard, *NASA Contract. Rep. CR-757,* 1967.

Bostock, H. H., The Clearwater Complex, New Quebec, *Geol. Surv. Can. Bull., 178,* 1969.

Braslau, D., Partitioning of energy in hypervelocity impact against loose sand targets, *J. Geophys. Res., 75,* 3987–3999, 1970.

Carmichael, I. S. E., F. J. Turner, and J. Verhoogen, *Igneous Petrology,* 737 pp., McGraw-Hill, New York, 1974.

Carr, M. H., and G. G. Schaber, Martian permafrost features, *J. Geophys. Res., 82,* 4055–4066, 1977.

Carr, M. H., et al., Preliminary results from Viking orbiter imaging experiment, *Science, 193,* 766–776, 1976.

Carr, M. H., L. A. Crumpler, J. A. Cutts, R. Greeley, J. E. Guest, and H. Masursky, Martian craters and emplacement of ejecta by surface flows, *J. Geophys. Res., 82,* 4055–4065, 1977.

Charters, A. C., and J. J. Summers, Comments on the phenomena of high-speed impact, *Rep. NOLR-1238,* pp. 200–221, U.S. Nav. Ordnance Lab., Silver Spring, Md., May 1959.

Cintala, M. J., C. A. Wood, and J. W. Head, The effect of target characteristics on fresh crater morphology: Preliminary results for the moon and Mercury, *Proc. Lunar Sci. Conf. 8th,* 3409–3425, 1977.

Consolmagno, G. J., and J. S. Lewis, The evolution of icy satellite interiors and surfaces, *Icarus, 34,* 280–293, 1978.

Cooper, H. F., Jr., Empirical studies of ground shock and strong motions in rock, *Rep. DNA 3245F,* p. 85, R & D Ass., Santa Monica, Calif., 1973.

Cooper, H. F., Jr., A summary of explosion cratering phenomena relevant to meteor impact events, in *Impact and Explosion Cratering,* edited by D. J. Roddy, R. O. Pepin, and R. B. Merrill, pp. 11–44, Pergamon, New York, 1977.

Croft, S. K., S. W. Kieffer, and T. J. Ahrens, Low-velocity impact craters in ice and ice-saturated sand with implications for Martian crater count ages, *J. Geophys. Res., 84,* 8023–8032, 1979.

Curran, D. R., D. A. Schockey, L. Seaman, and M. Austin, Mechanisms and models for cratering in earth media, in *Impact and Explosion Cratering,* edited by D. J. Roddy, R. O. Pepin, and R. B. Merrill, pp. 1057–1087, Pergamon, New York, 1977.

Currie, K. L., Geology and petrology of Manicouagan resurgent caldera, Quebec, *Geol. Surv. Can. Bull., 198,* 153, 1972.

Dence, M. R., A comparative structural and petrographic study of probable Canadian meteorite craters, *Meteoritics, 2,* 249–269, 1964.

Dence, M. R., Dimensional analyses of impact structures, *Meteoritics, 8,* 343–344, 1973.

Dence, M. R., R. A. F. Grieve, and P. B. Robertson, Terrestrial impact structures: Principal characteristics and energy considerations, in *Impact and Explosion Cratering,* edited by D. J. Roddy, R. O. Pepin, and R. B. Merrill, pp. 247–276, Pergamon, New York, 1977.

Eskola, P., On volcanic necks in Lake JänisJärvi in eastern Finland, *Geol. Tutkinalseitos Bull., 55,* 3–13, 1921.

Firsov, L. V., The meteoritic origin of the Puchezh-Katunki Crater (in Russian), *Geotektonika,* 106–118, 1965.

Floran, R. J., and M. R. Dence, Morphology of the Manicouagan ring-structure, Quebec, and some comparisons with lunar basins and craters, *Proc. Lunar Sci. Conf. 7th,* 2845–2865, 1976.

Floran, R. J., R. A. F. Grieve, W. C. Phinney, J. L. Warner, C. H. Simonds, D. P. Blanchard, and M. R. Dence, Manicouagan impact melt, Quebec, 1, Stratigraphy, petrology, and chemistry, *J. Geophys. Res., 83,* 2737–2760, 1978.

Fredriksson, K., A. Dube, D. J. Miton, and M. S. Balasundaram, Lonar Lake, India: An impact crater in basalt, *Science, 180,* 862–864, 1973.

Gary, M., R. McAfee, and C. L. Wolf (Eds.), *Glossary of Geology,* American Geological Institute, Washington, D. C., 1974.

Gault, D. E., and R. Greeley, Exploration experiments of impact craters formed in viscous-liquid targets: Analogs for Martian rampart craters?, *Icarus, 34,* 486–495, 1978.

Gault, D. E., and E. D. Heitowit, The partition of energy for hypervelocity impact craters formed in rock, *Proc. Hypervelocity Impact Symp. 6th,* 420–456, 1963.

Gault, D. E., and H. J. Moore, Scaling relationships for microscale to megascale impact craters, *Proc. Hypervelocity Impact Symp. 7th, 6,* 341–351, 1965.

Gault, D. E., E. M. Shoemaker, and H. J. Moore, Spray ejected from the lunar surface by meteoroid impact, *NASA Tech. Note TN D-1767,* 39 pp., 1963.

Gault, D. E., W. L. Quaide, and V. R. Oberbeck, Impact cratering mechanics and structures, in *Shock Metamorphism of Natural Materials,* edited by B. French and N. Short, pp. 87–99, Mono, Baltimore, Md., 1968.

Gentner, W., H. J. Lippolt, and O. A. Schaeffer, Argonbestimmungen an Kaliummineralien, XI, Die Kalium-Argon-Alter der Gläser des Nördlinger Rieses und der böhmischmährischen Tektite, *Geochim. Cosmochim. Acta, 27,* 191–200, 1963.

Grieve, R. A. F., Petrology of the impact melt at Mistastin Lake Crater, Labrador, *Geol. Soc. Amer. Bull., 86,* 1617–1629, 1975.

Grieve, R. A. F., The melt rocks at Brent Crater, Ontario, Canada, *Proc. Lunar Sci. Conf. 9th,* 2579–2608, 1978.

Grieve, R. A. F., M. R. Dence, and R. B. Robertson, Cratering processes: As interpreted from the occurrence of impact melts, in *Impact and Explosion Cratering,* edited by D. J. Roddy, R. O. Pepin, and

R. B. Merrill, pp. 791–814, Pergamon, New York, 1977.
Guppy, D. J., R. Brett, and D. J. Milton, Liverpool and Strangways craters, Northern Territory: Two probable structures of impact origin, *J. Geophys. Res., 76,* 5387–5393, 1971.
Harlow, F. H., and W. E. Pracht, Formation and penetration of high-speed collapse jets, *Phys. Fluids, 9,* 1951, 1966.
Hartung, J. B., M. R. Dence, and J. A. S. Adams, Potassium-argon dating of shock metamorphosed rocks from the Brent impact crater, Ontario, Canada, *J. Geophys. Res., 76,* 5437–5448, 1971.
Head, J. W., and R. Roth, Mars pedestal crater escarpments: Evidence for ejecta related emplacement, in *Symposium on Planetary Cratering Mechanisms,* pp. 50–52, Lunar Science Institute, Houston, Tex., 1976.
Higgins, G. H., and T. R. Butkovich, Effects of water content, yield, medium and depth of burst on crater radii, *Rep. UCRL-5023,* Lawrence Radiat. Lab., Livermore, Calif., 1967.
Hörz, F., R. B. Gibbons, R. E. Hill, and D. E. Gault, Large scale cratering into lunar highlands: Some Monte Carlo considerations, *Proc. Lunar Sci. Conf. 7th,* 2931–2945, 1976.
Hughes, H. G., F. N. App, and T. R. McGetchin, Global seismic effects of basin forming impacts, *Phys. Earth Planet. Interiors, 15,* 251–263, 1977.
Janssens, M. J., J. Hertogen, H. Takahashi, and E. Anders, Rochechouart meteorite crater: Identification of projectile, *J. Geophys. Res., 82,* 750–758, 1977.
Jessberger, E. K., J. C. Huneke, F. A. Podosek, and G. J. Wasserburg, High-resolution argon analyses of neutron-irradiated Apollo 16 rocks and separated minerals. *Proc. Lunar Sci. Conf. 5th,* 1419–1449, 1974.
Jones, E. M., and M. T. Sandford, Numerical simulation of a very large explosion at the earth's surface with possible application to tektites, in *Impact and Explosion Cratering,* edited by D. J. Roddy, R. O. Pepin, and R. B. Merrill, pp. 1009–1024, Pergamon, New York, 1977.
Kalashnikov, N. G., N. M. Pavlouskiy, G. W. Simakov, and R. F. Trunin, Dynamic compressibility of calcite group minerals, *Izv. Akad. Nauk SSSR Fiz. Zemli,* no. 2, 23–29, 1973.
Kaula, W. M., Planetary thermal evolution during accretion, in *Lunar Science IX,* pp. 615–617, Lunar and Planetary Institute, Houston, Tex., 1978.
Kieffer, S. W., Shock metamorphism of Coconino sandstone at Meteor Crater, Arizona, *J. Geophys. Res., 76,* 5449–5473, 1971.
Kieffer, S. W., From regolith to rock by shock, *Moon, 13,* 301–320, 1975*a*.
Kieffer, S. W., Droplet chondrules, *Science, 189,* 333–340, 1975*b*.
Kieffer, S. W., Impact conditions required for formation of melt by jetting in silicates, in *Impact and Explosion Cratering,* edited by D. J. Roddy, R. O. Pepin, and R. B. Merrill, pp. 751–769, Pergamon, New York, 1977.
Kieffer, S. W., and J. M. Delany, Isentropic decompression of fluids from crustal and mantle pressures, *J. Geophys. Res., 84,* 1611–1620, 1979.
Kieffer, S. W., D. P. Phakey, and J. M. Christie, Shock processes in porous quartzite: Transmission electron microscopic observations and theory, *Contrib. Mineral. Petrol., 59,* 41–93, 1976*a*.
Kieffer, S. W., R. B. Schaal, R. Gibbons, F. Hörz, D. J. Milton, and A. Duba, Shocked basalt from Lonar impact crater, India, and experimental analogues, *Proc. Lunar Sci. Conf. 7th,* 1391–1412, 1976*b*.
Kraut, F., and B. French, The Rochechouart meteorite impact structure, France: Preliminary geological results, *J. Geophys. Res., 76,* 5407–5413, 1971.
Lambert, P., Les effets des ondes de choc naturelles et artificielles, et le cratère d'impact de Rochechouart, Ph.D. thesis, 515 pp., Université de Paris, Paris, Oct. 1977.
Lambert, R. St. J., and V. E. Chamberlain, CO_2 permafrost and Martian topography, *Icarus, 34,* 568–580, 1978.
Lunar Sample Preliminary Examination Team, Preliminary examination of lunar samples from Apollo 11, *Science, 165,* 1211–1227, 1969.
Masaitis, V. L., Astroblemes in the USSR (in Russian), *Sov. Geol., 1975,* 52–64, 1975.
Masaitis, V. L., M. V. Mikhaylov, and T. V. Selivanouskaya, Popigai meteorite crater (in Russian), report, 124 pp., All Union Sci. Res. Geol. Inst., Moscow, 1975.
Maxwell, D. E., Simple Z model of cratering, ejection and the overturned flap, in *Impact and Explosion Cratering,* edited by D. J Roddy, R. O. Pepin, and R. B. Merrill, pp. 1003–1008, Pergamon, New York, 1977.
McCabe, H. R., and B. B. Bannatyne, Lake St. Martin crypto-explosion crater and geology of surrounding area, *Geol. Pap. 3/70,* 79 pp., Geol. Surv. of Manit., Winnipeg, 1970.
McQueen, R. G., S. P. Marsh, J. N. Fritz, Hugoniot equation of state of 12 rocks, *J. Geophys. Res., 72,* 4999–5036, 1967.
Melosh, H. J., On the origin of fractures radial to lunar basins, *Proc. Lunar Sci. Conf. 7th,* 2967–2982, 1976.
Melosh, H. J., Crater modification by gravity: A mechanical analysis of slumping, in *Impact and Explosion Cratering* edited by D. J. Roddy, R. O. Pepin, and R. B. Merrill, pp. 1245–1260, Pergamon, New York, 1977.
Milton, D. J., et al., Gosses Bluff impact structure, Australia, *Science, 175,* 1199–1207, 1972.
Moore, H. J., Missile impact craters (White Sands Missile Range, New Mexico) and applications to lunar research, *U.S. Geol. Surv. Prof. Pap., 812-B,* 47 pp., 1976.
Morgan, J. W., M.-J. Janssens, J. Hertogen, J. Gros, and H. Takahashi, Ries impact crater: Search for meteoritic material, *Geochim. Cosmochim. Acta, 43,* 803–816, 1979.
Oberbeck, V. R., Application of high explosion cratering data to planetary problems, in *Impact and Explosion Cratering,* edited by D. J. Roddy, R. O. Pepin, and R. B. Merrill, pp. 45–66, Pergamon, New York, 1977.
Oberbeck, V. R., and R. H. Morrison, Candidate areas for in situ ancient lunar materials, *Proc. Lunar Sci. Conf. 7th,* 2983–3005, 1976.
Offield, T. W., and H. A. Pohn, Deformation at the Decaturville impact structure, Missouri, in *Impact and Explosion Cratering,* edited by D. J. Roddy, R. O. Pepin, and R. B. Merrill, pp. 11–14, Pergamon, New York, 1977.
O'Keefe, J. D., and T. J. Ahrens, Shock effects from a large impact on the moon, *Proc. Lunar Sci. Conf. 6th,* 2831–2844, 1975.
O'Keefe, J. D., and T. J. Ahrens, Impact ejecta on the moon, *Proc. Lunar Sci. Conf. 7th,* 3007–3025, 1976.
Onorato, P. I. K., D. R. Uhlmann, and C. H. Simonds, Heat flow in impact melts: Apollo 17 Station 6 boulder and some applications to other breccias and xenolith-laden melts, *Proc. Lunar Sci. Conf. 7th,* 2449–2467, 1976.
Onorato, P. I. K., D. R. Uhlmann, and C. H. Simonds, Thermal history of Manicouagan impact melt sheet, Quebec, *J. Geophys. Res., 83,* 2789–2798, 1978.
Orphal, D. L., Calculations of explosion cratering, I, The shallow-buried nuclear detonation Johnie Boy, in *Impact and Explosion Cratering,* edited by D. J. Roddy, R. O. Pepin, and R. B. Merrill, pp. 897–906, Pergamon, New York, 1977.
Ostro, S. J., and G. H. Pettengill, Icy craters on the Galilean satellites, *Icarus, 34,* 268–279, 1978.
Palme, H., M.-J. Janssens, H. Takahashi, E. Anders, and J. Hertogen, Meteoritic material in five large impact craters, *Geochim. Cosmochim. Acta, 42,* 313–323, 1978.
Phinney, W. C., C. H. Simonds, A. Cochran, and P. E. McGee, West Clearwater, Quebec impact structure, II, Petrology, *Proc. Lunar Sci. Conf. 9th,* 2659–2693, 1978.
Pohl, J., D. Stöffler, H. Gall, and K. Ernstson, The Ries impact crater, in *Impact and Explosion Cratering,* edited by D. J. Roddy, R. O. Pepin, and R. B. Merrill, pp. 343–404, Pergamon, New York, 1977.
Rehfuss, D. E., D. Michael, J. C. Anselmo, and N. K. Kincheloe, A model for the wind-extension of the Copernicus eject blanket, in *Impact and Explosion Cratering,* edited by D. J. Roddy, R. O. Pepin, and R. B. Merrill, pp. 1123–1132, Pergamon, New York, 1977.
Reiff, W., The Steinheim Basin—An impact structure, in *Impact and Explosion Cratering,* edited by D. J. Roddy, R. O. Pepin, and R. B. Merrill, pp. 309–320, Pergamon, New York, 1977.
Rice, M. H., and J. M. Walsh, Equation of state of water to 250 kb, *J. Chem. Phys., 26,* 824–830, 1957.
Riney, T. D., S. K. Garg, J. W. Kirsch, L. W. Morland, and C. R. Hastings, Stress wave effects in inhomogeneous and porous earth materials, *Rep. 35R-267,* Systems, Science and Softwave, La Jolla, Calif., 1970.
Robertson, P. B., Zones of shock metamorphism at the Charlevoix impact structure, Quebec, *Geol. Soc. Amer. Bull., 86,* 1630–1638, 1975.
Robertson, P. B., and R. A. F. Grieve, Shock attenuation at terrestrial impact structures, in *Impact and Explosion Cratering,* edited by D. J. Roddy, R. O. Pepin, and R. B. Merrill, pp. 687–702, Pergamon, New York, 1977.

Roddy, D. J., The Flynn Creek Crater, Tennessee, in *Shock Metamorphism of Natural Materials,* edited by B. M. French and N. M. Short, pp. 291–322, Mono, Baltimore, Md., 1968.

Roddy, D. J., R. O. Pepin, and R. B. Merrill (Eds.), *Impact and Explosion Cratering,* 1301 pp., Pergamon, New York, 1977.

Rondot, J., Impactite at the Charlevoix structure, Quebec, Canada, *J. Geophys. Res., 76,* 5414–5423, 1971.

Ruoff, A. L., Linear shock-velocity-particle-velocity relationship, *J. Appl. Phys., 38,* 4976–4980, 1967.

Schaal, R. B., and F. Hörz, Shock metamorphism of lunar and terrestrial basalts, *Proc. Lunar Sci. Conf. 8th,* 1697–1729, 1977.

Schock, R. N., The response of rocks to large stresses, in *Impact and Explosion Cratering,* edited by D. J. Roddy, R. O. Pepin, and R. B. Merrill, pp. 657–668, Pergamon, New York, 1977.

Shipman, F. H., and V. G. Gregson, A shock wave study of Coconino sandstone, final Report, p. 1, Mater. and Struct. Lab., Gen. Mot. Corp., Warren, Mich., 1970.

Shoemaker, E. M., Impact mechanics at Meteor Crater Arizona, in *The Moon, Meteorites and Comets—The Solar System,* vol. 4, edited by B. Middlehurst and G. P. Kuiper, pp. 301–336, University of Chicago Press, Chicago, Ill., 1963.

Shoemaker, E. M., Astronomically observable crater-forming projectiles, in *Impact and Explosion Cratering,* edited by D. J. Roddy, R. O. Pepin, and R. B. Merrill, pp. 617–628, Pergamon, New York, 1977.

Shoemaker, E. M., and S. W. Kieffer, *Guidebook to the Geology of Meteor Crater Arizona,* p. 66, Institute of Meteoritics, Arizona State University, Tempe, 1974.

Short, N. M., The anatomy of an impact crater: West Hawk Lake, Manitoba, Canada, *Geol. Soc. Amer. Bull, 81,* 609–648, 1970.

Short, N. M., and M. L. Foreman, Thickness of impact crater ejecta on the lunar surface, *Mod. Geol., 3,* 69–91, 1972.

Simonds, C. H., Thermal regimes in impact melts and the petrology of the Apollo 17 Station 6 boulder, *Proc. Lunar Sci. Conf. 6th,* 641–672, 1975.

Simonds, C. H., and P. E. McGee, Petrology of impactites at Lake St. Martin, Manitoba structure, *Proc. Lunar Planet. Sci. Conf. 10th,* 2493–2518, 1979.

Simonds, C. H., W. C. Phinney, J. L. Warner, P. E. McGee, J. Geeslin, R. W. Brown, and J. M. Rhodes, Apollo 14 revisited, or breccias aren't so bad after all, *Proc. Lunar Sci. Conf. 8th,* 1869–1893, 1977.

Simonds, C. H., R. J. Floran, P. E. McGee, W. C. Phinney, and J. L. Warner, Petrogeneis of melt rocks, Manicouagan impact structure, Quebec, *J. Geophys. Res., 83,* 2773–2788, 1978*a*.

Simonds, C. H., W. C. Phinney, P. E. McGee, and A. Cochran, West Clearwater impact structure, 1, Field geology, structure and bulk chemistry, *Proc. Lunar Planet. Sci. Conf. 9th,* 2633–2658, 1978*b*.

Soderblom, L. A., and D. B. Wenner, Possible fossil H_2O liquid-ice interfaces in the Martian crust, *Icarus, 34,* 622–637, 1978.

Stähle, V., Impact glasses from suevite of the Nordlinger Ries, *Earth Planet. Sci. Lett., 17,* 275–293, 1972.

Stähle, V., and J. Ottemann, Ries-Forschungsbohrung 1973: Zeolithigierung der Gläser in Suevit und petrographic der Beckensuevite und gangbreccian, *Geol. Bavarica, 75,* 191–217, 1977.

Stanfors, R., Lake Mien—An astrobleme or a volcanic-tectonic structure, *Geol. Foeren. Stockholm Foerh., 91,* 73–86, 1969.

Stearns, R. G., C. W. Wilson, H. A. Tiedemann, J. T. Wilcox, and P. S. Marsh, The Wells Creek structure Tennessee, in *Shock Metamorphism of Natural Materials,* edited by B. M. French and N. M. Short, pp. 323–338, Mono, Baltimore, Md., 1968.

Stöffler, D., Deformation and transformation of rock forming minerals by natural and experimental shock processes, I, Behavior of minerals under shock compression, *Fortschr. Mineral., 49,* 50–113, 1972.

Stöffler, D., Research drilling Nordlingen, 1973: Polymict breccias, crater basement and cratering model of the Ries impact structure, *Geol. Bavarica, 75,* 443–458, 1977.

Stöffler, D., D. E. Gault, J. Wedekind, and G. Polkowski, Experimental hypervelocity impact into quartz sand: Distribution and shock metamorphism of ejecta, *J. Geophys. Res., 80,* 4062, 1975.

Stöffler, D., U. Ewald, R. Ostertag, and W. U. Reimold, Research drilling Nordlingen 1973 (Ries) composition and texture of polymict impact breccias, *Geol. Bavarica, 75,* 163–190, 1977.

Sweeney, J. F., Gravity study of great impact, *J. Geophys. Res., 83,* 2809–2816, 1978.

Taylor, S. R., and S. R. McLennan, Chemical similarity between irghizites and Javan tektites, *Lunar and Planetary Science X,* pp. 1219–1221, Lunar and Planetary Institute, Houston, Tex., 1979.

Toulmin, P., A. K. Baird, B. C. Clark, K. Keil, H. J. Rose, R. P. Christian, P. H. Evans, and W. C. Kelliher, Geochemical and mineralogical interpretation of the Viking inorganic chemical results, *J. Geophys. Res., 82,* 4625–4634, 1977.

Trulio, J. G., Ejecta formations: Calculated from motion from a shallow-buried nuclear burst, and its significance for high velocity impact cratering, in *Impact and Explosion Cratering,* edited by D. J. Roddy, R. O. Pepin, and R. B. Merrill, pp. 919–957, Pergamon, New York, 1977.

van Terzaghi, K., *Theoretical Soil Mechanics,* John Wiley, New York, 1945.

von Engelhardt, W., Shock produced glasses from the Ries Crater, *Contrib. Mineral. Petrol., 36,* 265–292, 1972.

von Engelhardt, W., and G. Graup, Stosswellen metamorphose in Kristallin der Forschungs-bohrung Nördlingen 1973, *Geol. Bavarica, 75,* 255–271, 1977.

von Engelhardt, W., D. Stöffler, and W. Schneider, Petrologische Untersuchungen in Ries, *Geol. Bavarica, 61,* 229–295, 1969.

Walsh, J. M., and R. H. Christian, Equation of state of metals from shock wave measurements, *Phys. Rev., 97,* 1544, 1955.

Walsh, J. M., R. G. Shreffler, and F. J. Willig, Limiting conditions for jet formation in high velocity collisions, *J. Appl. Phys., 24,* 349, 1953.

Warner, J. L., C. H. Simonds, and W. C. Phinney, Apollo 16 rocks classification and petrogenetic model, *Proc Lunar Sci. Conf. 4th,* 481–504, 1973.

Wilshire, H. G., T. W. Offield, K. A. Howard, and D. Cummings, Geology of the Sierra Madera cryptoexplosion structure, Pecos County, Texas, *U.S. Geol. Surv. Prof. Pap., 599-H,* 42, 1972.

Winzer, S. R., The Steen River astrobleme, Alberta, Canada, *Proc. Int. Geol. Cong. 24th, Sect. 15,* 148–156, 1972.

Yurk, Yu. Yu., G. K. Yeremenko, and Yu. A. Polkanov, The Boltysh depression: A fossil meteorite crater, *Int. Geol. Rev., 18,* 196–202, 1975.

Zook, H. A., The state of meteoritic material on the moon, *Proc. Lunar Sci. Conf. 6th,* 1653–1672, 1975.

(Received July 26, 1979;
accepted August 6, 1979.)